RMUTL Engineering Journal

Volume10 Issue 2 July - December

ISSN(Print) 3027-7426
ISSN(Online) 3027-7434

Journal of Engineering

Rajamangala University of technology Lanna

Journal of Engineering
Rajamangala University of technology Lanna
It has been assessed to be in the database of the Thai Journal Citation Index Center (TCI), Tier 1.

Faculty of Engineering

Journal of Engineering
Rajamangala University of Technology Lanna

Objective

The Rajamangala University of Technology Lanna Engineering Journal is an academic journal first published in January 2016. The journal aims to disseminate research findings and scholarly knowledge in research and academic services, thereby contributing to academic progress and professional standards. The scope of the journal includes the following areas of research: Mechatronics Engineering, Control Systems Engineering, Electrical Engineering, Electronic Engineering, Telecommunications Engineering, Mechanical Engineering Agricultural Engineering, Computer Engineering, Material Handling Engineering, Industrial Engineering, Mold Engineering, Metallurgical Engineering, Civil Engineering, Environmental Engineering, Mining Engineering, Related Sciences and Technologies.

Owner
Faculty of Engineering, Rajamangala University of Technology Lanna
Address: 128 Huay Kaew Road, Chang Phueak Subdistrict, Mueang District, Chiang Mai Province 50300
Phone: 0 5392 1444 ext. 1205
Website: https://engineering.rmutl.ac.th/journal and https://www.tci-thaijo.org/index.php/RMUTLEngJ
Email: EngineeringJournal@rmutl.ac.th

Letter From the Editor

Rajamangala University of Technology Lanna Engineering Journal (RMUTL Eng. J.) Year 10, Issue 2, July - December 2025 t is in the Thai Journal Citation Index (TCI) database, Tier 1. Research articles submitted through the system have been evaluated for quality by the editorial board and experts (Peer Review) from various fields. The editorial team will maintain the quality of the journal to meet standards in order for the Engineering Journal (RMUTL Eng. J.) to be accepted and to continuously share quality and up-to-date academic knowledge.

This issue of Rajamangala University of Technology Lanna Engineering Journal (RMUTL Eng. J.) has compiled 6 peer-reviewed academic articles, including articles on civil engineering, industrial engineering, computer engineering and electrical engineering. For those interested, you can read the current or previous editions of this article online at https://www.tci-thaijo.org/index.php/RMUTLEngJ.

On behalf of the Editorial Board of the Rajamangala University of Technology Lanna Engineering Journal (RMUTL Eng. J.), we extend our sincere appreciation to all researchers who have submitted articles for consideration. We also would like to thank everyone who took the time to evaluate the articles and provide suggestions for improving the quality of the content. We gratefully acknowledge the support of The Executive Committee of Rajamangala University of Technology Lanna Sponsors, as well as the dedication of the journal's editorial team (RMUTL Eng. J.), whose collective efforts continue to further improve the quality of the journal. And on this occasion, I would like to invite professors, researchers and students to submit research articles, academic articles or review articles related to engineering in English for publication in future issues of the journal (RMUTL Eng. J.).

(Asst. Prof. Dr. Krisda Yingkayun)
Editor of the Engineering Journal, Rajamangala University of Technology Lanna

List of Contents

Year 10, Issue 2, July - December 2025

Academic articles

Comparison of Elevation in a straight line from Leveling with Level and Global Navigation Satellite Systems

Phanu Uthaisri*, Plaifah Oopkao, Natipat Sukpasong and Mathawee Chaichompu
Program of Civil Engineering Division of Civil Engineering and Environment, Faculty of Engineering, Rajamangala University of Technology Lanna
128 Huay Kaew Road, Muang, Chiang Mai, Thailand, 50300
*Corresponding Author: Phanu@rmutl.ac.th. Phone Number: +66-856166191

Received: 2 May 2025, Revised: 19 July 2025, Accepted: 27 July 2025

Abstract
Accurate elevation determination is essential in civil engineering for ensuring the structural integrity of constructed facilities. Traditional optical leveling, while highly precise, requires transferring elevation values from existing benchmarks, which can be time-consuming when the benchmarks are located far from the project area. Recent advances in Global Navigation Satellite Systems (GNSS) technology-especially using static surveying techniques with post-processing and geoid correction-have enabled the possibility of determining elevation data more efficiently. This study evaluates the accuracy of GNSS-based elevation measurements compared with conventional third-order leveling methods, focusing on a straight-line transect of 2,201 meters at the Agricultural Technology Research Institute, Rajamangala University of Technology Lanna. The GNSS survey was conducted using the static method, with observed data post-processed and converted from ellipsoidal to orthometric height using the Thailand Geoid Model 2017 (TGM2017). The optical leveling was performed to third-order standards using both aluminum and Invar leveling rods. Results show that the elevation difference obtained from GNSS measurements deviated by only 6 millimeters from the optical leveling result, which falls within the allowable error margin for third-order leveling standards. The findings confirm that GNSS, when used with a validated geoid model, is a viable alternative for elevation determination in engineering applications under the Thai vertical datum, particularly for establishing local control benchmarks with reduced fieldwork time and cost.
Keywords: GNSS, GNSS Leveling, Third-order Leveling, Elevation Survey.

1. Introduction

Leveling is a fundamental technique in civil engineering and surveying that ensures structures are positioned accurately in the vertical dimension. It involves measuring the elevation, or height above a reference surface, at specific points, or determining the elevation difference between two locations [1]. Elevation information is crucial because errors in vertical positioning can lead to serious structural and drainage problems. For example, if a building's foundation is not properly leveled, it may experience uneven settlement, leading to cracks or even structural failure. In typical engineering projects, leveling is used during the design and construction phases to ensure that roads, bridges, buildings, and pipelines conform precisely to their design specifications. Normally, surveyors reference known elevation points, called benchmarks, to anchor their measurements. Traditional leveling methods often rely on optical instruments, such as automatic levels and leveling rods, which require setting up equipment along a line of sight between points. This method, although highly accurate, can be labor-intensive and time-consuming, especially when benchmarks are located far from the project site, requiring many intermediate measurements.

The Global Navigation Satellite System (GNSS) provides positioning data on the Earth's surface, enabling the determination of both horizontal and vertical coordinates. Initially, vertical positioning obtained through GNSS exhibited significant errors, making it unsuitable for engineering applications. However, over the past several years, advancements in geoid modeling—especially the development of

country-specific geoid models such as Thailand Geoid Model 2017 (TGM2017)-have substantially improved the accuracy of vertical coordinates, allowing for the conversion of ellipsoidal heights into orthometric heights with centimeter-level precision [2].

Consequently, GNSS technology is increasingly employed to obtain both horizontal and vertical positions [3], with vertical accuracies meeting the requirements of third-order leveling standards for engineering works [4]. Recent studies in Thailand have verified the reliability of combining GNSS static surveys with TGM2017 in real-world environments, especially in reducing time, labor, and cost associated with conventional optical leveling [5-6]. Recognizing these technological advancements, the researcher aims to evaluate whether GNSS-based leveling can achieve third-order accuracy suitable for engineering applications. If successful, this method could be used to establish local control benchmarks more efficiently, resulting in significant savings in both time and cost associated with traditional leveling methods.

2. Literature and Methodology

In the context of surveying, precise elevation data is typically obtained through leveling techniques defined by engineering standards [7]. Third-order leveling is widely accepted for engineering applications due to its balance of accuracy and field efficiency. Over the years, GNSS technologies have emerged as viable alternatives to traditional methods, offering potential benefits in reducing manpower, time, and accessibility constraints [8].

GNSS-based height determination relies on satellite observations to calculate ellipsoidal height, which must be converted to orthometric height for engineering applications. This conversion is performed using a geoid model that represents the shape of the Earth's gravity field. The precision of this conversion depends heavily on the accuracy and regional suitability ozf the geoid model in use [9]. Limitations of global geoid models such as EGM96 or EGM2008-particularly their coarse resolution-can introduce discrepancies when applied to local conditions [10]. Therefore, several countries, including Thailand, have developed high-resolution local geoid models.

The Thailand Geoid Model 2017 (TGM2017) was developed using a combination of airborne and terrestrial gravimetric data, GNSS/leveling benchmarks, and advanced interpolation techniques [2], [11]. The model provides centimeter-level accuracy for converting ellipsoidal heights derived from GNSS to orthometric heights under the Thai vertical datum. It has become a standard reference model in Thai geodetic and engineering practice.

Studies in other regions, such as Nigeria, have similarly validated the use of GNSS-derived ellipsoidal heights combined with regional or global geoid models for determining orthometric elevations [12]. These findings reinforce the global applicability of satellite-based leveling methodologies when paired with a suitable geoid framework.

This study compares the elevation difference between two benchmarks measured using two methods: third-order optical leveling and GNSS static survey with post-processing. The study site is located at the Agricultural Technology Research Institute, Rajamangala University of Technology Lanna, Lampang Campus, as shown in Figure 1, which is situated in northern Thailand and serves as an ideal location for field-based geodetic studies due to its open terrain and controlled conditions.

Aerial imagery of the campus, as shown in Figure 2, displays the alignment of the measurement path along agricultural service roads and adjacent flat ground. Two benchmarks, BM4 and BM11, were selected along a straight transect of 2,201 meters, which were placed and referenced by the university's surveying team (as shown in Figure 3).

The overall research design followed a stepwise protocol consisting of field reconnaissance, benchmark setup, GNSS observation using the static method, optical leveling using aluminum and Invar rods, data processing, and final comparison. A summarized flow of the methodology is illustrated in Figure 4.

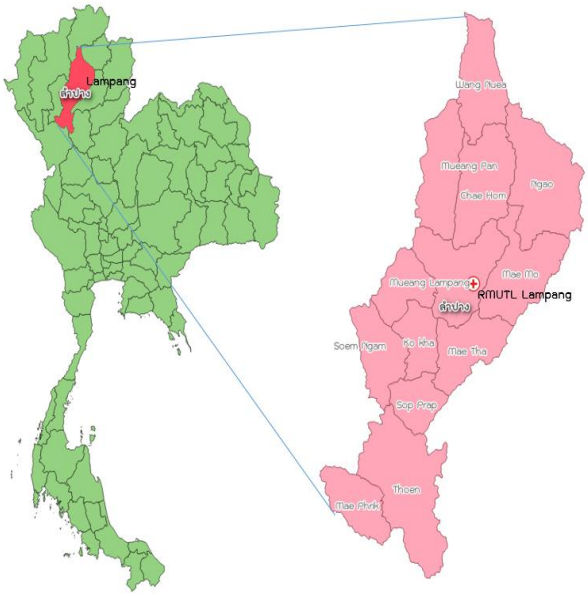

Figure 1 Location of Rajamangala University of Technology Lanna, Lampang Campus, Lampang Province.

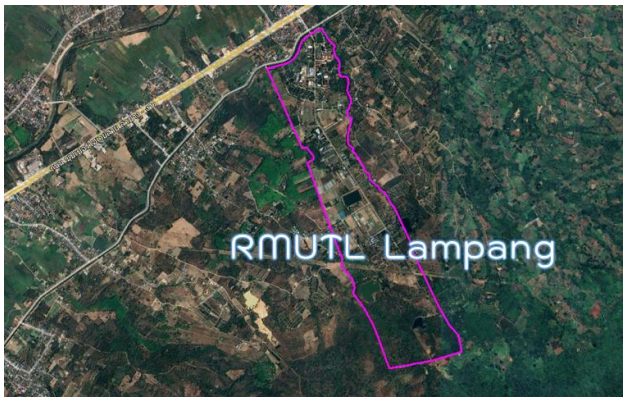

Figure 2 Aerial view of the Agricultural Technology Research Institute, Rajamangala University of Technology Lanna, Lampang Campus.

Figure 3 Locations of the benchmark points used for elevation testing.

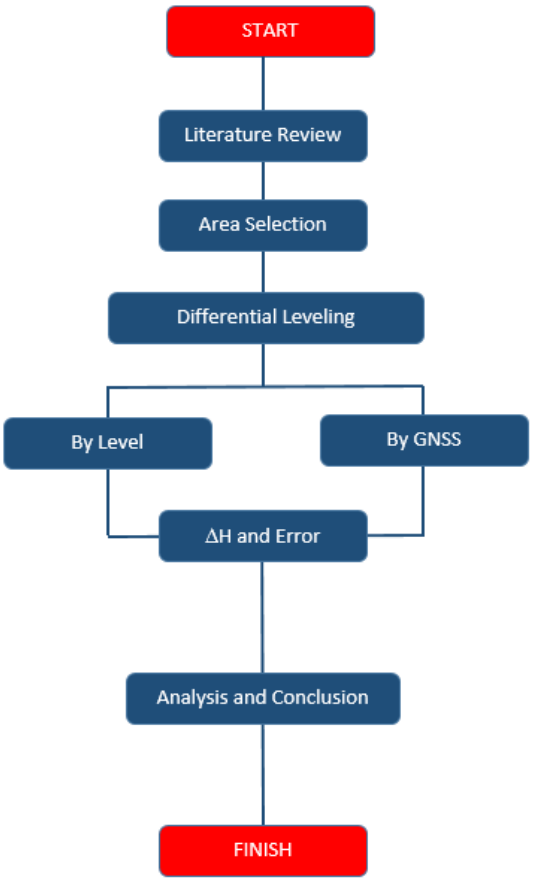

Figure 4 Flowchart of the research methodology.

2.1 Instruments and Equipment

The instruments and equipment used in this research are listed below and illustrated in Figures 5-7.

1) Sokkia C31 automatic level and tripod (Figure 5)
2) Folding aluminum leveling rod (Figure 5)
3) Invar leveling rod (Figure 6)
4) Foot plate (Figure 6)
5) Measuring tape (Figure 6)
6) GNSS Trimble R8s dual-frequency receiver (Figure 7)

Figure 5 Leveling instrument: Sokkia C31 with tripod.

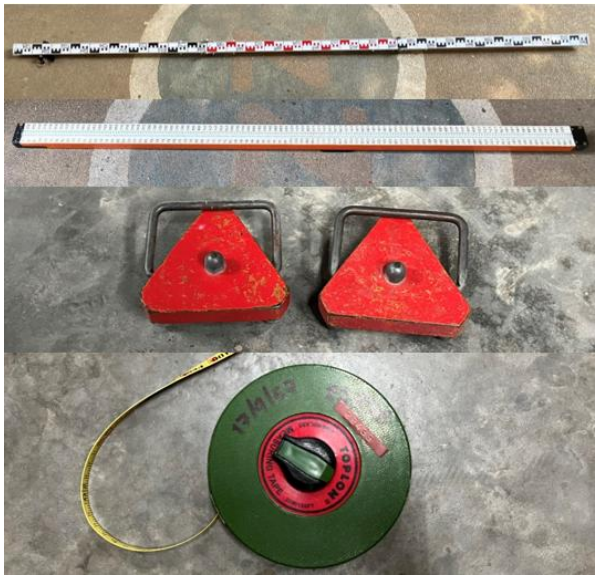

Figure 6 Aluminum folding Staff, Invar Staff, foot plate and measuring tape.

Figure 7 GNSS receiver Trimble R8s and supporting accessories

2.2 Fieldwork Procedures

After selecting the study area, a detailed evaluation of the terrain was conducted to determine the longest possible straight-line segment available within the site. This selection process is crucial because a straight-line layout minimizes errors associated with changes in direction and simplifies the comparison of elevation data collected by different methods. The chosen transect not only needed to maximize distance but also maintain direct line-of-sight and stable ground conditions suitable for accurate surveying. By ensuring the area of interest was as linear and uniform as possible, both GNSS and traditional optical leveling techniques could be applied under controlled and comparable conditions, strengthening the validity of the resulting analysis.

Figure 8 RTSD control point A100358

The GNSS survey was conducted using the static method, which involves placing dual-frequency GNSS receivers at both known and unknown stations. Initially, a receiver was installed and configured at the military geodetic control point A100358 (as shown in Figure 8), and additional GNSS units were deployed at the two benchmark locations, BM4 and BM11. Observations were conducted simultaneously and continuously for 1 hour and 30 minutes at each station. This extended observation duration helped improve positional accuracy by mitigating atmospheric disturbances and satellite geometry fluctuations. The base station was initialized at BM4 using known reference coordinates, while the rover receiver was positioned at BM11. During the observation period, field personnel monitored satellite geometry and signal obstructions to ensure data quality. Upon completion, RINEX data from the receivers were transferred to Trimble Business Center software for post-processing, which provided precise ellipsoidal coordinates. The orthometric heights (elevations above the geoid) were subsequently calculated using the TGM2017 geoid model, allowing an accurate determination of the elevation difference between BM4 and BM11.

The second method involved conducting a traditional elevation survey using a Sokkia C31 automatic level and two types of leveling rods: a 3-meter aluminum rod and a 3-meter Invar rod. The elevation of BM4, obtained from the GNSS survey, was adopted as the starting reference elevation. The leveling operation proceeded along the same straight-line transect, with intermediate checkpoints established every 500 meters to monitor cumulative error. In each segment, the leveling path was divided into distances not exceeding 40 meters and measured in alternating forward and backward directions using a leapfrog pattern. This approach allowed for systematic error detection and comparison between rod materials, including evaluating the influence of thermal expansion. Observations were conducted to comply with third-order leveling standards, applying a maximum allowable misclosure of $\pm 12\sqrt{K}$ mm, where K is the total distance in kilometers. All elevation differences were recorded in field notebooks and later compiled into a leveling loop adjustment table to compute the net elevation change between BM4 and BM11. By employing both GNSS-based static surveying and precise third-order optical leveling, this study ensured a robust comparative methodology. The use of intermediate checkpoints and dual rod types added redundancy and enhanced the reliability of the optical leveling results, while the extended GNSS observation time and rigorous data processing minimized positioning error. Together, the two approaches enabled a comprehensive evaluation of whether GNSS with geoid correction could reliably substitute traditional leveling techniques for engineering applications, especially in establishing third-order leveling benchmarks

3. Results and Discussion

3.1 GNSS Elevation Results

GNSS observations at BM4 and BM11 were post-processed using Trimble Business Center software. The data from the static survey was converted from ellipsoidal height to orthometric height using the TGM2017 geoid model. The orthometric height values are shown in Table 1.

Table 1 Orthometric heights from GNSS measurements using TGM2017

Benchmark	Ellipsoidal Height (m)	Geoid Undulation (m)	Orthometric Height (m)
BM4	222.562	-37.269	**259.831**
BM11	256.356	-37.228	**293.593**

The elevation difference between BM4 and BM11, as obtained from the GNSS survey, was calculated to be 33.762 meters. The location of the GNSS setup at points BM4 and BM11, as shown in Figure 9 and Figure 10.

Figure 9 GNSS receiver setup at point BM4

Figure 10 GNSS receiver setup at point BM11

Figure 11 Survey line from point BM4 to point BM11

Figure 12 Leveling procedure using an automatic level

3.2 Optical Leveling Results

The optical leveling survey was conducted along the same transect using a Sokkia C31 automatic level, with aluminum and Invar leveling rods used during the forward and return runs, respectively. Intermediate checkpoints were established every 500 meters, and segment lengths were kept under 40 meters to maintain third-order accuracy. The leveling path is depicted in Figure 11. Leveling was performed over the entire 2,201-meter transect to determine the elevation difference, as shown in Figure 12.

A sample of leveling survey data is shown in Table 2, illustrating the detailed field observations recorded during the optical leveling process. This includes back sight (BS), fore sight (FS), intermediate readings, distances, and computed elevations at each checkpoint, which were used to verify measurement consistency and ensure compliance with third-order leveling standards.

Table 2 Example of leveling data collected during the survey

Target	BS	INT	Dist	FS	INT	Dist	HI	Elve
BM4	1.566						261.273	259.831
	1.442	0.124						
	1.318	0.124						
		24.8	24.8					
TP1	1.385			1.599			261.059	259.799
	1.2605	0.1245		1.4745	0.1245			
	1.136	0.1245		1.35	0.1245			
		24.9	49.7		24.9	24.9		
TP2	1.46			1.402			261.116	259.782
	1.334	0.126		1.277	0.125			
	1.208	0.126		1.152	0.125			
		25.2	74.9		25	49.9		
TP3	1.332			1.39			261.054	259.852
	1.202	0.13		1.2645	0.1255			
	1.072	0.13		1.139	0.1255			
		26	100.9		25.1	75		
TP4	2.125			1.446			261.733	259.733
	2	0.125		1.321	0.125			
	1.875	0.125		1.196	0.125			
		25	125.9		25	100		
TP5	1.411			1.431			261.714	260.379
	1.335	0.076		1.3535	0.0775			
	1.259	0.076		1.276	0.0775			
		15.2			15.5			
TP6	1.385			0.95			262.13	260.87
	1.2605	0.1245		0.8445	0.1055			
	1.136	0.1245		0.739	0.1055			
		24.9			21.1			
TP7	1.47			0.448			263.153	261.808
	1.3455	0.1245		0.3225	0.1255			
	1.221	0.1245		0.197	0.1255			
		24.9	150.8		25.1	125.1		

Table 3 shows the computed elevation values from the leveling data, highlighting the differences observed between aluminum folding and Invar rods. These values support the evaluation of rod performance under third-order leveling standards.

Table 3 Elevation results from third-order optical leveling survey

Staff	BM4 (m)	BM11 (m)	BM4 (m)	Error (m)
Folding	259.831	293.597	259.828	-0.003
Inva	259.831	293.598	259.834	+0.003

The total elevation difference from BM4 to BM11 obtained from optical leveling was 33.766 meters. The misclosure between forward and return runs was within 3 mm, which complies with the allowable error for third-order leveling ($\pm 12\sqrt{K}$ mm, where K = 2.201 km $\approx \pm 17.7$ mm).

3.3 Comparative Analysis

Before conducting the main comparison between GNSS-based elevation measurements and traditional optical leveling, this study initially evaluated the performance of two types of leveling rods: aluminum folding rods and Invar rods. The objective was to determine whether the more portable aluminum rod could satisfy the accuracy requirements of third-order leveling standards. As shown in Table 4, the elevation difference obtained using the aluminum rod was 33.768 meters, while the Invar rod yielded 33.765 meters. The discrepancy between the two was only 1 millimeter, well within the allowable error margin for third-order leveling ($\pm 12\sqrt{K}$ mm). These results confirm that aluminum folding rods, despite being more susceptible to thermal expansion, can be reliably used in third-order leveling applications when proper procedures are followed. This validation supports their practical use in field conditions, offering greater convenience without compromising accuracy. Following this confirmation, the study proceeded to compare GNSS-derived elevations with those obtained from optical leveling.

The difference between the GNSS-derived elevation difference and that from optical leveling was 0.006 meters (6 mm), well within the acceptable range for third-order leveling precision. This indicates that GNSS static surveying when paired with post-processing and geoid correction is capable of producing reliable vertical measurements.

Table 4 compares the elevation differences obtained from each method and also includes measurements using different rod types.

Staff	BM4 (m)	BM11 (m)	BM4 (m)	ΔH (m)
Folding	259.831	293.599	259.831	33.768
Inva	259.831	293.596	259.831	33.765

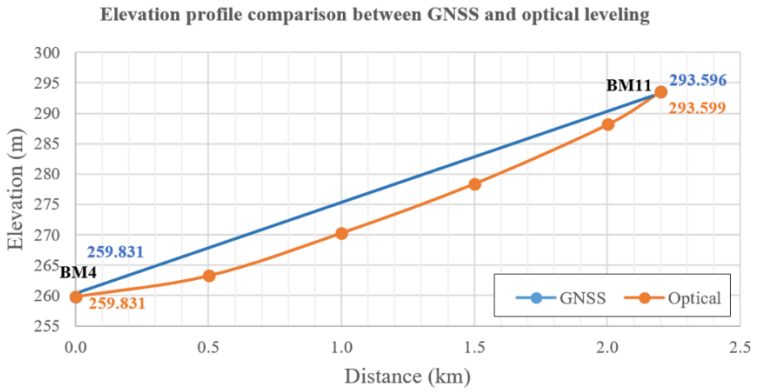

Figure 13 Elevation profile comparison between GNSS and optical leveling

3.4 Elevation Profile and Interpretation

Figure 13 illustrates the elevation profile along the transect, based on both GNSS and leveling observations. The plotted profiles show excellent alignment, with only minor deviations at checkpoint locations. These variations may be attributed to local surface irregularities or minor observational noise, but do not significantly affect the overall accuracy.

These results confirm the practicality of GNSS-based leveling for engineering applications under the Thai vertical datum. With proper observation time, equipment calibration, and reliable geoid models such as TGM2017, GNSS offers a time- and labor-efficient alternative to traditional leveling methods, especially for establishing third-order benchmarks in field environments.

4. Conclusions

This study presented a comparative evaluation of two elevation determination techniques-GNSS static surveying with geoid correction and conventional third-order optical leveling-conducted over a 2.201 km straight-line transect located within a controlled research area. The GNSS method, using post-processed data and the TGM2017 geoid model, produced an elevation difference of 33.762 meters between benchmarks BM4 and BM11. The corresponding elevation difference obtained via optical leveling was 33.762 meters. The observed discrepancy of 6 millimeters between the two methods falls well within the permissible tolerance for third-order leveling ($\pm 12\sqrt{K}$ mm), thereby confirming the reliability and consistency of both approaches.

The results validate that GNSS-based surveying, when combined with an appropriate local geoid model and sufficient observation duration, can serve as an efficient and accurate alternative to optical leveling, particularly for establishing elevation benchmarks under the Thai vertical datum. The advantages in operational time, reduced manpower, and flexibility in field conditions underscore its potential for broader engineering applications.

5. Acknowledgment

The authors would like to express their gratitude to the Agricultural Technology Research Institute, Rajamangala University of Technology Lanna, for providing access to the research site and supporting this study.

6. References

[1] Chugiat W, Sanya S. Plane Surveying: Leveling. Bangkok: Department of Survey | Engineering, Chulalongkorn University Press; 1996.

[2] Dumrongchai P, Srimanee C, Duangdee N, Bairaksa J. The determination of Thailand Geoid Model 2017 (TGM2017) from airborne and terrestrial gravimetry. Terrestrial Atmospheric and Oceanic Sciences. 2021;32(6):671–682.

[3] Geo - Informatics and Space Technology Development Agency. Global Navigation Satellite System (GNSS) Data - RINEX. Available from: https://sapace.gistda.or.th/en/services/ national -space - data - center-nsdc/global-navigation-satellite-system-gnss-data-rinex/(accessed Apr 27,2025)

[4] Pırtı A, Hoşbaş RG. Evaluation of some levelling techniques in surveying application. Geod Cartogr. 2019;68(2):361-373. doi: 10.24425/ gac.2019.128463

[5] Trimble Inc. Trimble Business Center User Guide (v5.50). Westminster, CO: Trimble Geospatial; 2022.

[6] Wichai Y. Engineering Survey 1. Bangkok. Chulalongkorn University Press; 2014.

[7] Federal Geodetic Control Subcommittee. FGCS specifications and procedures to incorporate electronic digital/bar-code leveling systems. NOAA National Geodetic Survey. Version 4.1; 2001.

[8] Kumar P, Srivastava PK, Tiwari P, Mall RK. Application of GPS and GNSS technology in geosciences. In: Petropoulos GP, Srivastava PK, editors. GPS and GNSS Technology in Geosciences. Elsevier; 2021. p. 415-427. doi:10.1016/B978-0-12-818617-6.00018-4

[9] Senthil Kumar S, Chauhan AK. Fast vertical positioning with GPS & EGM96 geoid model. *Proc 6th SPG Conf*. 2006;Paper 321.

[10] Abdel Aziz KM, Rashwan KS, Saba N. Evaluation of EGM96 and EGM08 based on GPS/levelling heights in Egypt. *South Afr J. Geomatics*. 2023;12(1):27- 40.

[11] Dumrongchai P, Duangdee N. Evaluation of TGM2017 for height system using GNSS/leveling data in Thailand. Int Trans J. Eng Manag Appl Sci Technol. 2019;10(10):1-10. doi:10.14456/ITJEMAST. 2019.135

[12] Herbert T, Olatunji RI. Determination of Orthometric Height Using GNSS and EGM Data: A Scenario of the Federal University of Technology Akure. Int J. Environ Geoinformatics. 2021;8(1):100-5. doi:10. 30897/ijegeo.754808

Production Improvement through Fixture Design: A Case Study of an Agricultural Machinery Parts Manufacturer

Bhoomboon Phontang[1], Jetnipat Pimollukanakul[1], Thamrong Gearam[1],
Jittiwat Nithikarnjanatharn[1] Supattra Muparang[2] and Wannisa Nutkhum[1*]
[1]Department of Industrial Engineering, Faculty of Engineering and Technology, Rajamangala University of Technology Isan
744 Sura Narai Road, Muang, Nakhon Ratchasima, Thailand, 30000
[2]Department of Industrial Engineering and Logistics, School of Engineering and Innovation, Rajamangala University of Technology Tawan-ok
43 Vibhavadi Rangsit Road, Sriracha, Chonburi, Thailand, 20110
[*]Corresponding Author: wannisa.nu@rmuti.ac.th* Phone Number: +66-928534148
Received: 27 December 2024, Revised: 4 June 2025, Accepted: 11 June 2025

Abstract
This case study focuses on a manufacturing company producing agricultural machinery parts. The company faced a significant challenge: it could not meet customer demand due to inefficiencies in the production process. The primary objective of this study was to enhance the production process by implementing a new Jig Fixture and leveraging the principles of karakuri kaizen. Through a thorough analysis of the production process, the Customer revealed that the daily demand was 350 units, while the company could only produce 280 units per day. The researchers employed engineering principles to address this issue, including 7 QC Tools and Failure Mode and Effects Analysis (FMEA). By identifying the root causes of the production bottlenecks, the team developed and implemented solutions involving a new workpiece holding device and Karakuri Kaizen automation. The results of these improvements were substantial. The cycle time per unit decreased from 96.22 seconds to 75.52 seconds, enabling the company to produce 362 daily units. The total production distance was reduced from 30.2 meters to 27.7 meters.
Keywords: Karakuri Kaizen, Jig Fixture, Failure Mode and Effects Analysis, 7 QC Tools

1. Introduction

The automotive parts industry is vital in driving a country's economy. Thailand's automotive industry is the largest in Southeast Asia and the 10th largest globally, with an annual production exceeding 1.5 million units, encompassing passenger cars, pickup trucks, motorcycles, and engine-powered vehicles. The country exports automotive parts worth more than $5 billion, surpassing the combined value of all Southeast Asian members in the same year. Additionally, 80% of automotive parts are produced domestically [1]

Thailand has over 2,000 parts manufacturing plants dispersed across industrial zones [2]. Procurement is categorized into 1) engine parts and components, 2) transmission parts, 3) suspension and brake parts, 4) electrical system parts, 5) body parts, and 6) other parts and accessories. Collaborative agreements among automotive parts manufacturers in all sectors have been developed to establish common goals, joint work plans, shared resource agreements, and long-term relationships among companies in the same industry, such as risk, benefits, planning, and technology sharing [3].

The case study company manufactures and distributes automotive and agricultural machinery parts to industrial operators, such as agricultural machinery. The company also exports agricultural machinery parts to domestic customers. Currently, the company aims to produce 350 units per day, but with the existing production system, it can only produce 280 units per day. To meet this target, overtime work is required, as customers prioritize quality and

timely delivery. This places an additional burden on the company in terms of labor costs. Researchers have studied related research to solve production process problems [4] by analyzing process failures using Failure Mode and Effects Analysis (FMEA) and 7 QC Tools. These tools effectively assess the risk of failure modes in systems, processes, designs, or services, enabling accurate assessment of failure risks, identification of critical failures, and application to complex systems [5-7].

This study focuses on analyzing the production process of a factory to implement appropriate engineering management techniques. By examining relevant research and theories, the aim is to improve the production process through the application of Jig fixtures. These fixtures will secure and precisely position workpieces during production, mitigating the risk of human error and increasing overall output. The fixtures will be designed for versatility and adaptability [8-13]. The ECRS principles of Eliminate, Combine, Rearrange, and Simplify will be employed to reduce unnecessary costs, conserve resources, minimize waste, and enhance organizational efficiency [14]. Production balancing will be implemented to reduce variability within the production line, minimize waiting times, and lower costs [15]. Karakuri Kaizen will be utilized to reduce energy consumption, transportation time, and physical strain. Its basic mechanisms include: 1. levers, 2. winches, 3. pulleys, 4. springs, 5. inclines, 6. direction changes, 7. power transmission through rotation, 8. fluids, and 9. magnets. The development of workpiece fixtures will also be a key component [16-18]. These improvements aim to enhance production efficiency by minimizing machine downtime, reducing overtime expenses, and enabling more effective and efficient operations. Additionally, simple tools and fixtures will be developed to improve torque control and reduce excessive force exertion, thereby preventing musculoskeletal disorders (MSDs). The objective of this project is to reduce the actual working cycle time from 96.22 seconds per piece to less than 78 seconds per piece.

2. Study and Method

2.1 Study Production Process

The case study company produces 7,280 parts per month, operating 26 days a month. This means that 280 parts are produced daily, with a daily working time of 7.6 hours. However, the demand for parts is 350 units per day, resulting in a Takt time of 78.17 seconds per unit. Conversely, the actual cycle time is 96.22 seconds per unit, which is a problem due to the nature of agricultural machinery parts as shown in Figure 1, and the workspace as shown in Figure 2.

a) Model 120 b) Model 90

Figure 1 Agricultural machinery part

2.2 Study the work procedures

Collect operational data using a workpiece flow chart to create a Flow Process Chart [19], which presents information on raw materials, employees, production processes, workpieces, and space. Standard time is established for the production process of agricultural machinery spare parts, as shown in Figure 3 and an example of collecting time data of Step 5 as shown in Table 1.

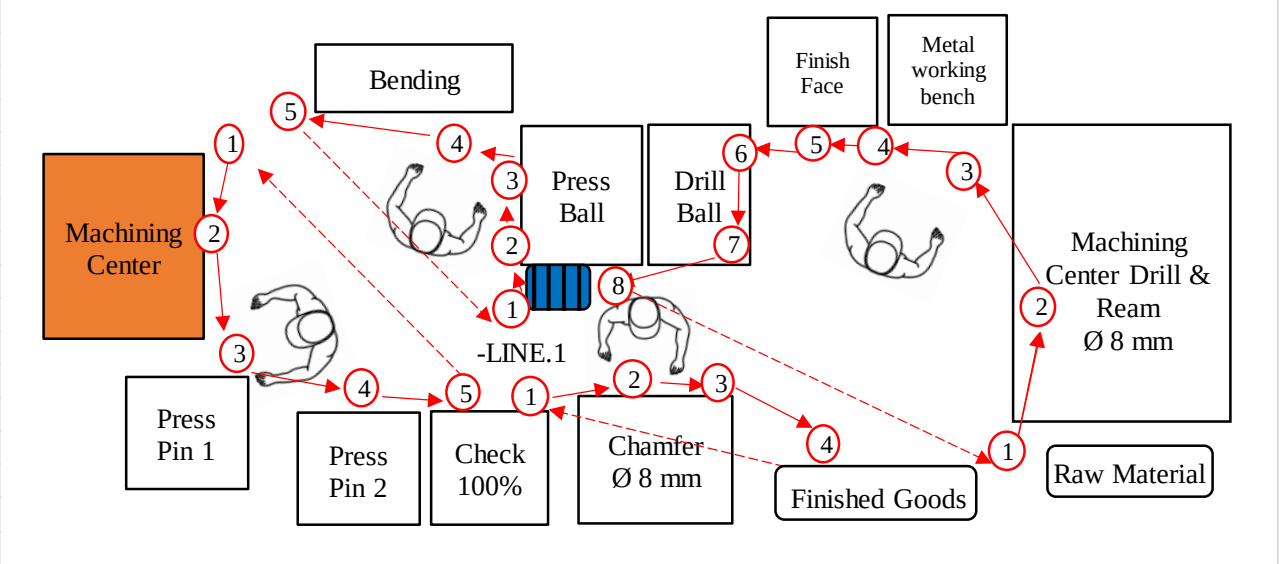

Figure 2 Process line agricultural machinery parts

Figure 2 shows the following machinery

1. R/M: Parts in Storage box
2. Drill & Ream: The process involves drilling and reaming the workpiece.
3. Metalworking bench
4. Finish Face: A machine used for shaping workpieces.
5. Drill Ball: A machine capable of drilling circular holes.
6. Press Ball: A hydraulic press.
7. Bending: A table used for bending or hammering workpieces.
8. Machining Center: An automatic machine (CNC).
9. Press Pin 1: A hydraulic press.
10. Press Pin 2: A hydraulic press.
11. Check 100 percent: A table for placing measuring tools to inspect workpieces.
12. Chamfer Ø 8 mm: A table for checking holes with a diameter of 8 millimeters.
13. F/G: A box for good-quality workpieces.

Table 1 Example of collecting time data for Step 5 (Forming workpiece bottom)

No.	Time (sec)	No.	Time (sec)
1	24.63	16	23.50
2	24.27	17	24.61
3	22.57	18	24.63
4	26.21	19	25.18
5	25.56	20	24.87
6	21.18	21	23.96
7	24.56	22	24.71
8	24.51	23	24.16
9	26.10	24	26.73
10	24.61	25	24.31
11	23.47	26	25.22
12	22.54	27	24.87
13	24.76	28	23.64
14	21.15	29	26.24
15	26.66	30	24.88
		Average	24.48
		Max	26.73
		Min	21.15
		Standard Deviation	1.36

FLOW PROCESS CHART					APPROVER	INSPECTOR	ORGANIZER
LINE NAME	Process	OPERATOR: A	BEFORE	REV.	A	B	C
PART NO:	Door	PART NAME: XX		0			
CHART NO: XX		SHEET NO. X	SUMMARY				
ACTIVITY :			ACTIVITY	PRESENT	Operater		C.T (Sec.)
METHOD:			OPERATION ○	12	Operater 1 (OP1)		94.57
LOCATION:			TRANSPORT ⇨	13	Operater 2 (OP2)		90.56
OPERATOR (S):			DELAY D	3	Operater 3 (OP3)		96.22
OPERATOR (S):			INSPECTION □	8	Operater 4 (OP4)		71.56
CHECK BY: X		DATE: XX/XX/XX	STORAGE ▽	5	The Sum of Process		96.22
APPROVED BY: X		DATE: XX/XX/XX	DISTANCE (m)	30.2			
DESCRIPTION			TIME (Sec)	352.91			

DESCRIPTION	TIME (Sec)	DIST(m)	SYMBOL	REM
1. Incoming Part		25		
2. Check tiny hole and dent	120	0.3		Not taken into account
3. Load and Unload Ream Dia 8 mm	10.74+65			Machine time
4. Strike ball and check	19.94	0.3		
5. Forming workpiece (bottom)	24.48	0.3		OP 1
6. Forming workpiece (top)	18.09			
7. Drill ball and check	21.32	2		
8. Insert workpiece into ball	8.22			
9. Press ball	8.48	0.4		OP 2
10. Bring workpiece to bend by striking	73.86			
11. Load, unload, and machine at the center	25.22+71			Machine time
12. Bring workpiece for grinding	44.63	0.2		
13. Press pin 1	8.52			OP 3
14. Press pin 2	14.84	1		
15. Inspect workpiece in jig	47.85	0.2		
16. Check plug and appearance	16.95			OP 4
17. Check diameter 8mm	6.76	0.5		
รวม	352.91	30.2		

Figure 3 Flowchart of the workpiece before improvement

Figure 3 shows a total cycle time of 352.91 seconds. The analysis reveals that machine idle time contributes significantly to the overall cycle time. This imbalance in process times leads to reduced efficiency, resulting in a cycle time of 96.22 seconds per piece, or an output of 37 pieces per hour. The total travel distance recorded is 30.2 meters.

2.3 Analysis Cause

An analysis of production inefficiencies in the manufacturing process of non-conforming products was conducted, including a root cause analysis. A fishbone diagram, categorized by the 4M factors (Man, Machine, Materials, and Method) [20-22], was used to identify potential causes in Figure 4. These identified problems were then subjected to a Failure Mode and Effects Analysis (FMEA) to assess their severity. Severity, occurrence, and detection scores were evaluated and recorded in Table 2, as per reference [23]. Finally, these problems were prioritized using a Pareto chart in Figure 5

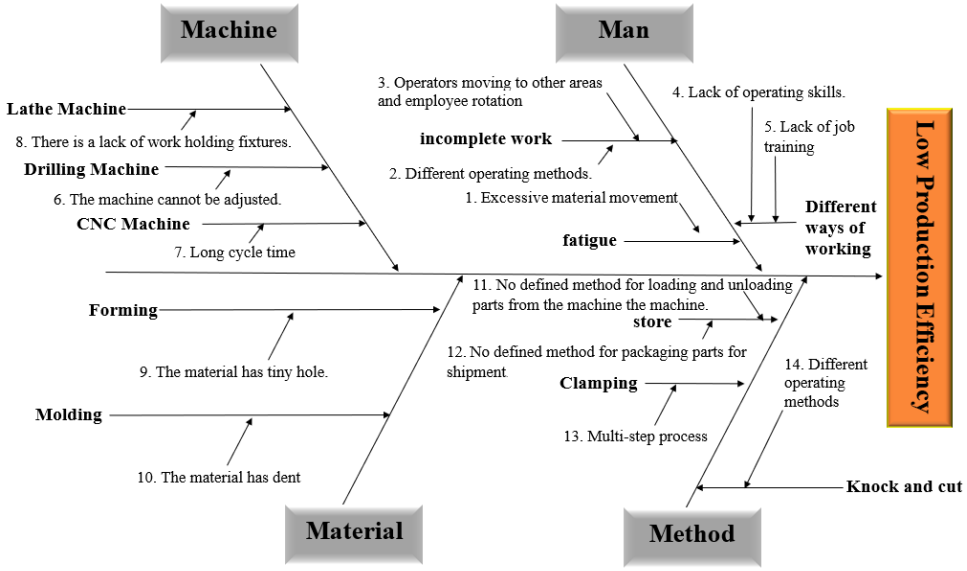

Figure 4 Fishbone diagram

Table 2 FMEA before improvement.

Cause	Problem	S	O	D	RPN
1	Excessive material movement	7	6	4	168
2	Different operating methods	6	3	3	54
3	Operators moving to other areas and employee rotation	2	4	4	32
4	Lack of operating skills	7	4	3	84
5	Lack of job training	7	5	2	70
6	The machine can't adjust	7	10	2	140
7	Long cycle time	2	8	2	32
8	There is a lack of work holding fixtures.	10	3	3	90
9	The material has a tiny hole	2	3	8	48
10	The material has Dents	2	9	2	36
11	No defined method for loading and unloading parts from the machine	3	10	2	60
12	No defined method for packaging parts for shipment	5	8	2	80
13	Multi-step process	5	10	2	100
14	Different operating methods	5	3	2	30

Severity (S) = Severity assessment criteria
Occurrence (O) = Likelihood assessment criteria
Detection (D) = Detection assessment criteria
Risk Priority Number (RPN) = S x O x D

Based on Table 1, the problems with the highest RPN scores were prioritized and visualized using a Pareto chart. The company has decided to focus on issues with an RPN greater than 80 [24] as these have the most significant impact on operations and lead to delays, as illustrated in Figure 5.

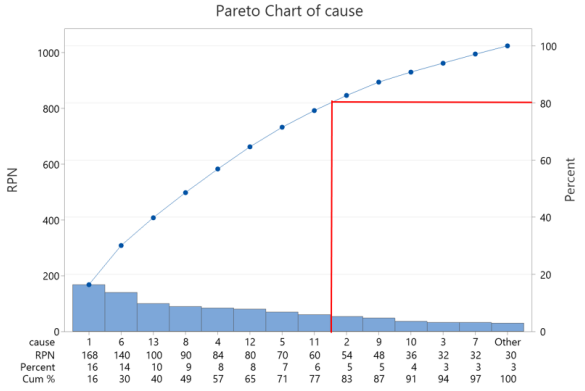

Figure 5 Pareto chart

As shown in Figure 5, a Pareto chart was used to identify and prioritize problems for resolution using the 80:20 rule [25,26]. Problems 1, 6, 13, 8, 4, 12, 5, and 11 collectively account for a significant 80% of the overall issues. These problems will be addressed first.

2.4 Proposed Solutions

Following the process analysis in Figure 5, a detailed examination of the root causes was carried out. To mitigate these issues, engineering management techniques were employed. Table 3 outlines the proposed solutions and their anticipated benefits.

Table 3 Root Causes, Solutions, and Expected Benefits

Case	Solutions	Expected Benefits
1. Excessive material movement	Line balance	Reduced travel distance
6. The machine can't adjust	ECRS	Significant increase in work speed
13. Multi-step process	Design Jig Fixture	Streamlined work processes
8. Work holding fixtures	ECRS	Increased production speed
4. Lack of operating skills	Workforce training	Reduced error rate leads to increased work speed
12. No defined method for packaging parts for shipment	Karakuri	Reduced work time and movement
5. Lack of job training	Training	Employees can learn more about the work process.
11. No defined method for loading and unloading parts from the machine	Work Instructions	Able to work faster

3. Results

3.1 Results of Karakuri Kaizen Implementation

Before the improvements, workpieces were transported via manual labor. By applying the Karakuri Kaizen concept and utilizing the principles of inclined planes and gravity, we have streamlined the process [27]. The modifications have led to a 4 second reduction in task duration, a 2.5 meter decrease in travel distance, and a substantial reduction in the physical exertion required for lifting workpieces. Visual representations of the before and after states are provided in Figures 6 and 7.

Figure 6 Design Karakuri Kaizen

Before After

Figure 7 Before and after Karakuri Kaizen implementation

3.2 Results of ECRS implementation

The redesigned fixture and ECRS implementation aimed to simplify the workflow and enhance workpiece locking speed. By replacing the bolt with a spring mechanism, the improved process involves inserting the workpiece while compressing the spring. Upon release, the workpiece is driven against a stopper. Subsequently, a cam is activated to further secure the workpiece. Additionally, the orange lock has been replaced with a cam lock for streamlined operation. As a result, the third worker's task time has been reduced from 96.22 seconds to 74.51 seconds, as depicted in Figures 8 and 9.

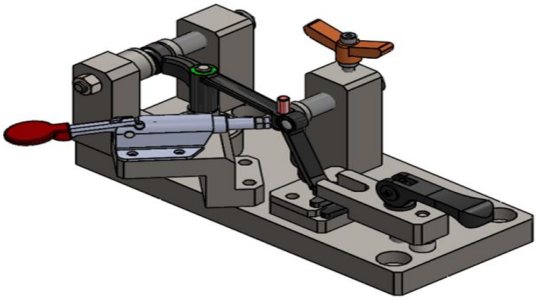

Figure 8 Design Jig Fixture

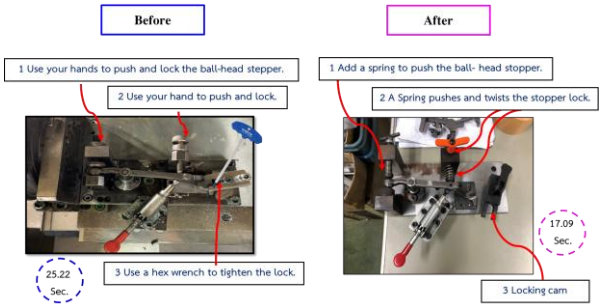

Figure 9 Before and after Jig Fixture implementation

3.3 Results of Jig Fixture Implementation

The original process required the workpiece to be pressed and clamped. The new fixture design, with its added attachment, enables the simultaneous clamping of two workpieces, streamlining the process and reducing task time from 42.57 seconds to 17.09 seconds. The process flow is depicted in Figures 10 and 11.

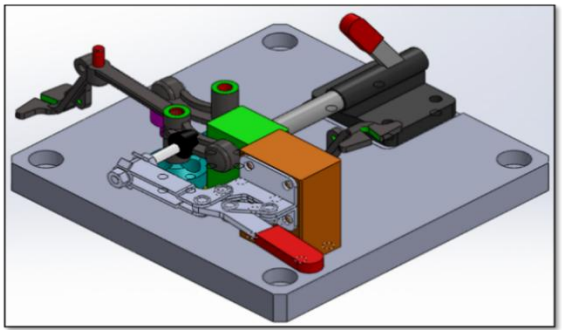

Figure 10 Design Jig Fixture

Before After

Figure 11 Before and after Jig Fixture implementation

3.4 Results of Line Balance Implementation

The rigid setup of the previous machine led to production bottlenecks. To enhance flexibility and streamline operations, a CNC machine has been installed and integrated with the following production stage. This integration ensures a seamless workpiece flow and prevents idle time for operators on the B line. Furthermore, the second workstation has undergone a workforce adjustment due to the integration. These improvements have resulted in a cycle time reduction from 96.22 seconds to 75.22 seconds.

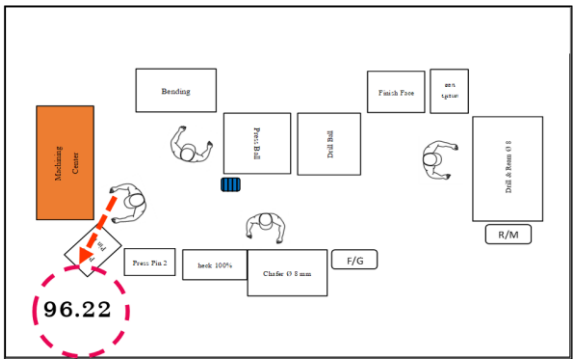

Before

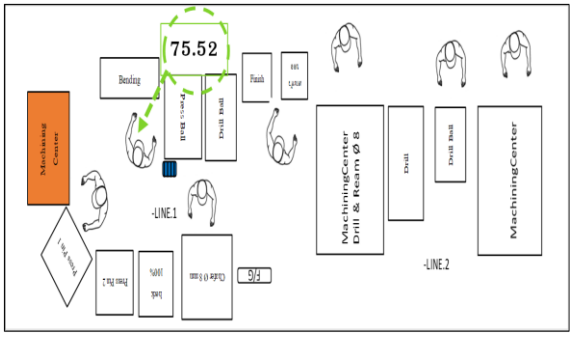

After

Figure 12 Before and after line balance implementation

3.5 Results of Flow Process Implementation

Following the improvements, a post-implementation study was carried out to measure the actual cycle time. Data was collected from each workstation in the modified production line. The results showed a reduction in the number of sub-processes to 13 steps, as depicted in Figure 12, indicating a potential decrease in cycle time.

FLOW PROCESS CHART					APPROVER	INSPECTOR	ORGANIZER
LINE NAME	Process	OPERATOR: A	AFTER	REV.	A	B	C
PART NO:	Door	PART NAME: XX		0			
CHART NO: XX		SHEET NO. X	SUMMARY				
ACTIVITY :			ACTIVITY	PRESENT	Operater		C.T (Sec.)
METHOD:			OPERATION ○	12	Operater 1 (OP1)		54.35
LOCATION:			TRANSPORT ⇨	13	Operater 2 (OP2)		75.52
OPERATOR (S):			DELAY D	3	Operater 3 (OP3)		75.07
OPERATOR (S):			INSPECTION □	8	Operater 4 (OP4)		70.47
CHECK BY: X		DATE: XX/XX/XX	STORAGE ▽	5	The Sum of Process		75.52
APPROVED BY: X		DATE: XX/XX/XX	DISTANCE (m)	27.7			
			TIME (Sec)	275.41			

DESCRIPTION	TIME (Sec)	DIST(m)	SYMBOL	REM
1. Incoming Part		25	● ➡ □ D ▽	
2. Check tiny hole and dent	120	0.3	○ ➡ ■ D ▽	Not taken into account
3. Load and Unload Ream Dia 8 mm	75		● ➡ ■ D ▽	Combine Line
4. *Strike ball*	17.94		● ➡ ■ D ▽	
5. *Forming workpiece (bottom and top)*	17.09		● ⇨ □ ◗ ▽	OP 1
6. Drill ball and check	19.32	0.1	○ ➡ ■ ◗ ▼	
7. Insert workpiece into ball	7.22		● ⇨ □ D ▽	
8. Press ball	8.44	0.4	● ➡ □ D ▽	OP 2
9. Bring workpiece to bend by striking	59.86		● ➡ ■ D ▼	
10. Load, unload, and machine at the center	17.07+58		● ➡ □ D ▽	Machine time
11. Bring workpiece for grinding	31.85	0.2	● ➡ □ D ▽	
12. Press pin 1	6.94		● ⇨ ■ D ▽	OP 3
13. Press pin 2	17.65	1	○ ➡ □ D ▼	
14. Inspect workpiece in jig	46.85	0.2	○ ⇨ ■ D ▽	
15. Check plug and appearance	16.95		○ ➡ ■ D ▼	OP 4
16. Check diameter 8mm	6.67	0.5	● ➡ □ D ▼	
รวม	275.41	27.7		

Figure 13 Flowchart of the workpiece after

The implementation of a new workpiece jig fixture, ECRS, and karakuri kaizen in processes 3 to 6 and 9 to 13, as shown in Figure 1 3, has significantly reduced task times and distances. The first operator's time was reduced by 40.22 seconds, the second by 15 seconds, the third by 21.15 seconds, and the fourth by 1.09 seconds. This resulted in a cycle time of 75.52 seconds per piece, increasing production to 47.54 pieces per hour, and a total daily output of 362 pieces for a 7.6 hour workday.

3.6 Results of Statistical

The post-improvement data was analyzed using a one-sample t-test to test the hypothesis. The null hypothesis (H_0) was rejected if the p-value was less than 0.05, indicating that the alternative hypothesis (H_1) was more likely to be true. Conversely, if the p-value was greater than 0.05, the null hypothesis (H_0) was accepted. This analysis was conducted to determine if the data supported the proposed hypothesis, $H_0 : \mu \leq 78$ $H_1 : \mu > 78$ as shown in Table 4.

Table 4 Results of the one-sample t-test after the improvement

N	Mean	StDev	SE Mean	P-Value
30	75.520	0.840	0.153	1.000

Table 4 presents the results of a one-sample t-test conducted using statistical software on the post-improvement cycle time data. The calculated p-value is 1.000, which is greater than the significance level of 0.05. Therefore, we fail to reject the null hypothesis (H_0). It can be concluded that the mean post-improvement cycle time is less than or equal to 78.17 seconds per unit.

3.7 Results of FMEA implementation

From Table 2, the causes of defects in the production process were identified through collaborative discussions with production staff and inspectors. It was found that after implementing corrective actions, the Risk Priority Number (RPN) decreased, indicating that the solutions effectively reduced the occurrence of defects, as shown in Table 5 and Figure 15.

Table 5 FMEA After improvement.

Cause	Problem	S	O	D	RPN	
					Before	After
1	Excessive material movement	7	3	4	168	84
2	Different operating methods	6	3	3	54	54
3	Operators moving to other areas and employee rotation	2	4	4	32	32
4	Lack of operating skills	7	4	2	84	56
5	Lack of job training	7	3	2	70	42
6	The machine can't adjust	7	1	2	140	14
7	Long cycle time	2	8	2	32	32
8	There is a lack of work holding fixtures.	7	3	3	90	63
9	The material has a tiny hole	2	3	8	48	48
10	The material has Dents	2	9	2	36	36
11	No defined method for loading and unloading parts from the machine	3	10	1	60	30
12	No defined method for packaging parts for shipment	5	4	2	80	40
13	Multi-step process	4	10	2	100	80
14	Different operating methods	5	3	2	30	30

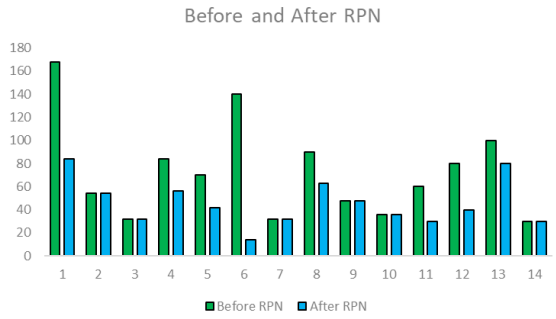

Figure 15 Compare RPN scores before and after

3.8 Analyze the improvement results

After implementing engineering improvements to the production process, the cycle time was significantly reduced from 352.91 seconds to 275.45 seconds, representing a 21.95% decrease. This improvement resulted in an increased daily production from 280 units to 362 units, exceeding the target of 350 units per day. Additionally, the working distance was reduced by 2.5 meters, as illustrated in Table 6 and Figures 16 and Figures 17 for detailed data.

Table 6 Improvement results analysis

Improvement	Cycle Time (sec/piece)	Production Quantity (pieces)	Distance (m)
Before	96.22	282	30.2
After	75.52	362	27.7

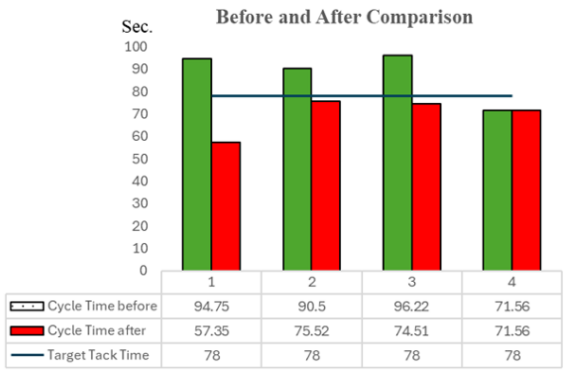

Figure 16 Cycle time before and after improvement

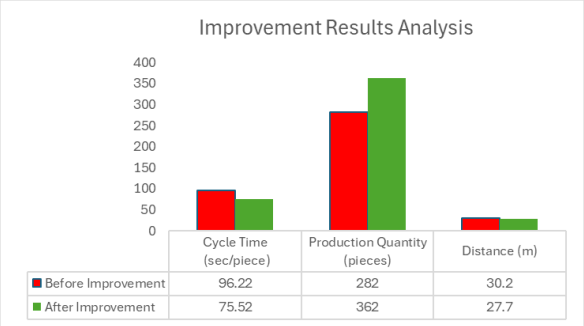

Figure 17 Improvement Results

4. Discussion

A case study of an agricultural parts manufacturing company revealed a production bottleneck due to an inability to meet demand. Researchers employed engineering principles, quality control tools, and Failure Mode and Effects Analysis (FMEA) to identify and mitigate risks associated with the production process. FMEA proved to be an effective tool in pinpointing potential problems and their associated impacts.

The majority of improvements involved equipment replacement, sharing of machinery among production lines, and the addition of work-holding fixtures to reduce process steps. A redesigned fixture was developed to enhance the efficiency of agricultural machinery parts production. Techniques such as ECRS, Jig fixture design, karakuri, and production balancing were employed to identify targeted improvement areas [28-30].

Data collection revealed a significant reduction in cycle time from 96.22 seconds to 75.52 seconds, representing a 21.74% decrease. Similarly, the total working distance decreased from 30.2 meters to 27.7 meters, a reduction of 8.28%. Overall line efficiency increased from 66.24% to 97.23%, a 30.99% improvement. The production cycle time was consistently maintained below 78 seconds per unit.

5. Conclusions

This research highlights the novel application of Karakuri Kaizen and Jig Fixture Design to address production bottlenecks in the manufacturing process of agricultural machinery parts. the root causes of the problem were identified. To address the issues, the researchers applied the karakuri kaizen principle, leveraging gravity, weight, and inclination, as well as implementing workpiece holding fixtures to reduce operator fatigue and cycle time. Additionally, the balancing of shared machinery streamlined the production process and minimized operational steps. As a result, the cycle time was significantly reduced from 352.91 seconds to 275.45 seconds, representing a 21.95% decrease. This improvement led to a daily production of 362 units, surpassing the previous output of 280 units. The primary limitation of this study lies in its focus on a single case, which restricts the generalizability of the findings to other industries or operational contexts. Additionally, the initial investment required for the design and implementation of Jig Fixtures may present financial challenges, particularly for small or resource-constrained organizations. Future research should explore the application of these methodologies-specifically Karakuri Kaizen and Jig Fixture implementation, across a wider range of manufacturing sectors to validate the results. Further studies should also address the long-term sustainability and cost-effectiveness of these approaches to support broader industrial adoption.

6. Acknowledgment

We would like to acknowledge the invaluable support of the Case study company, whose data, cooperation, and detailed explanations were instrumental in the successful completion of this research.

7. References

[1] Thanakorn M, Worawit L, and Wannawisa U. Time Series Forecasting of Automotive Component Production. Acad J. Sci Technol. (AJST). 2023;1(3):185-200.

[2] Jetnipat P, et al. Waste Reduction in the Assembly Process of Valve Production. Proceedings of the 14th Engineering Science Technology and Architecture Conference on Industrial engineering. 2023 Aug 25-26; Mung, Thailand. Kalasin; 2023;1348-1355.

[3] Napaporn A, Patchara W. The Inventory Management for Motor Vehicles Replacement Equipment in Wholesale Trade Sector Influence in Response to Customer Requests. Mahamakut Grad Sch J. 2019; 17 (2):218-232.
[4] Thamrong G. Enhancing efficiency in the production line of agricultural machinery components. B. Eng Thesis. Rajamangala University of Technology Isan; 2024.
[5] Peter M, Naqib D. Production line automation project based of FMEA method. MM Sci J. 2020; 13(1):3912-3917.
[6] Jittiwat N. QC 7 Tools in: Quality Control. Bangkok: OS Printing House; 2022;51-109.
[7] Rattawut V. Development of maintenance systems by Failure Modes and Effects Analysis (FMEA) techniques: a case study of concrete products industry. J. Eng Innov. 2023; 16(3):59-69.
[8] Nor Azinee S, Muhammad Afiq R, Norsilawati N, et al. Design and Fabrication of Jig and Fixture for Drilling Machine in the Manufacturing Industry to Improve Time Productivity. J. Adv Res Appl Sci Eng Technol. 2023; 29(2):304-313.
[9] Harshwardhan CP. Jigs and Fixtures in Manufacturing. Int J. Eng Res Appl. 2022; 12(10):50-55.
[10] Syed Mustafa H, Abbas H, Shaheryar Atta K, Naeem S, Amir N. Design, Fabrication, and Analysis of a Precision Drilling Jig for Waste Reduction: A Low-cost Solution. J. Kejuruteraan. 2024; 36(1):259-271.
[11] Kataria Mahendra B, Patel Neha H, Bhimani J. Design and Development of JIG for an Auto Part. Int J. Eng Dev Res. 2017; 5(1): 748-753.
[12] Charles Chikwendu O, Ezeanyim Okechukwu C. The Design and Need for Jigs and Fixtures in Manufacturing. Sci Res. 2015; 3(4):213-219.
[13] Jetnipat P, Surachai N, Worawut P, Jittiwat N and Wannisa N. Design Jigs and Fixtures to Reduce Time in the Bevel Milling of Workpiece. J. Manuf Manag Technol. 2024; 3(1): 38-48.
[14] Nuchsara K, Preecha K, Parinya P. Silver Box Production Efficiency Improvement: A Case Study. J. Sci Technol. 2022; 24(3): 30-38.
[15] Vijay S, Gomathi Prabha M. Work standardization and line balancing in a windmill gearbox manufacturing cell: A case study. Materials Today: Proceedings. 2020; 49:9721-9729.
[16] Pichawadee K, et al. Development of Material Handling Equipment in a Paint Factory with Karakuri Kaizen. J. King Mongkut's Univ Technol. 2024; 34(3): 1-17.
[17] Pakpoom J, Siwasit P, Suwannee S, Nuhjarin S and Parida J. Improvement of Motorcycle Wheel Hubs Conveyor rail Process by Poka-yoke Techniques. Ladkrabang Eng J. 2023; 40(2):138-146.
[18] Chaiwat K, et al. Productivity improvement of material handling using Karakuri Kaizen handtruck: A case study of Phuwiangwari community enterprise. RMUTSB Acad J. (Humanit. Soc. Sci.). 2024; 12(1):80-92.
[19] Krittapak P, et al. The case study company implemented the kaizen technique to improve the efficiency of control component manufacturing process. Proceedings of the 14th Engineering Science Technology and Architecture Conference on Industrial engineering; 2023 Aug 25-26; Mung, Thailand. Kalasin; 2023; 1391-1396.
[20] Chatpon P, Banthita P Ponatong and Siwaporn N. Waste reductionin khao tu production process of agriproduct processing groups. Ind Technol J. 2022; 7(2):113-122.
[21] Mongkol K, Ariyapong P, Ratchaneekorn D, Thiwarat S and Narathip P. Marketing Strategies Formulation Using Sale Reduction Root Cause Analysis: A Case Study of Herbal Soap Community Enterprise. Thai Ind Eng Netw J. 2023; 9(1):74-86.
[22] Jiranan K and Prachuab K. Reducing the Failure Rate of Dishwashersby Analyzing the ServiceLife of Spare Partsusing System Reliability Calculation. J. Ind Technol. 2023; 19(1):1-16.

[23] Warathorn P. Failure Mode and Effects Analysis for a Maintenance System Development: A Case Study of Meat Processing. Ladkrabang Eng J. 2016;33(4): 24-31.
[24] Wu Z, Liu W, Nie W. Literature review and prospect of the development and application of FMEA in manufacturing industry. Int J. Adv Manuf Technol. 2021;112(6):1409-1436.
[25] Suphawat M and Jeerawat P. Deffects reduction in polymer solid capacitor production process. Kasem Bundit Eng J. 2017;7(1):105-122.
[26] Daniel M. McCarthy and Russell S. Winer. The Pareto rule in marketing revisited: is it 80/20 or 70/20?. Mark. Lett. 2019;30(2):139-150.
[27] Aynur GÜRSOY ÖZCAN. Application of reba and karakuri kaizen techniques to reduce ergonomic risk levels in a workplace. J. Eng Sci Des. 2022;10(40:1430-1444.
[28] Jaruwan P and Teerapat J. Machine Maintenance Planning for Pelletizing Processes using FMEA Technique, A Case Study of the Pellet Biomass Factory. J. Ind Technol. 2020;8(1):1-12.
[29] Panya S, Naphob S, Suphot R, Burapa D, Sumet P, Wasan R and Ploypailin V. The Improving Productivity in Seasonal Product Manufacturing by Motion and Time Study and Jig Design. Thai Ind Eng Netw J. 2024; 10(1):51-59.
[30] Kataria M, Bhimani J. Design and Development of jig for an auto part. Int J. Eng Dev Res. 2017;5(1):748–753.

Time Series-Based Predictive Modeling of PM2.5 Levels in Chiang Mai, Thailand

Tewa Promnuchanont[1], Theeraphop Saengsri[1*], Rujipan Kosarat[2], Piyaphol Yuenyongsathaworn[2]
[1]Department of Computer Information System, Faculty of Business Administration and Libera Arts,Rajamangala University of Technology Lanna, Chiang Mai, Thailand
[2]Department of Software Engineering, Faculty of Engineering, Rajamangala University of TechnologyLanna, Chiang Mai, Thailand
128 Huay Kaew Road, Muang, Chiang Mai, Thailand, 50300
[*]Corresponding Author: tees@rmutl.ac.th. Phone Number: +66-869202820
Received: 3 December2024, Revised: 7 May 2025, Accepted: 23 May 2025

Abstract
The purpose of this study is to use a variety of models to create prediction models for Chiang Mai's PM2.5 levels. To improve the accuracy of our predictions, we take into account outside variables that might influence PM2.5 levels. Among the variables that we include in the data are PM2.5 concentrations, temperature, wind speed, precipitation, cloud cover, relative humidity, and other external factors. Before using the model, the researcher used basic statistical analysis, seasonal analysis, and stationary analysis to assess the data. The team of researchers carried out both data transformation and data cleansing. We tested the ARIMA, SARIMA, and SARIMAX forecasting models. First, we use ARIMA to forecast and assess results. The SARIMA model more accurately captured the seasonal connection in the data when we included a seasonal component. The model was able to forecast PM2.5 levels more precisely at times when seasonal patterns recurred thanks to this improvement. As the last step, we used the SARIMAX model to improve performance by adding exogenous variables. In the end, we assessed the accuracy and performance of each forecast using the MAE and RMSE numbers. The ARIMA model yielded MAE values of 7.34 and RMSE 7.95. The SARIMA model MAE values of 5.76 and RMSE 6.54. The SARIMAX model, when incorporating humidity, had the lowest MAE values of 4.36 and RMSE 5.25, representing improvements MAE of 40.6% and RMSE 34% compared to ARIMA.
Keywords: PM2.5, ARIMA, SARIMA, SARIMAX, Forecast Model

1. Introduction

Dust, a common environmental issue, has detrimental effects on both human health and the ecosystem. Dust is a term that refers to the minute particles that are floating in the atmosphere. These particles may vary greatly in size and composition, with some even being tiny enough to enter an individual's respiratory system. There are a number of major health hazards associated with small particles, including cardiovascular and pulmonary issues. We often divide small particles into categories of PM10 and PM2.5 categories. Due to its interactions with environmental systems, dust not only impacts health, but also influences climate change; especially when it contains harmful greenhouse gases. Finding solutions that improve the environment and human health requires an understanding of the sources, effects, and necessary mitigation techniques of dust pollution. PM2.5 may originate from a number of sources, such as vehicle emissions, wildfires, and industrial operations. By reducing air quality, PM2.5 worsens environmental problems, including poor sight and climate change, in addition to its negative health impacts. Knowledge of PM2.5 sources, effects, and mitigation strategies is essential for improving human health and protecting the environment. The forecast of PM2.5 levels is essential for maintaining air quality and safeguarding human health. Serious health risks may arise from particulate matter with a diameter of 2.5 micrometers or smaller, or PM2.5, which can enter the bloodstream and penetrate deeply into the lungs. Accurate PM2.5 level estimates may help individuals and communities prevent exposure, take effective action, and anticipate and solve air quality issues.

In today's world of rapid change, data mining has grown in importance due to the exponential growth in data collecting. Data mining uses sophisticated techniques rather than just extracting data to find valuable information hidden in massive datasets. In order to develop sophisticated artificial intelligence models, find patterns, and facilitate informed decision-making, it involves using deep technologies and complex algorithms. Businesses, academic institutions, and other organizations of various kinds may utilize this ability to identify important trends across a range of industries. Many different areas, including forecasting commercial trade, targeted marketing plan development, and medical research, employ data mining.

The use of data mining techniques has made it possible to develop new methods for displaying and analyzing data. Regression analysis accomplishes the separation of dependent factors and independent variables [1], classification models make educated guesses about the categories that individuals belong to, anomaly detection [2] pinpoints problems, association rule mining [3] illustrates the connectivity of data, and text mining [4] extracts meaning from text data. Time series analysis (ARIMA) [5] examines and forecasts data gathered over time. Hierarchical structures are used by decision trees [6] to assist individuals in making decisions. Ensemble approaches use multiple models to make predictions more accurate. And neural networks [7] try to work like the brain. The optimal data mining technique depends on the specific goals and types of data.

This project aims to develop prediction models for PM2.5 levels in the Thai region of Chiang Mai, which has annual PM2.5 dust pollution. We have evaluated the forecast model using three models: SARIMA, ARIMA, and SARIMAX. ARIMA is used for modeling time-dependent data that exhibit trends and autocorrelation. SARIMA is built upon ARIMA by including seasonal components, which are essential for capturing the yearly patterns often observed in environmental data such as PM2.5. Forecasting is further enhanced by SARIMAX through the incorporation of external variables, such as weather conditions, which are known to influence PM2.5 levels. These models are widely applied to support early warning systems and inform environmental policies aimed at reducing public health risks.

In the test, the test component used data from January 2023 to December 2023 for 12 months, while a 60-month data from January 2018 to December 2022 was used to predict the PM2.5 levels for the whole year of 2023. The structure of this work describes the setup as follows: Section 2 provides a review of various earlier studies directly related to this subject, while Section 3 discusses the technique. Section 5 concludes this article with a presentation and discussion of the results from Section 4.

2. Literature review

According to research, PM2.5 and PM10 are two different kinds of dust, each having its own origins and chemical makeup [8]. The particles that make up particle pollution are separated into two categories, according to Chen et al [9], PM10 contains particles as tiny as 10 microns, whereas PM2.5 contains particles as small as 2.5 microns. PM2.5 contains carbonaceous material and metal compounds that may be harmful to both people and the environment The atmosphere disperses these particles in different ways, according to Singh et al [10], and PM10 often reflects coarse-mode PM, such as dust carried by the wind. The study used the Nested Regional Climate and Chemistry Model (NRCM-Chem) to predict PM2.5 concentrations over the northern peninsula of Southeast Asia during 2020–2029 under the RCP8.5 scenario. The model showed good agreement with observed data, with an Index of Agreement (IOA) between 0.63 and 0.80, although it slightly underestimated temperature and precipitation and overestimated PM2.5 levels [11].

The intersection of big data, machine learning, and data mining is a fast-growing subject with enormous potential for a broad variety of possible applications at every stage of its development. Singh highlights how machine learning may be able to help with the difficulties that come with large data analytics [12]. Yang C, Huang Q, and et al [13] both stress the value of data mining as a

technique for drawing insightful conclusions from large and intricate data sets. Furthermore, they look at the different kinds of big data and the difficulties that come with them. Wang S and Cao J's [14] article delves deeper into the use of data mining methods and the applications of big data processing. The research looks more closely at various applications and focuses on the diverse nature of huge data.

ARIMA has been the subject of several research studies in the fields of data mining and projected outcomes. Díaz-Robles LA, Ortega JC and et al [15] used an upgraded ARIMA model for air quality prediction and achieved better results by using a sliding window technique and forecasted data. The integration of the data made this possible. Lee, Dongwon, and et al [16] achieved a low average error rate, while Khashei M and Bijari M [17] likewise discovered that ARIMA was effective in predicting time series data. Shivhare N, Rahul AK, and et al [18] has developed tools for daily weather forecasting and proposed an ARIMA method for weather data mining that is based on Hadoop. These research findings illustrate the utility of ARIMA in data mining and prediction activities. Other research results demonstrate the usefulness of ARIMA in other fields. The results of this research illustrate the adaptability and use of ARIMA in the field of data mining.

According to earlier research, there were a number of obstacles in PM2.5 forecasting, such as significant environmental variability, difficulties in capturing abrupt pollution spikes, and limitations in data completeness and resolution. To address these challenges, models were required that could manage missing or inconsistent data, incorporate external factors, and handle seasonality. The combination of many forecasting models, such as ARIMA, SARIMA, and SARIMAX, plus the addition of other exogenous factors to increase predicted accuracy set this study apart from earlier investigations. This study examined the relative effectiveness of several models and showed how external meteorological elements might greatly improve forecasting accuracy, while previous studies often relied on a single model or just looked at past PM2.5 data.

3. Methodology

A structured time series forecasting flowchart was the primary program of the proposed algorithm, as shown in Figure 1. Data entry comes first, followed by analysis and cleaning. Before establishing the ARIMA, SARIMA, and SARIMAX models, we made changes to the cleaned data. With this model, we made predictions and we corrected for poor model performance. The technique produced excellent analysis and outcomes. This method generated accurate forecasts by fine-tuning the model in response to performance assessments.

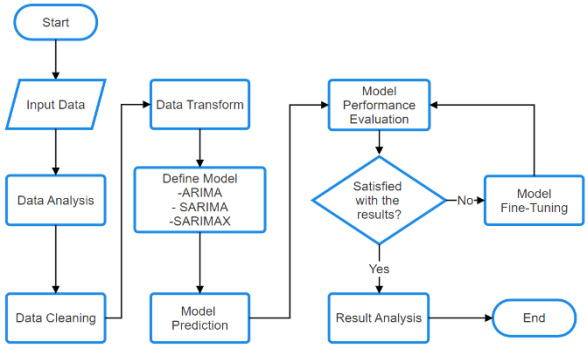

Figure 1 the primary program of the suggested approach.

3.1 Dataset

The comprehensive data from several sources was included in the dataset used to study PM2.5 levels, which improved the analysis's resilience. The PM2.5 information came from Berkeley Earth (https://berkeleyearth.org), which provided detailed records of particulate matter concentrations [19]. Visual Crossing (https://www.visualcrossing.com) provided essential meteorological context by retrieving external data; including temperature, cloud cover, relative humidity, and wind speed. An additional source of environmental information was rainfall data from the Hydrological Information Institute (https://www.hii.or.th) [20]. By combining these datasets, the research was able to more accurately identify the factors influencing PM2.5 levels more accurately, yielding more useful conclusions and recommendations for managing air quality and understanding environmental impacts.

3.2 Data preprocessing

We formatted the obtained data in this stage so that it cloud be used for other forecast. Data preparation is an essential step in the data analysis pipeline that ensured the data was accurate, consistent, and ready for analysis. We converted raw data into a format suitable for analysis, cleaning, and transformation to achieve for more accurate and insightful results. To identify stationary, seasonality, and seasonal decomposition data, we examined the processes involved in the data analysis procedure. After that, the data transformation procedure included converting daily data into monthly data, removing anomalies, and using averages to fill in the missing days.

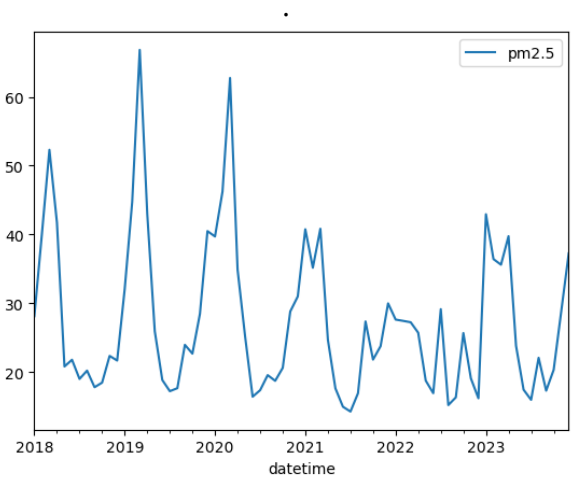

Figure 2 Chiang Mai, Thailand's basic information on PM2.5 levels.

The 2218-day collection of PM2.5 data for Thailand's Chiang Mai province provided crucial information on the air quality in that area. Data transformation involved several steps. Outliers were removed, and missing values were filled using the average of the available data. The daily data were then aggregated and converted into monthly data. For model evaluation, the dataset was divided into two parts. The training set consisted of 60 months of monthly data, from January 2018 to December 2022. The testing set included 12 months of data, from January 2023 to December 2023, and was used to forecast the PM2.5 values for the entire year of 2023. The average PM2.5 level was 27.24 µg/m³, which was considered moderate pollution by the Air Quality Index (AQI). Air quality fluctuated significantly, as seen by the standard deviation of 19.41 µg/m³, which demonstrated substantial variability in daily pollution levels. The variability was further shown by the data, which displayed a broad range of PM2.5 values, from a low of 3.67 µg/m³ to a maximum of 126.44 µg/m³. According to the distribution analysis, the 25th percentile (Q1) was 12.51 µg/m³, meaning that the air was comparatively clean for 25% of the days. PM2.5 levels were at or below this threshold on half of those days, as shown by the median (Q2) of 20.84 µg/m³. The 75th percentile (Q3), which indicated that 25% of those days had greater pollution levels, was 37.24 µg/m³. Even though Chiang Mai occasionally experiences low pollution levels, the city frequently experiences moderate to high PM2.5 levels, with notable daily fluctuations. Figure 2 illustrates how important this data is for planning public health initiatives, and for those who are sensitive to changes in air quality.

A time series analysis's ability to determine whether the data is stationary or if its statistical properties remain constant across time was essential for its success. There were a number of ways to do this. For visual assessment, we plotted the data to see whether the mean and variation were seasonal and stable. It was possible to determine the unit root using statistical methods like the Augmented Dickey-Fuller (ADF) test. Without it, the data remains stagnant. When the autocorrelation function (ACF) and the partial autocorrelation function (PACF) were analyzed, it was possible to determine whether or not the relationships in the data had deteriorate with time.

Time series analysis requires determining whether the data was stable and if its statistical features stayed constant. To find a unit root, one can either display the data and determine whether the mean and variance remain constant, or they can use statistical tests such as the Augmented Dickey-Fuller (ADF) test, as outlined in Eq. (1). Both null hypotheses assume unsteady data. This test should have a p-value of 0.05 or less to reject the null hypothesis.

$$\Delta y_t=\alpha+\beta t+\gamma y_{t-1}+\sum_{i=1}^{p}\delta_1\Delta y_{t-i}+\epsilon_t \quad (1)$$

where Δy_t the time series' initial difference,
y_t, γy_{t-1} the time series' delayed level,
α is an optional constant term,
βt is an optional trend term,
ϵt is the error term,
p is the model's number of lag differences,
$\sum_{i=1}^{p}\delta_1\Delta y_{t-i}+\epsilon_t$ is the Sum of time series lagged differences to adjust for higher-order autocorrelation.

The following were the ADF test results: There were 60 observations, the p-value was 0.766, and we employed 11 lags. These findings implied that we were unable to rule out the ADF test's null hypothesis, which showed that the time series was not stationary. The results of the ADF test suggest that we could validate the unit root or non-stationary nature of this data with a p-value of 0.05.

After that, time series analysis used the autocorrelation (ACF) and partial autocorrelation (PACF) functions to understand the correlations between the data [21]. The ACF method evaluated the connection between the present data value and the future data value (lag) without taking into consideration any additional factors in the data. Through the consideration of intermediate lag correlations, PACF was able to discover independent links between the values of the present data and those of the distant data.

The Autocorrelation Function (ACF) for a time series $\{X_t\}$ at lag k is defined as seen by Eq. (2).

$$\rho_k=\frac{Y_k}{Y_o} \quad (2)$$

where Y_k is $Cov(X_t,X_{t-k})$ for any i.
$Cov(X_t,X_{t-k})$ is the covariance between X_t to X_{t-k}.
Y_o is the variance of the stochastic process.

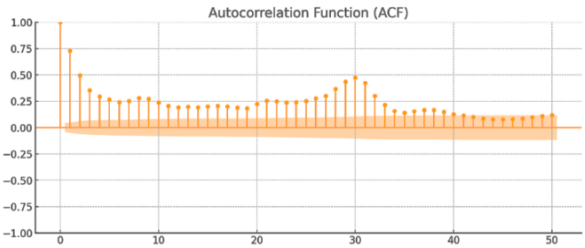

Figure 3 The autocorrelation (ACF).

From Figure 3. The ACF graph shows the relationship between current and lag values. Its periodic decline reveals seasonality. The ACF graph's cyclical rise and fall validates data seasonality by showing a recurrent and consistent correlation across periods.

The Partial Autocorrelation Function (PACF) is a statistical tool that quantifies the degree of correlation between a time series and its delayed values. This function took into consideration the influence of intermediate delays. In the PACF at lag k, the direct link between X_t and X_{t-k}. was calculated after the contributions of intermediate delays had taken into consideration. In the next regression model, Eq. (3) shows how to estimate the PACF at lag k, which is shown by $\emptyset_{kk}$ as the coefficient of X_{t-k}.

$$X_t=\emptyset_{1k}X_{t-1}+\emptyset_{2k}X_{t-2}+\ldots+\emptyset_{(k-1)}X_{t-(k-1)}+\epsilon_t \quad (3)$$

where X_t is the partial autocorrelation coefficient at lag k,
ϵ_t denotes the residual.

For an autoregressive (AR) process, PACF may be computed using recursive connections derived from the Yule-Walker equations. To calculate the PACF at lag k, use Eq. (4).

$$\emptyset_{kk}=Corr(X_t, X_{t-k} \mid X_{t-1},\ldots, X_{t-(k-1)}) \quad (4)$$

The PACF (Partial Autocorrelation Function) graph that is shown in Figure 4 indicates a direct link that exists between the current values and the lagged values. This graph takes into consideration the effect of other lagged data as well. The existence of substantial spots in the PACF graph at lags that correspond to seasonal periods, i.e. around 12 months, is additional evidence that the data exhibited seasonality. This was evidenced by the fact that the PACF graph contains significant spots. The evidence of seasonal patterns was enhanced by these notable spikes, which demonstrate that there was a clear association between the data and values from previous seasonal periods. This gives credence to the notion that seasonal patterns existed.

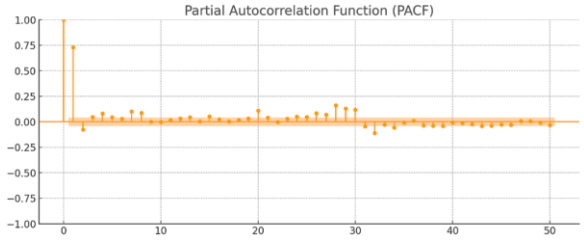

Figure 4 The partial autocorrelation (PACF).

In the last step of data analysis, seasonal decomposition breaks down the data to better understand its patterns and properties. Separating the trend, seasonal, and residual data. This was a typical seasonal breakdown. The trend component showed a long-term data evolution to identify long-term growth or reduction. Seasonality captures trends that occur monthly, quarterly, or annually to indicate short-term changes that follow a cycle. Once we eliminated trends and seasonal effects, the residual component reveals random data fluctuations or deviations that neither a trend nor seasonal factors can explain. Breaking the data into various components helped us understand and analyze the time series.

Figure 5 illustrates the seasonality and non-stationarity of Chiang Mai's PM2.5 data from 2018 to 2023. The ADF test and seasonal decomposition analysis p-values over 0.05 indicated data instability. The breakdown graph shows trends and seasonality components in the data. The monthly PM2.5 data for Chiang Mai shows distinct seasonal patterns and trends.

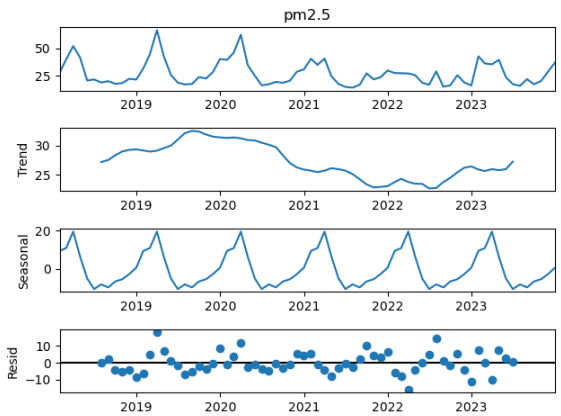

Figure 5 2018–2023 Chiang Mai PM2.5 seasonal component decomposition.

3.3 Model prediction

To assess the study's prediction effectiveness based on the examination of PM 2.5 data in Chiang Mai Province, the researchers used three models: ARIMA, SARIMA, and SARIMAX [22].

A technique known as ARIMA, which is an acronym that stands for autoregressive integrated moving average, was used by us for the aim of assessing and predicting time series data that displays seasonality, patterns, or instability. ARIMA is comprised of three components: MA, I, and AR. We made use of differencing in order to decrease trends and stabilize the data; MA makes use of moving averages of prediction mistakes in order to boost accuracy; and AR makes use of past values in order to anticipate future values. All of these techniques were used in parallel. ARIMA is able to manage time-series data that is both unstable and intricate when both components are mixed inside the model.

It was possible to represent the ARIMA model equation in terms of its constituent parts. Eq. (5) displays the generic form of the ARIMA *(p, d, q)* model for a time series Y_t.

$$y_t = c + \emptyset_1 y_{t-1} + \ldots + \emptyset_p y_{t-p} - \theta_1 \epsilon_{1-1} - \ldots - \theta_q \epsilon_{t-q} + \epsilon_t \quad (5)$$

where y_t is the actual value at time *t*,

c is a constant term,

$\emptyset_i$ are coefficients for autoregressive terms,

θ_i are the coefficients for moving average terms,

ϵ_t is the time-*t* error term.

When $d>0$, replace Y_t with its Δ^d differences $\Delta^d Y_t$ for stationarity, as described in Eq. (6)-(7). ARIMA successfully models and forecasts time series data using AR, differencing, and MA terms.

$$\Delta Y_t = Y_t - Y_{t-1} \quad (6)$$

$$\Delta^d Y_t = \Delta(\Delta^{d-1} Y_t) \quad (7)$$

SARIMA adds seasonal components to the ARIMA model. The SARIMA model is defined as SARIMA $(p, d, q) \times (P, D, Q)_s$, Eq. (8) represents the SARIMA model.

$$y_t=c+\emptyset_1 y_{t-1}+\ldots+\emptyset_p y_{t-p}-\theta_1\epsilon_{1-1}-\ldots-\theta_q\epsilon_{t-q}+\Phi_1 y_{t-s}+\ldots+\Phi_P y_{t-Ps}-\Theta_1\epsilon_{1-s}-\ldots-\Theta_Q\epsilon_{t-Qs}+\epsilon_t \quad (8)$$

where L is the lag operator,

$\emptyset_i$ and Φ_i are Coefficients of the non-seasonal AR terms,

θ_i and Θ_i are Coefficients of the non-seasonal MA terms,

ϵ_t is the white noise,

s is the seasonal period.

SARIMAX adds exogenous regressors to the SARIMA model. SARIMAX incorporates wind speed, rainfall, relative humidity, temperature, and cloud cover. We added one external variable to each test. The SARIMAX model is defined as $(p, d, q) \times (P, D, Q)_s$ with exogenous variables X_{it}. Eq. (9) represents the SARIMAX model.

$$y_t=c+\emptyset_1 y_{t-1}+\ldots+\emptyset_p y_{t-p}-\theta_1\epsilon_{1-1}-\ldots-\theta_q\epsilon_{t-q}+\Phi_1 y_{t-s}+\ldots+\Phi_P y_{t-Ps}-\Theta_1\epsilon_{1-s}-\ldots-\Theta_Q\epsilon_{t-Qs}+\beta_1 X_{1,t}+\ldots+\beta_k X_{k,t}+\epsilon_t \quad (9)$$

where L is the operator of lag,

$\emptyset_i$ and Φ_i are the parameters of AR, θ_i ,

Θ_i are the parameters of MA,

β_k are coefficients of the exogenous variables.

ϵ_t is the forecast error,

X_{it} are the exogenous variables.

3.4 Model performance evaluation

For the purpose of the test, the data was collected over a period of twelve months, commencing in January 2023 and finishing in December 2023. On the other hand, the data for the train component was collected over a period of sixty months, beginning in January 2018 and ending in December 2022. A total of three models, namely ARIA, SARIMA, and SARIMAX, was used by us in order to carry out the procedure. Through the use of two distinct optimization methodologies, we were able to enhance the correctness of the product. First, the SARIMA model's parameters were adjusted using grid search. Grid Search lets you change the model's parameters by giving each parameter a range, and carefully examining every possible combination. This process finds the set of parameters that yields the highest accuracy. Grid search systematically looks at every potential combination of parameters to improve prediction accuracy and optimize model performance.

In an effort to achieve more precision, we included external components into the SARIMAX model. We made observations on the amount of precipitation, relative humidity, temperature, cloud cover, and wind speed. The model incorporates these variables to increase forecast accuracy by adding crucial components that may affect time series data. We used MAE and RMSE to test the SARIMAX model with these external regressors. These metrics, which compute the average magnitude of errors and the square root of the average of squared errors, demonstrate the accuracy of the model. Our prediction model accuracy statistic is Mean Absolute Error (MAE). Mean absolute error (MAE) shows prediction errors' average magnitude regardless of direction. Since it provides the precise difference between predicted and actual values, this statistic helps evaluate a model. The formula calculates the average absolute discrepancies between the predicted and actual values. The MAE formula is in Eq. (10).

$$MAE=\frac{1}{n}\sum_{i=1}^{n}\left|Y_i-\hat{Y}_i\right| \quad (10)$$

$$RMSE=\sqrt{\frac{1}{n}\sum_{i=1}^{n}\left(Y_i-\hat{Y}_i\right)^2} \quad (11)$$

where n is the quantity of occurrences.,

Y_i is the actual value at occurrences i,

$\hat{Y}_i$ is the predicted value at occurrences i

$\left|Y_i-\hat{Y}_i\right|$ reflects each occurrence's absolute error.

The Root Mean Squared Error (RMSE) statistic is often used by predictive models in order to carry out an evaluation with a degree of accuracy that they possess. We were able to calculate the difference between the numbers that were predicted and those that were actually observed by using the square root of the average of the squared deviations. This allows us to determine the difference between the two sets of numbers. RMSE is one of the measures that was used to evaluate how well the predictions made by the model fit the actual data. Due to the fact that this

measure squares differences, it provides more weight to larger errors that are the result of the squared differences approach. As a consequence of this, major deviations and outliers have the ability to have a large impact on the root mean square error (RMSE). Because it presents a degree of mistakes in the same units as the data that was initially gathered, Eq. (11) was a useful indicator for assessing the overall performance of a model. This was because it displays the errors in the same units.

4. Result and discussion

The dataset gathers PM2.5 data for the Thai province of Chiang Mai over a period of 2,218 days, spanning 60 months, from January 2018 to December 2022. The test data was obtained between January 2023 and December 2023. In addition to exterior factors like temperature, cloud cover, relative humidity, wind speed, and rainfall, it includes 52,584 records with PM2.5 values. This large dataset made it easier to accurately measure and predict PM2.5 levels while taking a variety of meteorological factors into consideration.

Table 1 2023 monthly actual data vs. numerous predicting systems.

Year 2023	Actual	ARIMA	Best SARIMA	SARIMAX (temp)
January	43.446	33.618	36.128	36.562
February	36.796	31.159	28.069	28.186
March	34.467	29.069	31.440	31.596
April	37.329	28.022	26.984	25.839
May	24.240	26.419	18.962	17.965
June	17.774	26.636	20.838	20.311
July	17.697	27.769	28.543	28.317
August	20.482	28.506	18.045	17.806
September	17.800	28.844	24.221	23.661
October	20.949	28.918	27.487	27.339
November	29.446	28.579	24.572	24.244
December	37.117	28.187	36.822	35.973

Table 2 2023 monthly actual data vs. numerous predicting systems (con.).

Year 2023	SARIMAX(Humidity)	SARIMAX (Cloud Cover)	SARIMAX (Wind Speed)	SARIMAX(Rainfall)
January	36.040	37.094	35.842	35.995
February	29.131	30.272	27.094	28.516
March	33.864	33.683	30.662	32.459
April	33.207	30.380	27.190	27.465
May	21.957	21.737	19.795	20.996
June	20.701	20.622	22.288	20.620
July	28.667	28.642	30.571	28.790
August	18.818	18.182	17.942	20.428
September	23.140	24.241	25.184	23.613
October	24.270	25.824	28.374	25.515
November	24.876	25.296	24.706	25.331
December	35.649	36.808	36.538	36.938

On the other hand, the PM2.5 levels for each month of 2023 are shown in Tables 1 and 2, and the forecasts for each model reveal the PM2.5 values in Chiang Mai Province. Please refer to both tables displayed down below. Examples of models that are provided in this package include ARIMA, the best SARIMA, and a number of other SARIMAX models. These models consider a variety of parameters, including temperature, humidity, cloud cover, wind speed, and rainfall. One example of a forecast with an actual value of 43.446, was recorded for the month of January, as shown by the data in Table 1. It is worth noting that the year 2023 saw the highest rating for PM2.5. The ARIMA model anticipated 33.618, whereas the best SARIMA model projected 36.128. Additionally, for this month, a number of models generated forecasts that were different from one another. The SARIMAX models, while factoring in a wide range of meteorological factors, generated the following predictions: 36.562 for temperature, 36.040 for humidity, 37.094 for cloud cover, 35.842 for wind speed, and 35.995 for rainfall.

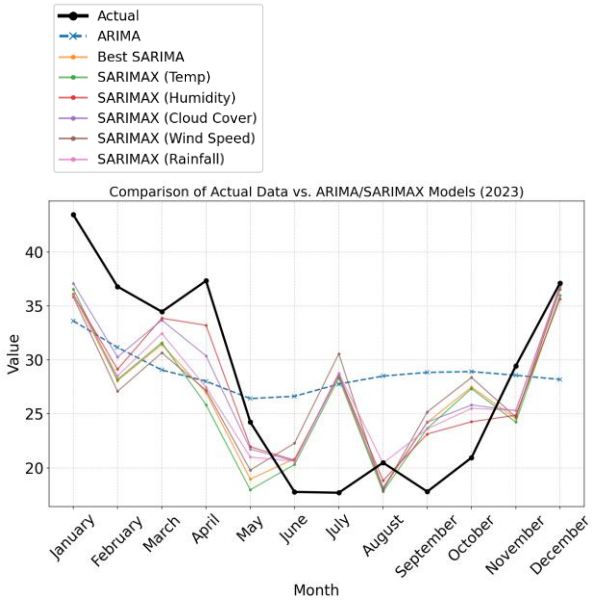

Figure 6 Many predicting methods compared to 2023 monthly data.

The graph in Figure 6 presents a comparison between the actual levels of PM2.5 in Chiang Mai for the year 2023 and the predictions generated by a number of models. These models include

ARIMA, SARIMA, and numerous SARIMAX models, all of which consider a variety of meteorological factors, such as temperature, humidity, cloud cover, wind speed, and rainfall. During the month of January, the actual PM2.5 value reached its maximum point, which was far greater than any model's projection. The SARIMAX model, which took into consideration cloud cover, produced the most accurate estimate of the data. These models have a tendency to reflect the trend of the actual values during the course of the year; nevertheless, they typically overestimate or underestimate the highs and lows that occur throughout the year. The existence of this gap draws attention to the challenges associated with accurately calculating PM2.5 levels and the influence that a wide range of environmental factors has on air quality. Table 3 and Figure 7 both show a comparison of the prediction error to the MAE and RMSE values. We can use metrics such as the RMSE and MAE to compare the forecast error. These metrics provide a numerical depiction of the prediction accuracy.

Table 3 Compare predicted error to MAE and RMSE.

Model	MAE	RMSE
1. ARIMA	7.34	7.95
2. Best SARIMA	5.76	6.54
3. SARIMAX (Cloud Cover)	4.58	5.43
4. SARIMAX (Humidity)	4.36	5.25
5. SARIMAX (Rain)	4.96	6.05
6. SARIMAX (Temperature)	5.85	6.60
7. SARIMAX (Wind Speed)	6.31	7.15

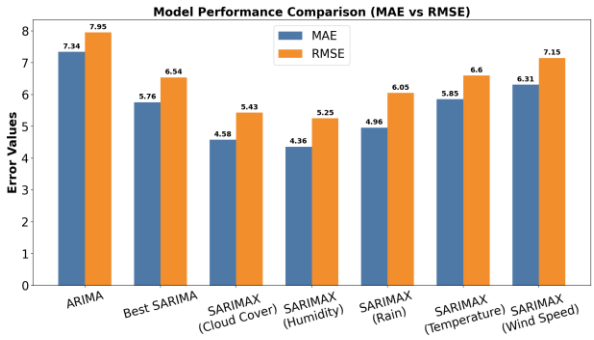

Figure 7 RMSE and MAE should be compared to prediction error.

The mean absolute error (MAE) and the root mean square error (RMSE) are two measurements that may be used in order to assess the prediction mistakes that are associated with the different models. The ARIMA model has a more significant degree of prediction error, as seen by its 7.95 RMSE and 7.34 MAE values. An RMSE of 6.54 and an MAE of 5.75 were the results of the best SARIMA model, which performed better. The SARIMAX models, which took into account a wide variety of climate-related parameters, provided a variety of results. The humidity SARIMAX model performed better than the temperature model, which has an RMSE of 6.60 and an MAE of 5.85. The humidity model has an RMSE of 5.25 and an MAE of 4.36 with a mean absolute error of 4.36. The SARIMAX cloud cover model, which has an RMSE of 5.43 and an MAE of 4.58, is shown to have better accuracy (see Figure 6), which displays the enhanced accuracy. The SARIMAX (wind speed) model, on the other hand, results in a greater number of mistakes, with an RMSE of 7.15 and an MAE of 6.31. The SARIMAX rainfall model is in the middle of the pack as it has a root mean square error of 6.05, and a mean absolute error of 4.96. When it comes to reliably estimating PM2.5 levels, the SARIMAX models which took into consideration cloud cover and humidity performed the best overall. This highlights the significance of these meteorological elements. We can direct future improvements in prediction accuracy by comparing these error measurements to acquire a better understanding of the relative advantages and downsides of each model. This has allowed us to guide future forecasting improvements.

Table 4 MAE's performance metrics.

Model	Q1 MAE	Q2 MAE	Q3 MAE	Q4 MAE
1. Best SARIMA	6.36	6.23	6.57	3.9
2. ARIMA	6.95	6.78	9.71	5.92
3. SARIMAX (Cloud Cover)	4.55	4.1	6.56	3.11
4. SARIMAX (Humidity)	5.22	3.11	5.99	3.12
5. SARIMAX (Rain)	5.91	5.32	5.65	2.95
6. SARIMAX (Temperature)	6.12	6.77	6.39	4.25
7. SARIMAX (Wind Speed)	7.03	6.37	7.6	4.24

The mean absolute error (MAE) and the root mean square error (RMSE) are two-me. The mean absolute error (MAE) and the root mean square

error (RMSE) have two measurements. RMSE and MAE performance indicators for every model in 2023 are shown in Table 4-5 and Figure 8-9. These metrics have been computed for each of the different time periods (First Quarter, Second Quarter, Third Quarter, Fourth Quarter, and Fourth Quarter). There were several metrics that were considered, and they are included in this table.

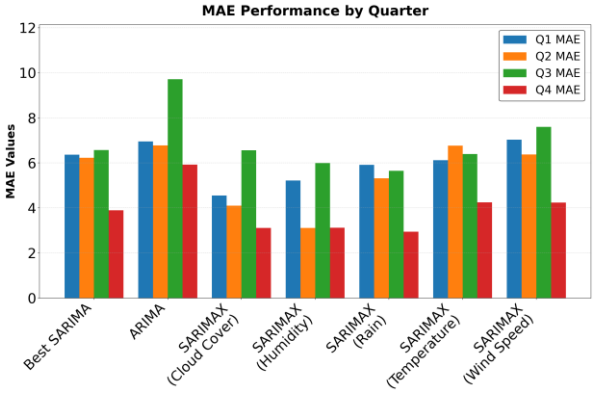

Figure 8 Time-series model performance (MAE).

Table 5 RMSE's performance metrics.

Model	Q1 RMAE	Q2 RMAE	Q3 RMAE	Q4 RMAE
1. Best SARIMA	6.8	6.93	7.41	4.71
2. ARIMA	7.25	7.53	9.79	6.93
3. SARIMAX (Cloud Cover)	5.28	4.57	7.45	3.7
4. SARIMAX (Humidity)	6.16	3.2	7.11	3.37
5. SARIMAX (Rain)	6.53	6.22	7.23	3.55
6. SARIMAX (Temperature)	6.58	7.7	7.17	4.8
7. SARIMAX (Wind Speed)	7.44	6.9	8.69	5.1

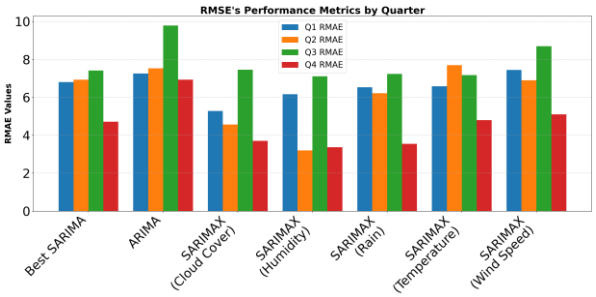

Figure 9 Time-series model performance (RMSE).

The mean absolute error (MAE) and the root mean square error (RMSE) are two-me. According to the information shown in Tables 4 and 5, overall, the SARIMAX model, which uses humidity as an exogenous variable, performs best; in most quarters, it regularly achieves the smallest MAE and RMSE values. Generally speaking, the SARIMAX models perform better than the best SARIMA models and the basic ARIMA models, which suggests that the incorporation of exogenous elements offers a significant improvement in prediction accuracy. In a rather interesting turn of events, the ARIMA model displays the largest errors, notably in Q3. The third quarter was a difficult time for all models, but the fourth quarter was a much better time, especially for the SARIMAX models which took into account the rain and humidity. When every aspect was taken into consideration, the SARIMAX (humidity) model emerges as the most trustworthy model for producing accurate predictions.

The ARIMA model was a key technique in time series forecasting those accounts for temporal correlations and variability throughout time. Its inability to take seasonality into account, particularly when forecasting PM2.5 levels that exhibit clear seasonal variations, was a significant disadvantage. Because ARIMA produced a mean absolute error (MAE) of 7.34 and a root mean squared error (RMSE) of 7.95, the model's performance at measuring clearly showed this issue. Understanding the importance of seasonality in accurately predicting PM2.5 levels, we created the SARIMA model and included a seasonal component to better represent the data's periodic oscillations. This enhancement significantly improved the accuracy of the model and led to a notable drop in both MAE and RMSE, which dropped by 17.6% (down to 6.55) and 21.5% (down to 5.76), respectively.

In order to build the SARIMAX model, we incorporated additional exogenous elements with the SARIMA model. These exogenous factors were temperature, relative humidity, cloud cover, wind speed, and rainfall. The model alone was able to account for variables that impacted PM2.5 variability beyond ARIMA and SARIMA by including these external variables. One important factor that greatly improved the model's predictive power was relative humidity. By applying these enhancements, the SARIMAX model dramatically lowered error metrics: the RMSE declined by 34% to 5.25, and the MAE decreased from the original ARIMA model by 40.6% to 4.36. These findings highlight how crucial it is to take seasonality and other exogenous variables into account when

predicting time series, especially for complex environmental data like PM2.5 levels where variations are driven by a number of interrelated causes.

5. Conclusion

Following the examination of PM2.5 data from Chiang Mai Province, the researchers used three models in order to assess the accuracy of the forecasting process. These models were ARIMA, SARIMA, and SARIMAX. We compared the MAE and RMSE values of each model and found that the SARIMAX model demonstrated the highest level of accuracy. We determined that SARIMAX, using humidity as the external variable, had the lowest MAE and RMSE values. The SARIMAX model, which used cloud cover as an external variable, demonstrated decreased MAE values in both the first quarter and the fourth quarter, as seen by a comparison of similar findings from quarter to quarter. SARIMAX was the most successful model overall because it used humidity as an external variable.

The shift from the ARIMA model to the SARIMA and SARIMAX models reveals a considerable increase in the ability to anticipate the level of PM2.5. Because it took into consideration external factors, and was able to accurately capture the complex external influences on PM2.5 levels, the SARIMAX model offers the greatest degree of projected accuracy. This research emphasizes how crucial it was to have complete models that take into account both external factors and seasonal components in order to attain high predictive accuracy in air quality forecasting.

The results of this study will be used in air quality forecasting systems, enabling the public and government agencies to prepare for PM2.5 pollution events effectively. For example, there will be notifications through mobile applications or systems for planning outdoor activities in high-risk areas. Additionally, public health authorities will be able to use the forecast data to plan the management of medical resources during PM2.5 pollution crises.

6. Acknowledgment

The authors wish to express their sincere appreciation to everyone who provided essential support and assistance for this research. We are especially grateful to Rajamangala University of Technology Lanna for their contribution. We also thank our coworkers and advisors for their invaluable guidance and feedback throughout the process, which was crucial in achieving our goals.

7. References

[1] Adiat KAN, Akeredolu BE, Akinlalu AA, Olayanju GM. Application of logistic regression analysis in prediction of groundwater vulnerability in gold mining environment: a case of Ilesa gold mining area, southwestern, Nigeria. Environ Monit Assess. 2020 Aug; 192(9).

[2] Robles-Velasco A, Cortés P, Muñuzuri J, Baets BD. Prediction of pipe failures in water supply networks for longer time periods through multi-label classification. Expert Syst Appl. 2023 Mar; 213:119050.

[3] Telikani A, Gandomi AH, Shahbahrami A. A survey of evolutionary computation for association rule mining. Inf Sci. 2020 Mar ; 524:318–52.

[4] Hickman L, Thapa S, Tay L, Cao M, Srinivasan P. Text preprocessing for text mining in organizational research: review and recommendations. Organ Res Methods. 2020 Nov ; 25(1):114–46.

[5] Cuenca E, Sallaberry A, Wang FY, Poncelet P. MultiStream: a multiresolution streamgraph approach to explore hierarchical time series. IEEE Trans Vis Comput Graph. 2018 Dec; 24(12):3160–73.

[6] Felzenszwalb PF, Huttenlocher DP. Efficient graph-based image segmentation. Int J Comput Vis. 2004 Apr; 59(2):167–81.

[7] Wang S, Cao J, Yu PS. Deep learning for spatio-temporal data mining: a survey. IEEE Trans Knowl Data Eng. 2020 Sep; 34(8):3681–700.

[8] Kong S, Ji Y, Lü B, Zhao X, Han B, Bai Z. Similarities and differences in PM2.5, PM10 and TSP chemical profiles of fugitive dust sources in a coastal oilfield city in China. Aerosol Air Qual Res. 2014 Jan; 14(7):2017–28.

[9] Chen Y, Shah N, Huggins FE, Huffman GP. Investigation of the microcharacteristics of PM2.5 in residual oil fly ash by analytical transmission electron microscopy. Environ Sci Technol. 2004 Nov; 38(24):6553–60.

[10] Singh K, Singh S, Jha AK, Aggarwal SG, Bisht DS, Murty BP, et al. Mass-size distribution of PM10 and its characterization of ionic species in fine (PM2.5) and coarse (PM10−2.5) mode, New Delhi, India. Nat Hazards. 2013 Mar; 68(2):775–89.

[11] Amnuaylojaroen T, Surapipith V, Macatangay RC. Projection of the near-future PM2.5 in Northern Peninsular Southeast Asia under RCP8.5. Atmosphere. 2022; 13(2):305.

[12] Lakshmi P, Yarlagadda S, Akkineni H, Reddy AM. Big data analytics applying the fusion approach of multicriteria decision making with deep learning algorithms. Int J Eng Trends Technol. 2021 Jan; 69(1):24–8.

[13] Yang C, Huang Q, Li Z, Liu K, Hu F. Big data and cloud computing: innovation opportunities and challenges. Int J Digit Earth. 2016 Nov; 10(1):13–53.

[14] Wang S, Cao J, Yu PS. Deep Learning for Spatio-Temporal Data Mining: A Survey. IEEE Transactions on Knowledge and Data Engineering. 2020 Sep; 34(8):3681–700.

[15] Díaz-Robles LA, Ortega JC, Fu JS, Reed GD, Chow JC, Watson JG, et al. A hybrid ARIMA and artificial neural networks model to forecast particulate matter in urban areas: the case of Temuco, Chile. Atmos Environ. 2008 Jul; 42(35):8331–40.

[16] Lee D, Lee D, Choi M, Lee J. Prediction of network throughput using ARIMA. In: 2020 International Conference on Artificial Intelligence in Information and Communication (ICAIIC); 2020; Fukuoka, Japan. IEEE; 2020. p. 1–5.

[17] Khashei M, Bijari M. A novel hybridization of artificial neural networks and ARIMA models for time series forecasting. Appl Soft Comput. 2010 Nov; 11(2):2664–75.

[18] Shivhare N, Rahul AK, Dwivedi SB, Dikshit PKS. ARIMA based daily weather forecasting tool: a case study for Varanasi. Mausam. 2021 Nov;70(1):133–40.

[19] Berkeleyearth. Org [Internet]. Independent Data for a Resilient Future, Available from: https://berkeleyearth.org/.

[20] An additional source of environmental information [Internet]. the Hydrological Information Institute, Available from: https://www.hii.or.th/.

[21] Yakubu UA, Saputra MPA. Time series model analysis using autocorrelation function (ACF) and partial autocorrelation function (PACF) for e-wallet transactions during a pandemic. Int J Glob Oper Res. 2022 Aug ;3(3):80–5.

[22] Manigandan P, Alam MS, Alharthi M, Khan U, Alagirisamy K, Pachiyappan D, et al. Forecasting natural gas production and consumption in United States—evidence from SARIMA and SARIMAX models. Energies. 2021 Sep;14(19):6021.

Machine Learning Model Development for Water Level Forecasting at P.1 Station, Chiang Mai Province

Supachai Mukdasanit [1] and Tawee Chaipimonplin [2*]
[1] Department of Business Computer, Faculty of Management Science, Chiang Mai Rajabhat University
202 Changpuek Rd., Muang, Chiang Mai, Thailand, 50300
[2] Department of Geography, Faculty of Social Sciences, Chiang Mai University
239 Huay Kaew Road, Muang, Chiang Mai, Thailand, 50200
*Corresponding Author: tawee.c@cmu.ac.th. Phone Number: +66-868799882

Received: 24 December 2024, Revised: 27 May 2025, Accepted: 5 June 2025

Abstract
This research applies machine learning models to forecast water levels at the P.1 station (Nawarat Bridge), Chiang Mai Province, both for 6 and 9 hours in advance. The objectives are to identify suitable variables and to create models for forecasting water levels at the P.1 station. The study utilizes historical hourly water level data from the P.1 and P.67 stations, combined with Moving Average (MA) and Exponential Moving Average (EMA) data covering the years from 2017 to 2024, which has amounted to a total of 66,180 records. The dataset is divided into a training set (80%) and a testing set (20%). The experiment design involves creating artificial neural network models based on historical data from one station (P.1) and two stations (P.1 and P.67). The models consist of those using only historical data, those using historical data combined with MA, and those using historical data combine with EMA, resulting in a total of 12 models. The structure of each model was optimized to achieve the best forecasting results. The results indicate that the best model for the 6-hour forecasting is the P.1_6 + P.67_6 + EMA model. This model utilizes 18 input variables, with 6 and 2 nodes in the first and second hidden layers, respectively, and 1 output node. This model achieved a Mean Absolute Error (MAE) of 0.0405, a Root Mean Square Error (RMSE) of 0.0578, and a coefficient of determination (R^2) of 0.9859. For the 9-hour forecasting, the best model is the P.1_9 + P.67_9 + EMA model, which also employs 18 input variables, with 5 and 4 nodes in the first and second hidden layers, respectively, and one output node. This model achieved a MAE of 0.0562, an RMSE of 0.0776, and an R^2 of 0.9746. Both models utilize data from two stations combined with EMA.
Keywords: Water Level Forecast, Machine Learning, Artificial Neural Network, Exponential Moving Average

1. Introduction

Flooding is considered one of the most severe natural disasters, causing significant damage to human lives, agriculture, infrastructure, and social and economic systems. Consequently, studies on flood disaster management systems and flood forecasting have gained increased importance. Accurate forecasting of flood occurrences and their progression poses a considerable challenge. Estimating water levels and flow speeds over extensive areas necessitates the integration of data, and the development of flood propagation models, which involve complex computations [1]. Water level forecasting is essential for effective water resource management and flood prevention [2]. Especially in regions like Chiang Mai, which has experienced severe flooding events, including the major flood of 2011 [3] and the 2022 flood caused by Tropical Storm "Noru". The storm led to a significant increase in the water volume of tributaries of the Ping River. The Regional Irrigation Office 1 measured and recorded the water level at the P.1 station on October 3rd, 2022, at 03:00 AM to be 4.14 meters, which was 0.44 meters above the critical water level. With continuous inflow from upstream, the water level subsequently rose up to 4.30 meters [4]. The most recent flood in the city of Chiang Mai occurred on

October 5th, 2024, when the water level of the Ping River peaked at 5.28 meters. This measurement was 1.58 meters above the riverbank level and exceeded the critical flood barrier level of 4.20 meters by 1.08 meters [5]. This situation affected key economic areas within the Chiang Mai city municipality, leading to damage to living conditions, property, businesses, and urban infrastructure. Therefore, monitoring water levels in Chiang Mai's economic zones is essential. The public can access information on water levels at the P.1 station, which is located at Nawarat Bridge, and this serves as the most important monitoring point for flood situations along the Ping River as it flows through the city of Chiang Mai. This station provides crucial indicators of flood risks that impact vital economic areas in the urban center.

Currently, the Royal Irrigation Department utilizes data from the P.67 station through a telemetry system to forecast water levels at the P.1 station. When water levels at the P.67 station reaches 4 meters, and with a flow rate of 530 cubic meters per second, it is anticipated that within 6 to 7 hours that water will overflow into urban areas, resulting in the water level at the P.1 station to overflow the riverbank. The public can monitor nearby water levels through the Chiang Mai Office of Irrigation 1's website, and the SWOC mobile application [6]. However, there is currently no advanced water level forecasting system that using machine learning models. An accurate forecasting system would significantly enhance preparedness for all stakeholders: government agencies such as the Royal Irrigation Department could issue timely flood warnings, and effectively manage reservoirs and drainage systems. Chiang Mai Municipality could also prepare pumps and flood prevention equipment in advance; Disaster response units could plan evacuations proactively; businesses would have the opportunity to safeguard their assets and inventory; hotels and tourist attractions could warn visitors and prepare appropriate responses; industrial sectors could adjust production and logistics accordingly; and residents could evacuate, move valuables to safety, stockpile essential supplies, and plan alternative routes in anticipation of flooded roads.

Presently, machine learning models play a critical role in the developing of forecasting models, particularly in the field of hydrology [7]. This study involved the collection of historical water level data from the P.1 and P.67 stations. The water levels at P.1 station exhibit a strong correlation with those at P.67 [8], as P.67 station is situated on the main river and serves as the upstream station for P.1 station, as illustrated in Figure 1.

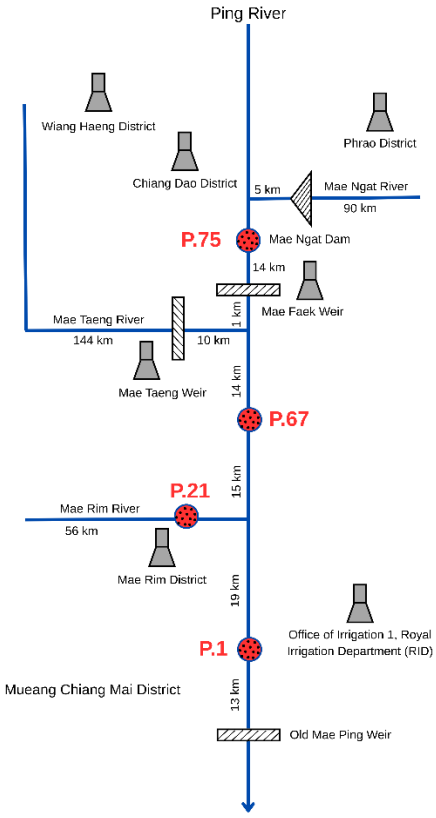

Figure 1. Hydrological diagram of the Ping River Basin [9]

Due to the geographical relationship between the two stations, the water level at the P.67 station significantly impacts the water level at the P.1 station. Consequently, data from the P.67 station is a critical variable for forecasting the water levels at the P.1 station [8]. The utilization of upstream data enhances the efficiency of forecasting models while reducing potential errors associated with relying solely on data from a single station. Therefore, data from the P.1 and P.67 stations are employed to develop an hourly water level

forecasting model specifically for P.1 station, which provides forecasts at 6-hour and 9-hour intervals. The 6-hour forecast is designed to enable relevant agencies to prepare for and respond promptly to flooding events, while the 9-hour forecast serves as a mid-range projection to assist in flood disaster planning and efficient water resource management.

Additionally, time series analysis techniques were employed, specifically the Simple Moving Average (MA) and Exponential Moving Average (EMA) methods to reduce data volatility and filter out unwanted noise [10]. The MA method computes a simple average, whereas the EMA method assigns greater weight to more recent data, thereby making the forecasts more responsive to changes [11]. The MA and EMA techniques have been shown to enhance the predictive accuracy of machine learning models, as demonstrated in [12] and [13]. Furthermore, the Stepwise Regression method was employed to identify the most appropriate variables for the development of the forecasting model. This method is efficient in filtering independent variables from large datasets by considering those with the highest correlation to the outcome, and systematically adding or removing variables to determine the optimal set. This improves forecast accuracy and reduces model complexity, enabling faster and more efficient computation [14].

This research aims to develop a machine learning-based model to forecast water levels 6 and 9 hours in advance, leveraging data from MA and EMA of water levels at the P.1 and P.67 stations, along with the most up-to-date data for model creation and testing. While previous forecasting models at station P.1 employed the Moving Average (MA) approach to improve prediction accuracy [15], [16], the limitations of this method became evident during the 2024 flood event, when water levels fluctuated rapidly. To address this, this study proposes integrating EMA into the forecasting process, hypothesizing that EMA's ability to respond more effectively to rapid changes will enhance predictive accuracy. The results of this study will support the development of flood warning systems and water management strategies in the upper Ping River basin, enabling timely and effective decision-making. Additionally, the model will aid businesses in risk management, reducing asset losses, and improving operational efficiency and sustainability, particularly in transportation, goods handling, and production planning.

This research aims to study the following objectives:

To identify the appropriate variables for forecasting the water level at Station P.1 (Nawarat Bridge), Chiang Mai Province, using historical water level data from Station P.1 and P.67, as well as MA and EMA values.

To develop an artificial intelligence model for forecasting the water level at Station P.1 for 6-hour and 9-hour ahead predictions, comparing the accuracy of the model using data from a single station with the model using data from two stations, and considering the effect of using MA and EMA to enhance the model's performance.

2. Literature Review

2.1. Moving Average Techniques (MA and EMA)

Time Series Analysis is an essential tool in finance, economics, and engineering for understanding data that changes over time. Among the various techniques used, Moving Average is widely adopted to smooth out data fluctuations, making underlying trends more visible [10].

- Simple Moving Average (MA) calculates the average of data over a specific period by assigning equal weights to all data points. While simple to use and interpret, MA tends to respond slowly to data changes as it gives equal importance to all data, regardless of recency [17].
- Exponential Moving Average (EMA) assigns greater weight to more recent observations, allowing it to respond more quickly to new trends. This makes EMA particularly useful for rapidly changing data [11] such as stock prices or water levels during storms.

2.2. Application of MA and EMA in Neural Network Models

MA and EMA have been applied to enhance the performance of ANN, particularly during the preprocessing phase of time-series modeling.

- A 5-day MA combined with ANN and Particle Swarm Optimization (PSO) was implemented for stock price forecasting. The use of MA as a preprocessing technique significantly improved model accuracy [12].
- EMA was combined with Neural Networks to forecast wireless channel quality based on the Frame Delivery Ratio. The EMA-enhanced model reduced Mean Squared Error (MSE) by 20-30%, particularly in scenarios involving sudden and nonlinear signal variations [13].

2.3. Forecasting Models

- Streamflow forecasting at the Huanren station in China was investigated using both individual models-Long Short-Term Memory (LSTM), Support Vector Machine (SVM), Random Forest (RF), and Artificial Neural Network (ANN)-and hybrid models incorporating signal decomposition techniques such as Empirical Mode Decomposition-LSTM (EMD-LSTM), Variational Mode Decomposition-LSTM (VMD-LSTM), and Wavelet Analysis-LSTM (WA-LSTM). LSTM showed the highest accuracy among single models, particularly during high-flow days, while VMD-LSTM outperformed other hybrid models in all performance metrics, achieving the lowest RMSE (52.14 m^3/s), the highest NSE (0.96), and the lowest BIAS (-0.002) during testing [18].

The study highlighted that signal decomposition (e.g., VMD) can effectively remove noise and isolate critical frequency components, thereby enhancing model performance significantly. Table 1 represents the strengths and limitations of the models.

Table 1 Comparison of Models

Model	Strengths	Limitations
LSTM	Excellent for time series, high accuracy, retains long-term dependencies	Complex structure, long training time
SVM	Suitable for linear/separable data, good with balanced datasets	Poor for large or nonlinear datasets, requires kernel selection
RF	Robust to noise/outliers, user-friendly, avoids overfitting	Lower accuracy in sequential data
ANN	Flexible architecture, broadly applicable, low overall bias	Sometimes less accurate for time series compared to LSTM

2.4. Water Level Forecasting at P.1 Station, Chiang Mai

Artificial Neural Networks (ANNs) were applied to forecast water levels at the P.1 station in northern Thailand using historical hourly water levels from stations P.1, P.67, and P.75, along with dam discharge data and corresponding MA values [15]. A comparison of learning algorithms-Levenberg-Marquardt (LM) and Bayesian Regularization (BR)-revealed that the LM algorithm with 75% hidden nodes provided the best performance for both 6- and 12-hour ahead forecasts.

A subsequent study compared ten ANN training algorithms, including LM, BR, Gradient Descent with Momentum and Adaptive Learning Rate (GDX), Resilient Backpropagation (RP), Broyden-Fletcher-Goldfarb–Shanno (BFG), and Scaled Conjugate Gradient (SCG) [16]. LM consistently delivered the highest accuracy for short-term forecasting (t+6 hours), followed by BR. The number of hidden nodes had minimal impact on performance, except for longer forecast horizons (t+18 hours).

2.5. Research Gap

To date, there has been no study that utilizes historical water level data from only two stations (P.1 and P.67) in combination with EMA-transformed data for short-term forecasting at station P.1. This study addresses this gap by minimizing the number of input sources while leveraging EMA to enhance the performance of an ANN. Focusing on a smaller number of well-processed inputs helps mitigate the risks associated with missing or erroneous data, thereby improving the reliability of the model. The EMA's responsiveness to short-term signal changes makes it a suitable choice for increasing model accuracy in such contexts.

This study differs from previous works [15], [16] in that it employs input data from only two stations (P.1 and P.67) and applies EMA for forecasting enhancement, whereas those studies used data from three stations-P.1, P.67, and P.75-as well as dam discharge volumes and MA of dam discharge.

3. Materials and Methods

3.1. Research Data

The hourly water level data from the P.1 and P.67 stations, collected from April 2017 to October 2024, comprise a total of 66,180 data points (Figure 2). These timeframes were selected for their completeness and reliability, characterized by nearly complete data coverage with only minimal data loss. This selection was made to minimize potential errors in calculating the MA and EMA values. Secondary data used for research purposes were collected by the Upper Northern Hydrology Center of the Royal Irrigation Department (Irrigation Office 1, Chiang Mai) [6]. Notable flooding events occurred from October 2nd to 5th, 2022, September 24th to 28th, 2024, and from October 3rd to 7th, 2024.

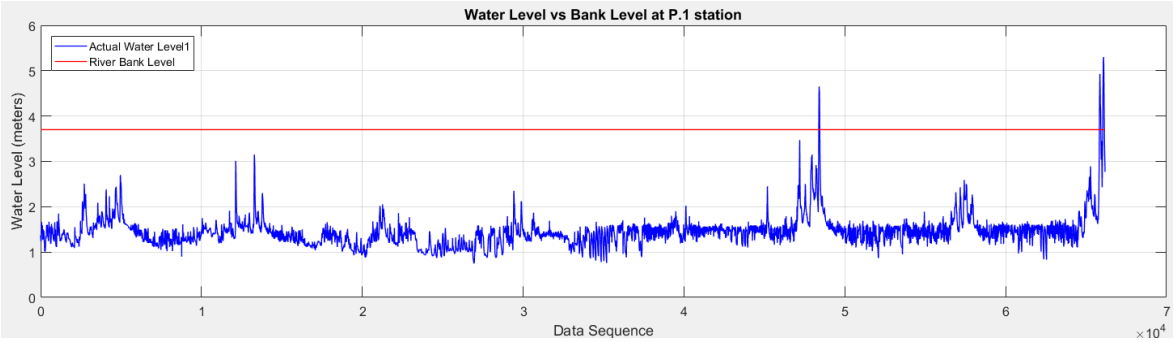

Figure 2. Hydrograph of data from April 2017 to October 2024

3.2. Research Tools

The tools used in this research include:

1) Microsoft Excel for data collection and preparation.

2) MATLAB for processing artificial neural network models.

3) SPSS for variable selection using Stepwise regression

3.3. Data Preparation

1) The water level data from the P.1 and P.67 stations were stored for the past 0 to 24 hours with variable names P1t-0 to P1t-24 and P67t-0 to P67t-24 in decimal format with two decimal places.

2) The Moving Average (MA) is a statistical method used to calculate the average water level over a specific period. This technique facilitates the identification of water level trends by smoothing out short-term fluctuations and reducing data variability. The MA method is also commonly applied in various fields, particularly in financial markets such as stocks, cryptocurrencies. MA water level data for the P.1 and P.67 stations were prepared for the past 0 to 24 hours, with each time point (t) representing the calculation of the hourly moving average of water levels over a period of *k* hours, where *k* ranges from 2 to 24. The formula for calculating the MA water level data [19] is as follows.

$$MA_{t,k}=\left(P_t+P_{t-1}+\ldots+P_{t-(k-1)}\right)/k \quad (1)$$

3) The Exponential Moving Average (EMA) is a technical analysis tool similar to the MA and is widely used in financial markets such as stocks and cryptocurrencies. While it shares similarities with the MA, a key distinction is that the EMA assigns greater weight to more recent data, allowing it to respond more quickly to changes in the dataset. Therefore, in this study, the EMA is utilized alongside historical water level data to forecast future water levels. Furthermore, the study compares the forecasting performance between using only historical water level data and using historical data in conjunction with the MA. EMA water level data for the P.1 and P.67 stations were prepared for the past 0 to 24 hours, with each time point representing the calculation of the hourly EMA of water levels over a period ranging

from 2 to 24 hours. The formula for calculating the EMA water level data [20] is as follows.

$$EMA_t = \left(P_t \times \frac{2}{n+1}\right) + EMA_{t-1}\left(1 - \frac{2}{n+1}\right) \quad (2)$$

3.4. Variable selection

Variable selection was performed using Stepwise Regression [21] to create a total of 12 forecasting models from the prepared dataset.

3.5. Model Development

The machine learning models in this study were developed using an Artificial Neural Network (ANN) with a Feed-Forward Back Propagation (FFBP) technique [22]. The Feedforward Neural Network (FFNN) is a type of ANN in which data flows in one direction, from the input layer to the output layer. The input layer receives external data, with the number of neurons determined by the number of features or variables relevant to the learning and forecasting tasks. The hidden layers process the input data through the application of activation functions, such as sigmoid, tanh, and ReLU. The configuration of these layers, including the number of neurons in each, must be appropriately selected based on the specific problem under investigation. The hidden layers enable the network to model complex, nonlinear relationships, which is particularly important for tasks such as water level forecasting. The output layer provides the final prediction, with a single neuron representing the forecasted water level in this study. The training process employs the backpropagation technique, which adjusts the weights and biases within the network to minimize the discrepancy between the predicted outputs and the actual target values, ensuring optimal accuracy in the final results.

Each model in this study was constructed using the "newff" package. The parameters of each model were set as follows [15], [16], [23].

- Learning function: trainlm
- Hidden layer activation function: tanh
- Output layer activation function: purelin
- Maximum epochs: 1,000
- Learning goal (target): 1e-5

To obtain the most suitable model for each dataset, the number of nodes in the input layer for each model was determined based on the number of features, which were selected through the Stepwise Regression process. The number of hidden layers was limited to a maximum of two to prevent excessive consumption of computational resources, while still maintaining a sufficiently high level of forecasting performance. For determining the number of nodes in each hidden layer, a trial-and-error method was employed [15], [16]. The first hidden layer was assigned a range of 1 to 20 neurons, while the second hidden layer was set to none, with the number of neurons also ranging from 1 to 20, to find the most appropriate network structure.

Each dataset is divided into 80% for training and 20% for testing [24], using a chronological split method that preserves the natural time order from April 2017 to October 2024. The goal is to identify the most efficient model for forecasting 6 and 9 hours ahead. The models evaluated for performance comparison are as follows:

3.5.1 Six-Hour Ahead Water Level Forecasting Models for the P.1 station

- Data from P.1 (P.1_6)
- Data from P.1 and MA (P.1_6 + MA)
- Data from P.1 and EMA (P.1_6 + EMA)
- Data from P.1 and P.67 (P.1_6 + P.67_6)
- Data from P.1, P.67, and MA for both stations (P.1_6 + P.67_6 + MA)
- Data from P.1, P.67, and EMA for both stations (P.1_6 + P.67_6 + EMA)

3.5.2 Nine-Hour Ahead Water Level Forecasting Models for the P.1 station

- Data from P.1 (P.1_9)
- Data from P.1 and MA (P.1_9 + MA)
- Data from P.1 and EMA (P.1_9 + EMA)
- Data from P.1 and P.67 (P.1_9 + P.67_9)
- Data from P.1, P.67, and MA for both stations (P.1_9 + P.67_9 + MA)
- Data from P.1, P.67, and EMA for both stations (P.1_9 + P.67_9 + EMA)

3.6. Model Evaluation

The performance of the models was evaluated based on the following metrics

- Mean Absolute Error (MAE)

It is an indicator used to calculate the Mean Absolute Error (MAE) of forecast values

compared to actual values [25], computed using the formula.

$$MAE=\frac{1}{n}\sum_{i=1}^{n}|y_i-\hat{y}_i| \quad (3)$$

-Root Mean Square Error (RMSE)

It is a metric used to measure the deviation between predicted and actual values, giving more weight to larger errors by squaring the deviations before averaging and then taking the square root [25].

$$RMSE=\sqrt{\frac{1}{n}\sum_{i=1}^{n}(y_i-\hat{y}_i)^2} \quad (4)$$

-R-squared (R^2)

It is a metric used to measure how well the predicted data explains the variance of the actual values [26]. It ranges between 0 and 1 and is calculated using the formula.

$$R^2=1-\frac{\sum(y_i-\hat{y}_i)^2}{\sum(y_i-\bar{y})^2} \quad (5)$$

The MAE and RMSE values should be as low as possible, while the R^2 value should be as high as possible (close to 1) to indicate that the model can explain the variability in the data effectively [27].

4. Results and Discussion

4.1. Results of Variable Selection Using Stepwise Regression

Variable selection for model development was conducted using Stepwise Regression, starting with no independent variables and progressively adding them one at a time based on their significance in explaining the dependent variable, according to predefined criteria. The results of the variable selection for each forecasting model are as follows: Model P.1_6 included 7 variables; Model P.1_6 + MA included 10 variables; Model P.1_6 + EMA included 8 variables; Model P.1_6 + P.67_6 included 16 variables; Model P.1_6 + P.67_6 + MA included 19 variables; Model P.1_6 + P.67_6 + EMA included 18 variables; Model P.1_9 included 7 variables; Model P.1_9 + MA included 8 variables; Model P.1_9 + EMA included 9 variables; Model P.1_9 + P.67_9 included 17 variables; Model P.1_9 + P.67_9 + MA included 18 variables; and Model P.1_9 + P.67_9 + EMA included 18 variables. The selected variables for each model are summarized in Table 2.

Table 2 Results of Variable Selection for Forecasting Models Using Stepwise Regression

Model	Variable Selection		
P.1_6	P1t-0	P1t-1	P1t-2
	P1t-3	P1t-12	P1t-19
	P1t-24		
P.1_6 + MA	P1t-0	P1t-1	P1t-3
	P1t-12	P1t-0_MA2	P1t-0_MA18
	P1t-18_MA24	P1t-23_MA11	P1t-24_MA3
	P1t-24_MA24		
P.1_6 + EMA	P1t-0	P1t-0_EMA2	P1t-0_EMA4
	P1t-1_EMA2	P1t-1_EMA3	P1t-12EMA24
	P1t-14_EMA20	P1t-20_EMA3	
P.1_6 + P.67_6	P1t-0	P1t-1 P1t-2	P67t-24
	P1t-3	P1t-12	P1t-19
	P1t-24	P67t-0	P67t-1
	P67t-5	P67t-6	P67t-7
	P67t-8	P67t-9	P67t-12
P.1_6 + P. 67_6 + MA	P1t-0	P1t-1_MA2	P1t-2
	P1t-3	P1t-12_MA3	P1t-13_MA22
	P1t-18_MA2	P1t-20_MA2	P1t-24_MA20
	P1t-24_MA24	P67t-0	P67t-0_MA2
	P67t-0_MA9	P67t-1_MA16	P67t-5_MA2
	P67t-7_MA2	P67t-18_MA22	P67t-24_MA5
	P67t-24_MA24		
P.1_6 + P. 67_6 + EMA	P1t-0	P1t-0_EMA23	P1t-1_EMA2
	P1t-4	P1t-2	P1t-10_EMA5
	P1t-19	P1t-20_EMA9	P1t-24_EMA3
	P1t-24_EMA24	P67t-0_EMA2	P67t-0_EMA5
	P67t-6	P67t-7_EMA6	P67t-20_EMA18
	P67t-23_EMA24	P67t-24_EMA3	P67t-24_EMA20
P.1_9	P1t-0	P1t-1	P1t-2
	P1t-3 P1t-24	P1t-12	P1t-17
P.1_9 + MA	P1t-0	P1t-1	P1t-1_MA2
	P1t-3	P1t-10_MA3	P1t-13_MA24
	P1t-21_MA11	P1t-24_MA2	
P.1_9 + EMA	P1t-0	P1t-1_EMA2	P1t-2
	P1t-4_EMA2	P1t-12_EMA24	P1t-14_EMA18
	P1t-14_EMA21	P1t-18_EMA9	P1t-24_EMA2
P.1_9 + P.67_9	P1t-0	P1t-1	P1t-2
	P1t-3	P1t-12	P1t-16
	P67t-0	P67t-1	P67t-3
	P67t-4	P67t-5	P67t-6
	P67t-7	P67t-8	P67t-9
	P67t-11	P67t-24	
P.1_9 + P. 67_9 + MA	P1t-0	P1t-0_MA2	P1t-0_MA20
	P1t-1_MA2	P1t-2	P1t-7_MA2
	P1t-11_MA6	P1t-17_MA3	P1t-24_MA7
	P1t-24_MA24	P67t-0	P67t-3_MA2
	P67t-3_MA10	P67t-5_MA2	P67t-7_MA2
	P67t-24_MA3	P67t-24_MA13	P67t-24_MA24
P.1_9 + P. 67_9 + EMA	P1t-0	P1t-1_EMA2	P1t-2_EMA14
	P1t-5	P1t-9	P1t-13_EMA_3
	P1t-17	P1t-21_EMA_12	P1t-23_EMA_5
	P67t-0	P67t-1	P67t-3
	P67t-4_EMA_8	P67t-8_EMA_2	P67t-17_EMA_3
	P67t-21	P67t-24_EMA_21	P67t-24_EMA_24

The meanings of the variables listed in Table 2 are further explained in Table 3, which provides descriptions of each variable used in the study.

Table 3 Definitions of the variables.

Variable Type	Description
Pnt-k	Water level at station *Pn* at *t-k* hours prior to the current time, where *Pn* represents the station code (i.e., P1 or P67), and *t-k* indicates the time lag of *k* hours from the present.
Pnt-k_MAp	Moving Average (MA) of the water level at station *Pn*, calculated from time *t-k* to *t-k-(p-1)*, totaling *p* values.
Pnt-k_EMAq	Exponential Moving Average (EMA) of the water level at station *Pn*, starting from time *t-k* and using *q* past values (or *q* periods).

4.2. Results of Water Level Forecasting Models for Station P.1

The Feed-Forward Back Propagation (FFBP) artificial neural network was used to develop forecasting models for the water level at the P.1 stations, both for 6-hour and 9-hour forecasts, using data from either one station (P.1) or two stations (P.1 and P.67). The models varied in terms of the number of nodes in the input layer, the number of hidden layers, the number of nodes in the hidden layers, and the number of nodes in the output layer, as shown in Table 4.

Table 4 Structures of Forecasting Models for Station P.1

Model	**Input layer**	**Hidden layer**		**Output layer**
		1	**2**	
P.1_6	7	7	-	1
P.1_6 + MA	10	6	4	1
P.1_6 + EMA	8	6	3	1
P.1_9	7	6	-	1
P.1_9 + MA	8	6	2	1
P.1_9 + EMA	9	6	2	1
P.1_6 + P.67_6	17	7	-	1
P.1_6 + P.67_6 + MA	19	6	-	1
P. 1_6 + P. 67_6 + EMA	18	6	2	1
P.1_9 + P.67_9	17	6	2	1
P.1_9 + P.67_9 + MA	19	6	1	1
P.1_9 + P.67_9 + EMA	18	5	4	1

4.3. Results of the 6-Hour Water Level Forecasting Models for Station P.1

Upon analyzing the hydrograph lines for the 6-hour forecast, as illustrated in Figures 3-5 (where the green line represents the model utilizing data from two stations, and the red line represents the model utilizing data from one station), it was determined that the model using data from two stations provided better forecast results. A comparison of the use of water level data with MA and EMA data revealed that the model employing water level data combined with MA could forecast higher peak water levels than the model using water level data alone (Figure 4, green line). However, when water level data was combined with EMA, the model's ability to forecast peak water levels improved (Figure 5, green line). Additionally, for the model using data from only one station, adding EMA data enhanced the model's performance (Figure 5, red line). Therefore, based on the hydrograph analysis, the model that combined water level data with EMA from two stations (P.1_6 + P.67_6 + EMA) was selected as the best model. This conclusion is consistent with the statistical comparison results shown in Table 5.

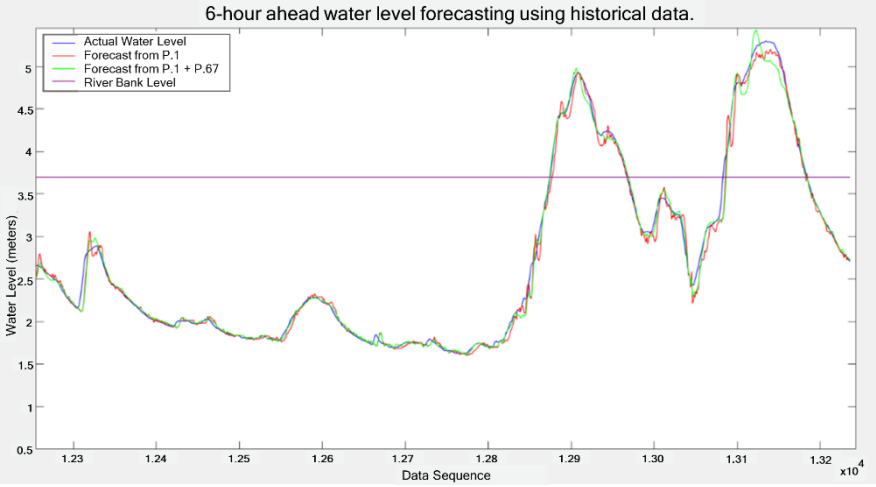

Figure 3 Comparison of the forecasting results between the P.1_6 model and the P.1_6 + P.67_6 model

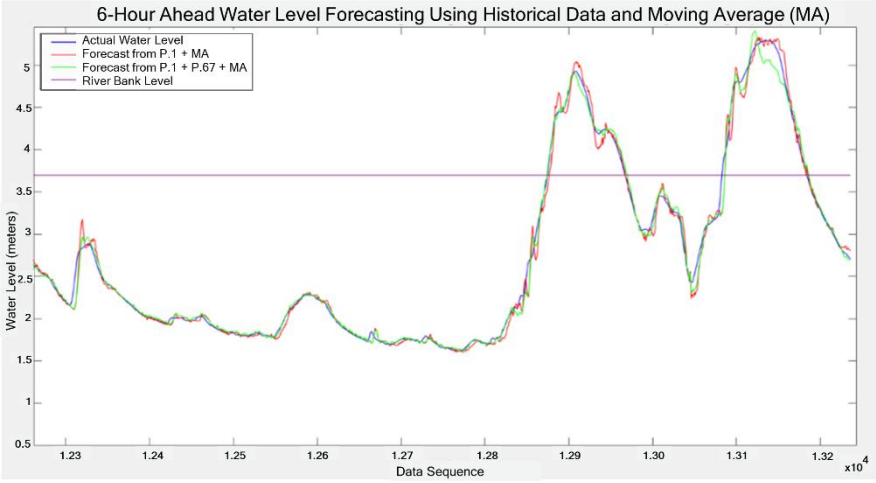

Figure 4 Comparison of the forecasting results between the P.1_6 + MA model and the P.1_6 + P.67_6 + MA model

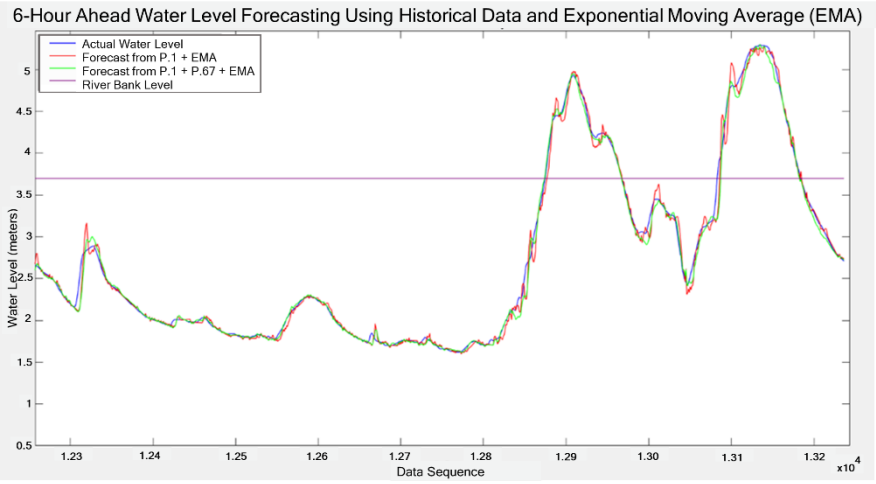

Figure 5 Comparison of the forecasting results between the P.1_6 + EMA model and the P.1_6 + P.67_6 + EMA model

4.4. Results of the 9-Hour Water Level Forecasting Model for Station P.1

The forecasting results for the 9-hour water level forecasting at the P.1 station are presented in Figure 6, where the red line represents data from one station and the green line represents data from two stations. It was observed that using data from one station provided better forecasts, particularly for predicting the peak water levels, compared to using data from two stations. However, when actual data was combined with MA and EMA data (Figures 7 and 8, respectively), it was found that the models using data from both one station and two stations showed improved performance, especially the models that used data from two stations (Figures 7-8). Adding EMA data to the two-station model continued to yield the best overall results (Figure 8), which is consistent with the statistical comparison results presented in Table 6.

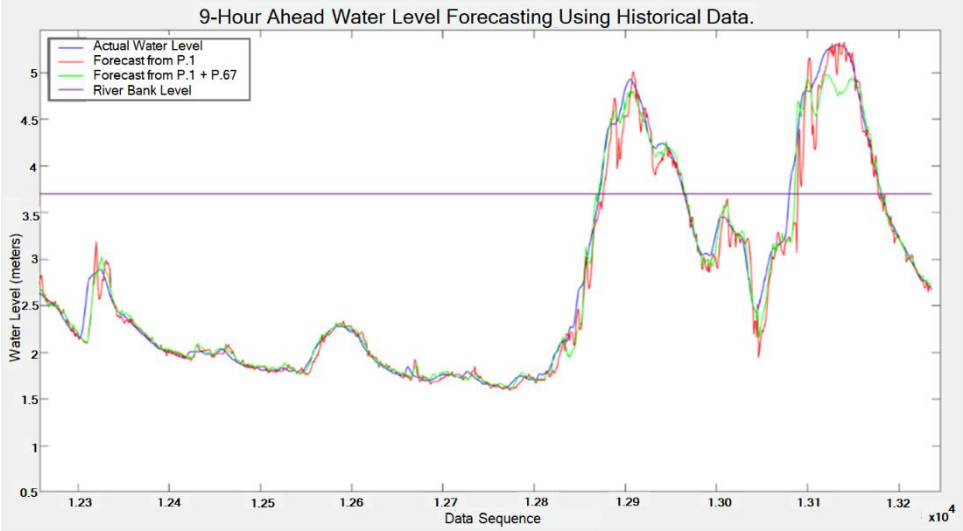

Figure 6 Comparison of the forecasting results between the P.1_9 model and the P.1_9 + P.67_9 model

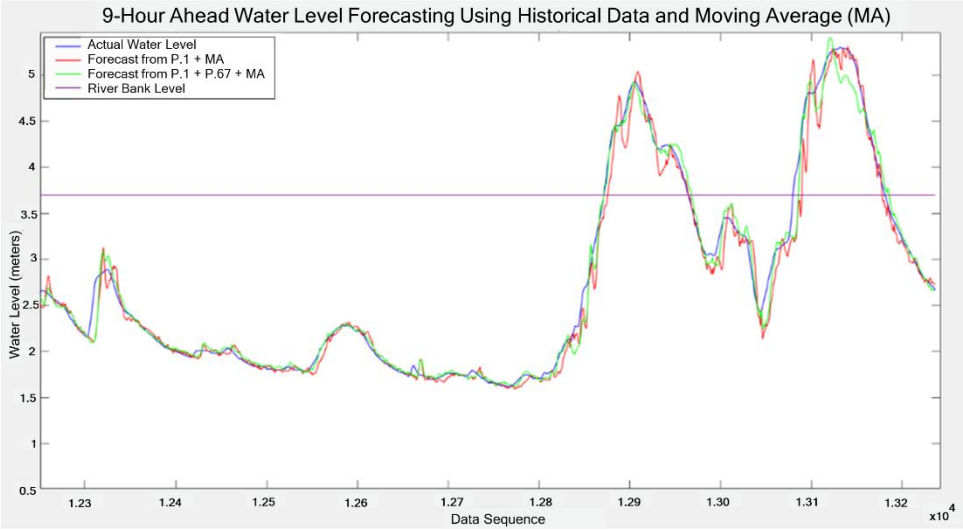

Figure 7 Comparison of the forecasting results between the P.1_9 + MA model and the P.1_9 + P.67_9 + MA model

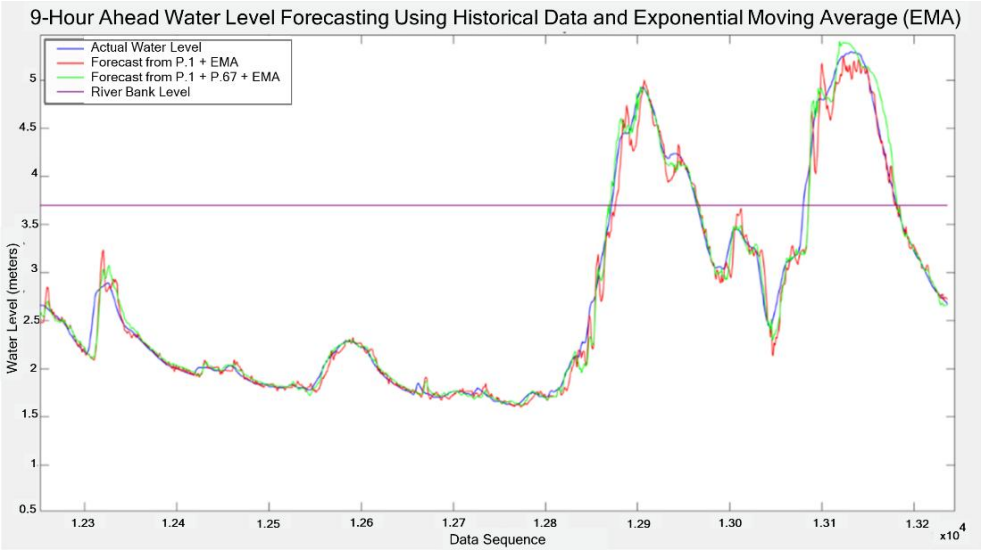

Figure 8 Comparison of the forecasting results between the P.1_9 + EMA model and the P.1_9 + P.67_9 + EMA model

4.5. Comparison of the Performance of the 6-Hour Water Level Forecasting Model for Station P.1

The results of comparing the 6- hour water level forecasting models for the P.1 station showed that the model P. 1_6 + EMA performed the best for the single station (P.1), as it yielded the lowest MAE, RMSE, and the highest R^2. This was followed by the P. 1_6 + MA model, and then the P.1_6 model. For the two-stations model (P.1 and P. 67), the P. 1_6 + P. 67_6 + EMA model showed the best performance, with the lowest MAE, RMSE, and the highest R^2, followed by the P. 1_6 + P. 67_6 + MA model and the P. 1_6 + P. 67_6 model, respectively. Additionally, the models using data from two stations outperformed those using data from only one station. Therefore, the P. 1_6 + P. 67_6 + EMA model is considered the most suitable for forecasting the 6-hour water level at Station P.1, as shown in Table 5.

Table 5 MAE, RMSE, and R^2 values for the 6-hour water level forecasting model for Station P.1

Model	Performance		
	MAE	RMSE	R^2
P.1_6	0.0470	0.0679	0.9805
P.1_6 + MA	0.0461	0.0675	0.9808
P.1_6 + EMA	0.0447	0.0655	0.9818
P.1_6 + P.67_6	0.0412	0.0587	0.9854
P.1_6 + P.67_6 + MA	0.0410	0.0582	0.9857
P.1_6 + P.67_6 + EMA	0.0405	0.0578	0.9859

4.6. Comparison of the Performance of the 9-hour Water Level Forecasting Model for Station P.1

The comparison of the 9- hour water level forecasting models for the P. 1 station, using data from only P. 1 station, revealed that the model P. 1_9 + EMA performed the best performance, with the lowest MAE, RMSE, and the highest R^2, followed by the P. 1_9 + MA model, and then the P. 1_9 model, respectively. For models using data from the P.1 and P.67 stations, the P.1_9 + P.67_9 + EMA model provided the best results, followed by the P. 1_9 + P. 67_9 + MA model, and then the P.1_9 + P.67_9 model. Additionally, the group of models using data from two stations performed better than those using data from only one station. Therefore, the P. 1_9 + P. 67_9 + EMA model demonstrated the best performance and is the most suitable for forecasting the 9- hour water levels at Station P.1, as shown in Table 6.

Table 6 MAE, RMSE, and R^2 values for the 9-hour water level forecasting model for Station P.1

Model	Performance		
	MAE	RMSE	R^2
P.1_9	0.0649	0.0939	0.9628
P.1_9 + MA	0.0657	0.0933	0.9456

P.1_9 + EMA	0.0643	0.0908	0.9652
P.1_9 + P.67_9	0.0572	0.0798	0.9732
P.1_9 + P.67_9 + MA	0.0568	0.0779	0.9744
P.1_9 + P.67_9 + EMA	0.0562	0.0776	0.9746

5. Conclusions

This study investigates the development of machine learning models for forecasting the water levels 6-hour and 9-hour ahead at the P.1 station. The primary objectives were to identify appropriate variables for forecasting water levels at the P.1 station, and to create the most suitable machine learning models for forecasting water levels at the same station for 6-hour and 9-hour periods. The results are summarized as follows:

Using data from the P.1 and P.67 stations showed better accuracy forecasting for both the 6-hour and 9-hour forecasts compared to using data from the P.1 station alone. Additionally, the inclusion of supplementary variables using EMA and MA techniques improved forecasting performance when compared to using only past water level data. Among these, EMA provided better improvement in model performance than MA.

For model development, the study used a Feed-Forward Back Propagation (FFBP) Artificial Neural Network (ANN) based on data from either one station (P.1) or two stations (P.1 and P.67). EMA and MA techniques were used to compare model performance, and variable selection was performed using Stepwise Regression.

For the 6-hour water level forecasting, the P.1_6 + P.67_6 + EMA model demonstrated the best performance, with the model structure comprising 18 input nodes; 6 and 2 nodes in the two hidden layers, and 1 output node. The model used 18 variables, including data from P.1 (P1t-0, P1t-2, P1t-4, P1t-19), EMA variables for P.1 (P1t-0_EMA23, P1t-1_EMA2, P1t-10_EMA5, etc.), data from P.67 (P67t-6, P67t-20), and EMA variables from P.67. This model achieved MAE = 0.0280, RMSE = 0.0431, and R^2 = 0.9780 for the training dataset, and MAE = 0.0405, RMSE = 0.0578, and R^2 = 0.9859 for the testing dataset. These are the best values among the models for 6-hour forecasting.

For the 9-hour water level forecasting, the P.1_9 + P.67_9 + EMA model achieved the best performance, with the model structure consisting of 18 input nodes, 4 nodes in each of the two hidden layers, and 1 output node. The model used 18 variables, including data from P.1 (P1t-0, P1t-5, P1t-9, P1t-17), EMA variables for P.1 (P1t-1_EMA2, P1t-2_EMA14, etc.), data from P.67 (P67t-0, P67t-1, P67t-3, P67t-21), and EMA variables for P.67. This model produced MAE = 0.0387, RMSE = 0.0564, and R^2 = 0.9627 for the training dataset, and MAE = 0.0562, RMSE = 0.0776, and R^2 = 0.9746 for the testing dataset. These were the best values for the 9-hour forecasting models.

In conclusion, the models for forecasting 6-hour and 9-hour water levels using past data from two stations combined with EMA performed better overall than those using past data from a single station alone or in combination with MA. Additionally, the 6-hour forecast models showed higher accuracy than the 9-hour forecast models.

For forecasting water levels at station P.1 six hours in advance, the best-performing model presented in this research utilized hourly historical water level data from two stations, P.1 and P.67, combined with the EMA of the historical water level data from both stations. This model produced forecasts consistent with the model proposed in [16], which used hourly historical data from stations P.1, P.67, P.75, and the water discharge volume from a dam, along with the MA of the dam's discharge volume. That model achieved an RMSE of less than 0.1 for 6-hour-ahead forecasting. In contrast, the study in [16] did not include a 9-hour-ahead forecast. However, the model proposed in this study still achieved an RMSE of less than 0.1 even at the 9-hour forecast horizon.

The reason why using data from two stations yields better results than using data from only one station is due to the direct correlation between P.1 and the upstream station P.67, which is located approximately 32 kilometers away. The water mass takes about 6–7 hours to travel from P.67 to P.1 [28]. Therefore, incorporating historical hourly water level data from both stations for forecasting water levels at P.1 6–9 hours in advance is likely

to result in more accurate predictions compared to using data from only P.1.

In addition, using historical hourly water level data from P.1 and P.67 along with the EMA of the historical data from both stations provided better performance than using MA or raw historical data alone. This is because EMA is more responsive to short- and medium-term changes in data [11], making it suitable for trend analysis in such timeframes. EMA assigns greater weight to the most recent data and gradually reduces the weight for older data, whereas MA gives equal weight to all data points (refer to Equations 1 and 2). On the other hand, using only the historical hourly water level data from P.1 and P.67 without any smoothing technique yielded the lowest performance, as the burden of learning trends fell solely on the Artificial Neural Network (ANN). Improving the model's performance in such cases would depend heavily on adjusting the architecture and hyper parameters. Therefore, the most appropriate model for forecasting 6- and 9-hour-ahead water levels at station P.1 is the one that uses historical hourly water level data from both P.1 and P.67 combined with the EMA of historical water level data from both stations—an approach not previously reported for model development at station P.1.

Practical Applications

The forecasting model for water levels at station P.1 proposed in this study can be effectively applied to flood warning systems in the urban area of Chiang Mai Province. One of its key advantages is the simplicity of the artificial neural network (ANN) architecture, which consists of only an input layer, a hidden layer, and an output layer. This streamlined structure enables faster processing compared to models with more complex architectures, facilitating easier development into practical applications.

Furthermore, using data from only two stations helps mitigate issues related to data loss, which often arise when relying on multiple data sources and can hinder model performance. The developed model can also be integrated to enhance previously developed flood warning applications [29], improving both forecasting accuracy and the overall efficiency of the warning system.

The practical implementation of this model is expected to increase the safety of residents in Chiang Mai's urban area by providing more reliable flood warnings, thereby protecting lives and property. Additionally, it can significantly reduce the overall economic losses caused by flooding, contributing to improved quality of life and economic stability within the community.

Suggestions for Future Research

- For the 9-hour water level forecasting models, it is recommended to include data from additional upstream stations to further improve forecasting accuracy.

- It would be beneficial to experiment with combining both MA and EMA data to compare forecasting performance.

- Other variable selection techniques should be explored alongside ANN models to further enhance the water level forecasting models and compare their effectiveness.

- Consideration could be given to using other deep learning models for water level forecasting and comparing their forecasting performance with the current models.

7. References

[1] Mosavi A, Ozturk P, Chau KW. Flood prediction using machine learning models: Literature review. Water. 2018;10(11):1536.

[2] Wee WJ, Zaini NAB, Ahmed AN, El-Shafie A. A review of models for water level forecasting based on machine learning. Earth Sci Inform. 2021;14:1707–28.

[3] Phuttithaworn W. Coping with flood situations. Environ J. 2012;16(1):45–54. Thai.

[4] Upper Northern Region Hydrology and Water Management Center. Announcement from the Irrigation Office No. 1, Issue 3/2022: Monitoring water levels in the Ping River area, Station P.1, Nawarat Bridge, Mueang District, Chiang Mai Province [Internet]. 2022. Available from:http://www.hydronet/Data/Admin/book/file/E1236-2565.pdf (Accessed 2024 Nov 15).

[5] Upper Northern Region Hydrology and Water Management Center. Announcement of the Irrigation Office No. 1, Issue 20/2024: Notification of critical water levels in the Ping River, Station P.1, Nawarat Bridge, Mueang District, Chiang Mai Province [Internet]. 2024. Available from:http://rio1.rid.go.th/main.php?p=2&id=2621 (Accessed 2024 Nov 15).

[6] Upper Northern Region Hydrology and Water Management Center. Hourly water level data at P.1 station Nawarat Bridge, Ping River, Wat Ket Subdistrict, Mueang District, Chiang Mai Province [Internet]. Available from: http://hydro-1.rid.go.th/Data/HD-04/hourly/water_today.php (Accessed 2024 Oct 20).

[7] Plate EJ. Early warning and flood forecasting for large rivers with the lower Mekong as example. J. Hydro-Environ Res. 2007;1(2):80–94.

[8] Upper Northern Region Hydrology and Water Management Center, Chiang Mai city flood warning, [Brochure], Royal Irrigation Department, n.d.

[9] Upper Northern Region Hydrology and Water Management Center. Hydrologic diagram of the Ping River Basin [Internet]. Available from: http://www. hydro-1.net/ Data/ HD-06/diagram.php (Accessed 2024 Dec 14).

[10] Box GE, Jenkins GM, Reinsel GC, Ljung GM. Time series analysis: forecasting and control. Hoboken (NJ): John Wiley & Sons; 2015.

[11] Lotysh V, Gumeniuk L, Humeniuk P. Comparison of the effectiveness of time series analysis methods: SMA, WMA, EMA, EWMA, and Kalman filter for data analysis. Informatyka Automatyka Pomiary Gospod Ochr Środowiska. 2023;13(3):71–4.

[12] Hermawan A, Ananda S, Junaedi E, Edy. Enhancing stock price forecasting: Optimizing neural networks with moving average data. Bit-Tech [Internet]. 2025;7(3):798–808. Available from: https://doi.org/10.32877/bt.v7i3.2196.

[13] Formis D, Colletto A, Delsanto D, Dey K, Demichelis F. Mixing neural networks and exponential moving averages for predicting wireless links behavior. In: Proceedings of the 2024 IEEE 7th International Conference on Industrial Cyber-Physical Systems (ICPS); 2024 May. p. 1–6. Available from: https:// doi.org/ 10.1109/ICPS59941. 2024. 106 40038.

[14] Kutner MH, Nachtsheim CJ, Neter J, Li W. Applied linear statistical models. New York: McGraw-Hill; 2005.

[15] Chaipimonplin T. Investigation internal parameter of neural network model for flood forecasting at Upper River Ping, Thailand. KSCE J Civ Eng. 2016;20(1):478–84.

[16] Chaipimonplin T. Comparison learning algorithms of artificial neural network model for flood forecasting, Chiang Mai, Thailand. In: Syme G, Hatton MacDonald D, Fulton B, Piantadosi J. editors. Proc. 22nd Int. Congr. Model. Simul. Soc. Aust. N. Z. (MODSIM 2017); 2017 Dec. p. 473–9. ISBN: 978-2-9872143-7-9.

[17] Shumway RH, Stoffer DS. Time Series Analysis and Its Applications: With R Examples. 4th ed. New York: Springer; 2017.

[18] Zhang X, Wang R, Wang W, Zheng Q, Ma R, Tang R, Wang Y. Runoff prediction using combined machine learning models and signal decomposition. J. Water Clim Change. 2025;16(1):230–47.

[19] Akrami SA, El-Shafie A, Naseri M, Santos CA. Rainfall data analyzing using moving average (MA) model and wavelet multi-resolution intelligent model for noise evaluation to improve the forecasting accuracy. Neural Comput Appl. 2014;25:1853–61.

[20] Vergura S. Bollinger bands based on exponential moving average for statistical monitoring of multi-array photovoltaic systems. Energies. 2020;13(15):3992.

[21] Zhou X, Jiang T. Metamodel selection based on stepwise regression. Struct Multidiscip Optim. 2016;54:641–57.

[22] Shaik NB, Pedapati SR, Taqvi SAA, Othman AR, Dzubir FAA. A feed-forward back propagation neural network approach to predict the life condition of crude oil pipeline. Processes. 2020;8(6):661.

[23] Chaipimonplin T, See LM, Kneale PE. Improving neural network for flood forecasting using radar data on the Upper Ping River. In: Proc. MODSIM 2011; 2011 Dec. p. 1070–6.

[24] Gholamy A, Kreinovich V, Kosheleva O. Why 70/30 or 80/20 relation between training and testing sets: A pedagogical explanation. Int J. Intell Technol Appl Stat. 2018;11(2):105–11.

[25] Willmott CJ, Matsuura K. Advantages of the mean absolute error (MAE) over the root mean square error (RMSE) in assessing average model performance. Clim Res. 2005;30(1):79–82.

[26] Wooldridge JM. Introductory Econometrics: A Modern Approach. 6th ed. Boston (MA): Cengage Learning; 2016.

[27] Ajiono A, Hariguna T. Comparison of three time series forecasting methods on linear regression, exponential smoothing and weighted moving average. Int J. Inform Inform Syst. 2023;6(2):89–102.

[28] Thai Meteorological Department. Chiang Mai Meteorological Warning [Internet]. Available from: https://cmmet.tmd.go.th/warning/cm_warn.html (Accessed 2025 May 21).

[29] Chaipimonplin T, Mukdasanit S. CM Water Forecast Mobile Application Version 1.0, presented at The 3rd Trilateral Symposium on Sustainability: Strategies for Climate Action and Mitigation of Climate Change Impacts, Chiang Mai, Thailand; organized by Chiang Mai University; 2020.

Design and Analysis of an SME-Level Pulsed Electric Field Device for Extracting Bioactive Compounds from Black Rice

Supakiat Supasin[1], Panich Intra[2], Pornsawan Sombatnan[2], Sureewan Rajchasom[2], Padipan huangsorn[1], Thanachat Mahawan[3] and Chatchawan Kantala[2*]

[1] Faculty of Engineering, Rajamangala University of Technology Lanna, 128 Huay Kaew Road, Chang Phueak, Mueang Chiang Mai, Chiang Mai, Thailand, 50300.

[2] Research Unit of Applied Electric Field in Engineering (RUEE), College of Integrated Science and Technology, Rajamangala University of Technology Lanna 98 Moo 8, Pa Pong, Doi Saket, Chiang Mai, Thailand, 50220.

[3] Office of Facilities and Services Management, Payap University, 272 Moo 2, San Phanet, San Sai, Chiang Mai, Thailand, 50210.

[*]Corresponding author: chatchawan_kantala@yahoo.com, Telephone number: +66-642974595

Received: 1 January 2025, Revised: 24 November 2025, Accepted: 27 November 2025

Abstract

This research developed a small-scale Pulsed Electric Field (PEF) machine to extract bioactive compounds from black rice grown in Doi Saket and assessed its extraction efficiency. The primary voltage ranged from 0 to 220 V, with secondary high voltage AC and DC outputs spanning from 0.68 to 15.00 kV and 0.96 to 21.21 kV, respectively. The experiment used a ratio of 1 kg of black rice to 2 L of water, with electric field strengths of 4, 5, and 6 kV/cm at a frequency of 1 Hz, varying the number of pulses between 1,000, 3,000, and 5,000. Results showed that 6 kV/cm and 5,000 pulses yielded the highest anthocyanin content (3.23±0.04 mg/L), which significantly differed from other conditions (p<0.05). The highest antioxidant levels were observed at 4 kV/cm for 1,000 pulses and 5 kV/cm for 1,000 pulses (77.86±0.67% and 76.91±0.71%, respectively), though these levels decreased in comparison to traditional extraction, showing statistical significance (p<0.05). However, a higher pulse count led to an increase in anthocyanin content. Furthermore, increased electric field intensity raised antioxidant yields, though this effect plateaued beyond a certain point. Optimal extraction conditions were achieved at 5 kV/cm and 3,000 pulses, yielding anthocyanin and antioxidant contents of 1.02±0.04 mg/L and 59.72±0.34%, respectively. The extraction process was most effective when temperatures remained below 50°C (without a cooling system) and pressure was kept at 1 atm. Additionally, the study developed a PEF prototype for bioactive compound extraction from black rice.

Keywords: Pulsed Electric Field, Extraction, Black Rice, Bioactive Compounds, Anthocyanin, Antioxidant

1. Introduction

Khao Gam Doi Saket is a variety of sticky rice known for its black color. The name "Doi Saket" comes from the area where it is grown, specifically in the village of San Pu Loei, San Pu Loei Sub-district, Doi Saket District, Chiang Mai Province. In addition to being grown in Chiang Mai, Khao Gam is also found in other provinces and regions, such as the central region, where it is commonly known as "black sticky rice." In the southern region, it is referred to as "Niaw Dam" or sometimes as "Khao Nil" due to the dark red or deep red color of the grain. There are several varieties of Khao Gam in Thailand, and in Chiang Mai Province, specifically, the Doi Saket Campus of Rajamangala University of Technology Lanna is home to a group of farmers cultivating the Doi Saket variety of Khao Gam. This variety has been registered and certified by the Department of Agriculture under the Plant Varieties Protection Act B.E. 2518 (1975). The rice variety was improved in 1995 by the Institute of Science and Technology Research at Chiang Mai University [1]. Khao Gam is recognized for its medicinal and herbal properties. It was found that Khao Gam Doi

Saket contains Gamma Oryzanol, which is three times higher than that in white rice. Additionally, it contains dark blue to purplish-black pigments, such as Proanthocyanidin (Cyanidin 3-glucoside), Anthocyanin, and is rich in vitamin E [2]. Khao Gam Doi Saket is promoted for cultivation in the Doi Saket District of Chiang Mai Province. A group of farmers in the village of San Pu Loei, San Pu Loei Sub-district, Doi Saket District, have come together to grow this rice on an area of 20 rai, yielding 750 kg per rai. The cultivated area is expected to expand, with more farmers showing interest in joining the group each year. Currently, the group sells milled rice to private companies. However, the group sees great potential in processing Khao Gam into various products, which would add value and create jobs for people in the village. As a result, a group of female farmers has been established to process products from Khao Gam. At present, the group has no products because they have not received support from any organizations, nor do they possess the necessary knowledge.

Khao Gam Doi Saket is rich in essential nutrients, including carbohydrates, fats, proteins, vitamins A, B1, B2, E, calcium, and iron. It also contains high levels of flavonoids and antioxidant compounds that surpass those in white rice [3]. Flavonoids, a type of polyphenol, are composed of 15 carbon atoms arranged in an aromatic ring structure with hydroxyl groups. More than 4,000 types of flavonoids exist in nature, predominantly in the glycoside form. Key flavonoids include flavanol, flavanone, flavone, isoflavone, catechins, and anthocyanins [4]. Further studies revealed that Gamma Oryzanol, when working in conjunction with Anthocyanin, has antioxidant properties that help slow down aging, prevent cancer, obesity, hypertension, heart disease, and memory loss, boost immunity, and lower cholesterol levels [5].

Anthocyanins and gamma-oryzanol, found in Khao Gam, are pigments ranging from red to purple or blue. Anthocyanins are water-soluble, pH-sensitive compounds that belong to the flavonoid group [6]. Their color changes with pH: red in acidic conditions, purple at neutral pH, and blue in alkaline conditions. These pigments are stored in the vacuole sap and play a protective role against environmental stressors. However, they are prone to degradation due to high temperatures, oxygen, and sugar concentration [7]. Anthocyanins are widely applied for their antioxidant properties in various industries, including food, cosmetics, and health products. Their chemical structure includes aglycone, sugar, and acyl groups, with 15 carbon atoms per molecule. Common anthocyanidins include cyanidin, peonidin, and others, contributing to the distinctive characteristics of Khao Gam [8, 9].

The major chemical composition of Khao Gam Doi Saket is anthocyanin, which is sensitive to heat extraction. Conventional extraction methods, such as boiling, Soxhlet extraction, and maceration, have been employed for centuries. However, these traditional techniques are often time-consuming, energy-intensive, and involve high temperatures, which can lead to the degradation of heat-sensitive nutrients [10]. To overcome these limitations, emerging extraction technologies that operate under mild or cold processing conditions are being explored to enhance anthocyanin yield and preserve nutritional quality. The pulse electric field extraction (PEF) is well known for the extraction of pure dry matter, carotenoids, vitamins, sucrose, proteins, inulin, and other substances [11]. This technique offers a promising alternative to traditional methods, particularly for thermolabile compounds such as anthocyanins. PEF is a non-thermal technology that uses high-voltage pulses (1-20 μs) at intensities of 20-50 kV/cm to induce electroporation, making it effective for applications such as extraction, microbial inhibition, and pickling. The process operates without heat or chemicals, preserving the taste, aroma, color, and nutritional value of food products. A typical PEF system comprises three components: a DC power supply to convert AC into high-voltage DC, a pulse modulator to generate pulsed electric energy, and a treatment chamber where samples are exposed to the

electric field. The efficiency of PEF depends on factors like pulse shape, conductivity, electric field strength, and frequency [12, 13]. Eshtiaghi and Knorr [14] reported enhanced sugar extraction from beetroot using PEF (1.2-2.5 kV/cm), while Rastogi et al. [15] demonstrated improved mass transfer and cell disruption in carrots. Bobinaite et al. [16] observed a 60% increase in anthocyanin content and a 31% rise in antioxidant activity in PEF-treated blueberries. Similarly, Zhi-Hong et al. [17] found enhanced pigment and antioxidant retention in spinach. Francisco et al. [18] reported that PEF increased total polyphenol content and antioxidant capacity in borage by up to 13.7-fold. Moreover, PEF has also been successfully applied in combination with freeze–thaw techniques to enhance pigment extraction efficiency from cyanobacteria [24]. In peaches, PEF significantly improved the extraction of phenolics and flavonoids using only water as a solvent [19]. Overall, PEF offers advantages over conventional thermal methods, including reduced processing time, lower energy input, and better preservation of thermolabile compounds, making it a sustainable and efficient approach for extracting sensitive phytochemicals such as anthocyanins.

Therefore, based on the nutritional properties of Khao Gam and its ability to enhance immunity against various diseases, as well as the fact that the pigments in Khao Gam can be extracted using advanced technology without destroying their beneficial properties, it can be developed into health products, cosmetic products, or other related items. Although PEF technology has been widely studied and applied internationally for the extraction of bioactive compounds in various agricultural products, most existing research and commercial applications are concentrated in large-scale or industrial settings. In Thailand, however, the adoption and development of PEF technology at the small and medium enterprise (SME) level remain limited. There is a noticeable lack of localized studies focusing on the design, optimization, and practical implementation of PEF systems that are affordable, scalable, and tailored to the needs of Thai SMEs, particularly for the extraction of valuable compounds from indigenous crops such as Khao Gam. The project has thus been designed to analyze and develop a pulse electric field (PEF) machine for SMEs to extract bioactive compounds from Khao Gam. The project aims to test the extraction efficiency of the PEF machine, study the optimal electric field intensity, and determine the appropriate number of pulses for extracting bioactive compounds from Khao Gam, in comparison with the traditional extraction method.

2. Research methodology

2.1 Design and construction of an extraction machine.

The power module consisted of a high-voltage transformer, rectifier, and pulse-forming network with solid-state switching, similar to designs reported by Kantala et al. (2022) [12]. The PEF generator produced monopolar square-wave pulses with a pulse width of 2.5 µs, a fast rise time (<500 ns), and a frequency of 1 Hz, ensuring effective electroporation while minimizing thermal effects.

The design and construction of the extraction machine began with a study of theoretical concepts, a review of relevant Literature, and the design of subcomponents for the PEF machine and treatment chamber. The treatment chamber, with a 500 mL capacity, features two flat stainless-steel electrodes (316L) separated by food-grade Teflon insulation. The process included creating a prototype, drafting detailed plans, and sourcing materials and equipment for assembly. Each component was tested individually before assembling the complete PEF machine. The system was then tested for its performance in extracting bioactive compounds from black rice, and the results were analyzed. Table1 outlines the system specifications.

Table 1. Properties of the bioactive compound extraction system to be developed for black rice

Design Conditions	Specifications
Principle	Electroporation
Size	SME
Type of food	Black rice
Electric field strength	> 2 kV/cm
Dimensions of the black rice extraction chamber	Gap: 4.0 cm and 500 ml
Voltage at electrode poles Maximum output current	≤ 20 kV ≤ 2 kA at a pulse width of approximately 2.5 µs
Maximum output current	≤ 2 kA
Pulse width	~ 2.5 µs
Pulse frequency	1 – 5 Hz
Voltage	Positive electrode
Working fluid pressure	1 bar
Production capacity	At least 5,000 ml/hr of bioactive composite extract
Efficiency	Better extraction of bioactive compounds from black rice compared to traditional extraction methods
Maintenance	Easy to disassemble, clean, and install

2.2 Testing the efficiency of bioactive compound extraction from black rice using the PEF machine.

The efficiency of bioactive compound extraction from black rice using the PEF machine was evaluated by selecting and washing black rice, followed by extracting with the PEF machine. A rice-to-water ratio of 1:2 was maintained, with adjustments to the electric field intensity at 4, 5, and 6 kV/cm at a frequency of 1 Hz. The number of pulses was varied between 0 (Control), 1,000, 3,000, and 5,000 pulses, respectively. These results were compared to those from the conventional extraction method for bioactive compounds in black rice. The process for testing bioactive compounds from black rice is illustrated in Figure 1.

2.3 Black Rice

The black rice used for extraction was sourced from the Doi Saket community enterprise and is characterized by its dark purple or black stems, purple husks, and grains measuring approximately 3.3 mm wide, 9.7 mm long, and 1.91 mm thick Figure 2. Bioactive compounds were extracted using a PEF machine, and the results were analyzed both before and after extraction. Physical properties, including L^*, a^*, and b^* values, were measured in triplicate, and data were processed in Microsoft Excel with statistical analysis performed using the MINITAB ANOVA-t test. Chemical properties, such as total anthocyanin content and antioxidant activity, were also evaluated under the same statistical protocol.

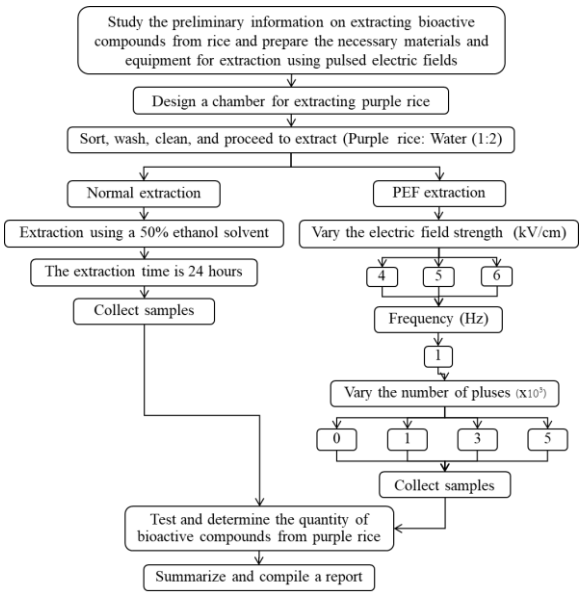

Figure 1 Experimental procedure

The initial experimental ranges (4-6 kV/cm; 1,000-5,000 pulses; 1 Hz) were selected based on prior PEF Literature, which typically reports effective electroporation at 1-20 kV/cm and 500-10,000 pulses. These parameters were chosen to ensure safe operation suitable for SME-scale equipment while covering an effective electroporation window for bioactive compound extraction.

2.4 Study of Optimal Conditions for Pulsed Electric Field Extraction Process

The extraction of bioactive compounds from black rice is performed using two methods: solvent extraction and pulsed electric field extraction. For the solvent extraction, the ratio used is 1 kg of purple rice to 2 L of water. Water and 50% ethanol are used as solvents, and the extraction time is 24 hours. Response surface

methodology (RSM) was used for optimization of PEF conditions. The 2-factor factorial design was used in designing the PEF treatment. For the pulsed electric field extraction, experiments are conducted with electric field strengths of 4, 5, and 6 kV/cm at a frequency of 1 Hz, and the number of pulses is varied at 1,000, 3,000, and 5,000 pulses, respectively. The model regression was calculated for the optimum point by the MINITAB program.

Figure 2 Doi Saket Black Rice Variety

2.5 Analysis of the Chemical Properties, Bioactive Compounds, and Key Components of the Concentrated Black Rice Beverage Extract

After measuring the physical properties, including color, the concentrated extract sample from Doi Saket black rice was analyzed for its chemical properties and bioactive compounds. These include total flavonoid content, anthocyanin content, antioxidant activity, and the levels of cyanidin and peonidin. The analysis details are as follows:

The analysis of total flavonoid content was performed using the aluminum chloride colorimetric method with quercetin as the standard. The total flavonoid content was determined by comparing it to a standard concentration graph (ranging from 10-100 mg/ml). A 1 mL sample was taken, and 1 mL of 10% aluminum chloride was added, followed by shaking the mixture. Then, 1 M potassium acetate was added, and the mixture was shaken again. The sample was kept in the dark for 45 minutes, after which the absorbance was measured using a spectrophotometer at a wavelength of 415 nm. The flavonoid content in the extract was calculated by comparing it to the quercetin standard graph (Y = ...x +..., R^2 = 0.999) and expressed as milligrams of quercetin equivalent per gram of extract (mg of quercetin equivalent/g extract) [20].

The analysis of anthocyanin content was performed using the pH differential method. A 1 mL sample was taken and diluted with distilled water to a final volume of 10 ml. The mixture was shaken well and centrifuged at 3,000 rpm for 15 minutes. Only the clear supernatant was collected, and 3 mL of it was diluted with pH 1 and pH 4.5 buffer solutions to a final volume of 30 ml. The solution was left to stand for 30 minutes, after which the absorbance was measured using a spectrophotometer at wavelengths of 510 nm and 700 nm [21]. Anthocyanin content was calculated based on the absorbance of the solution using the appropriate formula:

$$\text{The total anthocyanin content.} = \frac{\text{Adiff}\times MW\times df\times 1000}{\varepsilon}$$

where, Adiff = (A510-A700) pH1- (A510-A700) pH4.5, *Mw* = 449.2 g mol, ε = 26900 M cm, dilution factor (*df*) = 1.

The analysis of antioxidant activity was performed using the DPPH radical scavenging assay. A 0.12 mM standard solution of 2,2-diphenyl-1-picrylhydrazyl (DPPH) was prepared. For the test sample, 200 µl of the sample was mixed with 1.8 mL of methanol and 2 mL of DPPH solution. For the control, 2 mL of methanol was mixed with 2 mL of DPPH solution, and for the blank, 4 mL of methanol was used [22]. The antioxidant activity was calculated using the percentage inhibition formula:

$$\text{The percentage of inhibition} = \frac{(A517_{control}-A517_{sample})\times 100}{A517_{control}}$$

Where, $A517_{control}$ = absorbance of control sample at 517 nm, $A517_{sample}$ =absorbance of test sample at 517 nm.

The analysis of cyanidin and peonidin content was performed using High Performance Liquid Chromatography (HPLC) with a C18 column. Mobile phase A consisted of water and formic acid in a 90:10 v/v ratio, and Mobile phase B consisted of water, acetonitrile, methanol, and formic acid in ratios of 40:22, 5:22, and 5:10 v/v. The ratio of Mobile phase A to Mobile phase B was 50:50 v/v, with a flow rate of 1

ml/min. Detection was performed at a wavelength of 535 nm, with an injection volume of 20 µl. The analysis was carried out at a temperature of 4 °C, and the column temperature was maintained at 30°C [23].

2.6 Statistical Analysis of Experimental Results

Statistical analysis of the data was performed by analyzing the physical and chemical results from each experiment, with all analyses conducted in triplicate. Data were expressed as mean ± standard deviation (mean ± SD) using MINITAB Statistical Software version 20

3. Results and Discussion

3.1 Results of the Design, Construction, and Testing of the PEF Machine

3.1.1 Design Results

The design of a Pulse Electric Field Machine for SMEs to develop a Process for Extracting Bioactive Compounds from Black Rice, using SolidWorks software as shown in Figure 3.

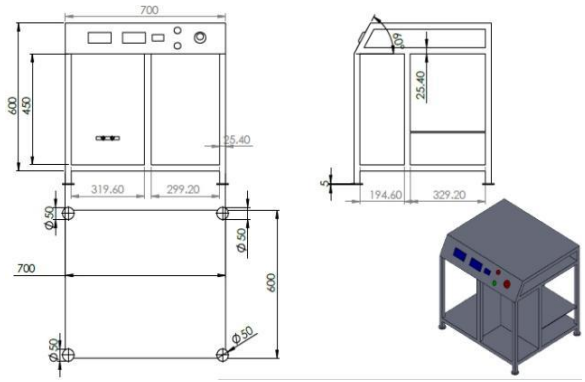

Figure 3 The pulsed electric field (PEF) device schematic drawing diagram.

3.1.2 Construction Results of the PEF Machine

A prototype PEF machine was constructed with a maximum voltage of 20 kV, a frequency range of 1-5 Hz, a pulse width of approximately 2.5 µs, and an electric field intensity greater than 2 kV/cm, as shown in Figure 4, which was designed for extracting bioactive compounds from black rice.

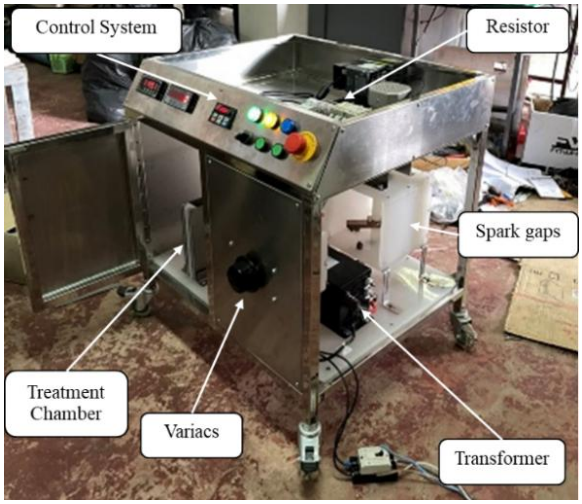

Figure 4 Internal components of the PEF device.

3.1.3 Performance Testing Results of the PEF Machine

The electrical performance of the pulse power supply was evaluated by measuring the primary and secondary voltages of the high-voltage transformer across the operating range. Table2 summarizes the energy requirements at different electric field strengths (4, 5, and 6 kV/cm) and pulse numbers (1,000, 3,000, and 5,000). Table3 further presents the relationship between the primary voltage, high-voltage AC output, and rectified DC voltage of the transformer module. The primary voltage was varied from 0 to 220 V, demonstrating that energy consumption increased proportionally with both electric field intensity and pulse count.

Table 2 Results of the relationship between electric field intensities, number of pulsed, and energy.

Electric Field Intensities (kV/cm)	Number of Pulsed (Pulsed)	Energy (kJ/L)
4	1,000	160
	3,000	480
	5,000	800
5	1,000	250
	3,000	750
	5,000	1,250
6	1,000	360
	3,000	1,080
	5,000	1,800

Table 3 Results of the relationship between primary voltage, secondary high AC voltage, and high DC output voltage.

Primary Voltage (V)	High Secondary Alternating Voltage (kV)	High Output Direct Voltage (kV)
0	0.06	0.09
10	0.68	0.96
20	1.36	1.93
30	2.05	2.89
40	2.73	3.86
50	3.41	4.82
60	4.10	5.79
70	4.77	6.75
80	5.46	7.71
90	6.36	8.68
100	6.82	9.64
110	7.50	10.61
120	8.18	11.57
130	8.86	12.53
140	9.55	13.50
150	10.23	14.46
160	10.91	15.43
170	11.60	16.39
180	12.27	17.35
190	12.96	18.32
200	13.64	19.28
210	14.32	20.25
220	15.00	21.21

The purpose of Table 3 is to verify the transformer step-up ratio and DC output stability of the custom pulse power module, serving as an indirect indicator of delivery efficiency. Due to proprietary technical constraints, only input-output characterization is reported; however, the results are consistent with previously reported PEF power system performance [12], supporting the reliability of the design for SME-scale operation.

3.2 Results of the Extraction Conditions Study for Doi Saket Black Rice

3.2.1 Physical Characteristics of Doi Saket Black Rice Extract

The black rice extracts obtained using plain water extraction and PEF extraction methods are shown in Figure 5. The physical characteristics of the black rice extract are liquid with a deep red to dark purple color. This is due to the presence of anthocyanin pigments in the black rice grains, which are highly soluble in water.

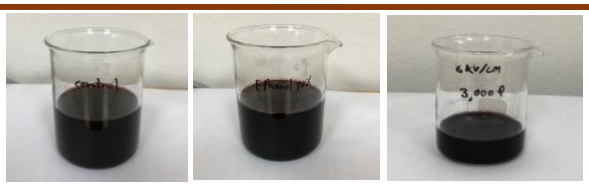

(a) (b) ©

Figure5 Physical characteristics of black rice extract: (a) Control; (b) 5 0 % Ethanol; (c) Extracted with PEF.

The distinct coloration observed in the PEF-treated extract reflects the efficient release of anthocyanin pigments from the rice matrix. This outcome aligns with the applied PEF waveform characteristics (monopolar square-wave, 2.5 µs pulse width, <500 ns rise-time), which promote electroporation-driven cell disruption while minimizing thermal effects. Consequently, thermolabile bioactive compounds are better preserved during extraction.

3.2.2 Percentage Yield and pH Analysis Results of Black Rice Extract

In the study of optimal conditions for PEF extraction of black rice, pulse numbers of 1,000, 3,000, and 5,000 were tested and compared with 50% ethanol extraction over 24 h [25]. Ethanol extraction yielded a total anthocyanin content of 1.59 ± 0.16 mg/L. The highest anthocyanin content, 3.23 ± 0.04 mg/L, was achieved with PEF at 6 kV/cm and 5,000 pulses, significantly higher than all other methods with 95% confidence (p<0.05). Antioxidant activity was highest at 4 kV/cm and 1,000 pulses (77.86 ± 0.67%) and 5 kV/cm and 1,000 pulses (76.91 ± 0.71%), both significantly different from other conditions at 95% confidence (p<0.05).

The optimal conditions for extracting valuable compounds from Doi Saket black rice were achieved using PEF at 5 kV/cm with 5,000 pulses, yielding a total anthocyanin content of 2.58 ± 0.04 mg/L and antioxidant activity of 54.77 ± 3.48%, as shown in Figure 6. Compared to plain water extraction (Control), PEF extraction produced higher levels of bioactive compounds in less time. Higher voltages and pulse numbers generally increased anthocyanin content, with more pulses resulting in higher yields. However, increased extraction energy reduced antioxidant activity, likely due to heat generation during extraction,

which may diminish antioxidant effectiveness [26]. Several studies support the observation that high electric field intensity and excessive pulse numbers in PEF treatment can lead to a decline in antioxidant activity. Mahnič-Kalamiza et al. [27] noted that excessive energy input during electroporation could cause the degradation of bioactive compounds due to local heating and membrane damage. Similarly, Zhang et al. [28] reported that when extracting pigments from spinach, field intensities beyond the optimal range reduced antioxidant yield, likely due to structural instability. In blueberry processing, Pataro et al. [29] also found that increasing the field strength beyond 1 kV/cm did not improve antioxidant content and could potentially cause compound degradation. These findings align with the current study's results, emphasizing the importance of optimizing PEF conditions to maximize bioactive compound retention without compromising antioxidant integrity.

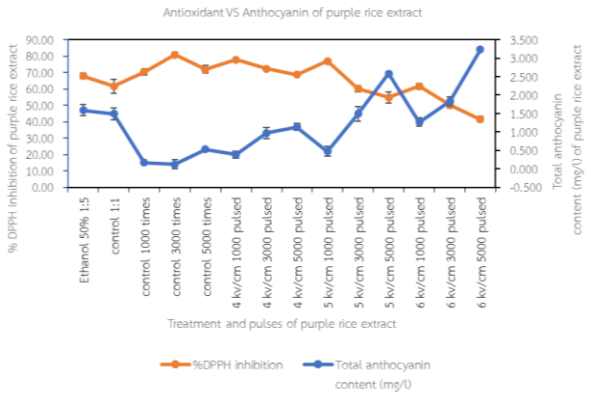

Figure 6 Comparison of total anthocyanin content (mg/L) and antioxidant activity from extractions at electric field intensities of 4, 5, and 6 kV/cm with 1,000, 3,000, and 5,000 pulses.

3.2.3 Analysis of Optimal Extraction Factors for Black Rice Using Response Surface Methodology (RSM)

Based on the experimental results, the optimal conditions for extracting black rice were determined to be a voltage of 5 kV/cm with 5,000 pulses. As shown in Figure 6, higher electric field intensity and pulse numbers increased anthocyanin content, whereas antioxidant activity tended to decrease. This indicates that although stronger PEF treatment enhances pigment release, excessive energy input may promote degradation of antioxidant compounds though local heating. These findings are consistent with previous studies reporting reduced antioxidant stability under high-intensity PEF [30, 31]. Thus, the results highlight the need for optimization to balance anthocyanin yield and antioxidant retention. The Response Surface Methodology from MINITAB software was used to further refine the extraction conditions. The analysis revealed that a voltage of 6 kV/cm and 5,000 pulses resulted in the highest total anthocyanin content of 3.25 mg/L, while extraction at 4 kV/cm with 1,000 pulses provided the highest antioxidant activity of 79.64%, as shown in Figure 7.

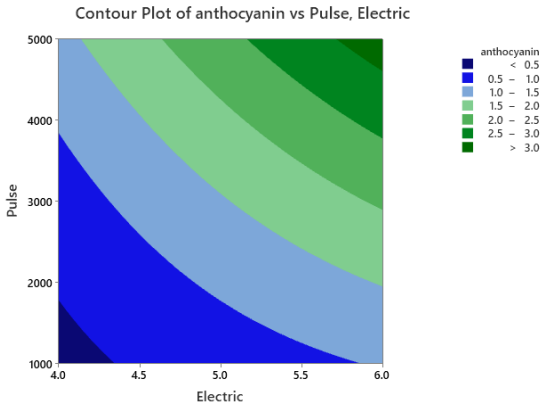

(a) RSM results for the total anthocyanin content of black rice extract.

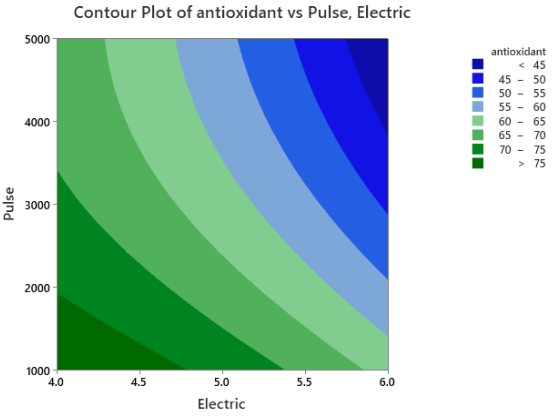

(b) RSM results for the antioxidant activity of black rice extract.

Figure 7 Response Surface Methodology (RSM)

Subsequently, the Response Optimizer function was utilized to identify the optimal factors that provide consistent conditions for extracting both the total anthocyanin content and antioxidant

activity. The optimal extraction conditions determined were a voltage of 4.63 kV/cm and 5,000 pulses, yielding a total anthocyanin content of 1.99 mg/L and an antioxidant activity of 61.10%, as depicted in Figure 8. The conditions that were closest to achieving both high total anthocyanin content and antioxidant activity involved using a voltage of 5 kV/cm with 3,000 pulses, resulting in a total anthocyanin content of 1.49 ± 0.19 mg/L and an antioxidant activity of 60.13 ± 1.95%, respectively.

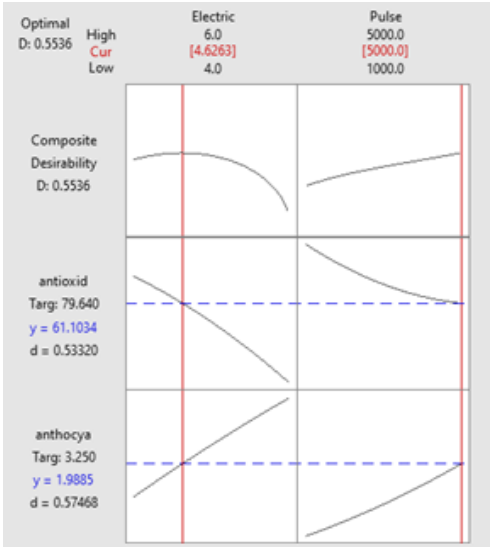

Figure 8 Optimal conditions for black rice extraction based on the optimal values of total anthocyanin content and antioxidant activity.

3.2.4 Cost-Benefit Consideration and SME Scalability

Compared with conventional solvent extraction, the PEF method substantially shortens the processing time (from ~24 h to only a few minutes) and eliminates solvent costs by utilizing water as the extraction medium. Although high voltage is required, the energy consumption per batch remains low due to the short pulse duration and low-frequency operation, with an estimated energy use of approximately 0.15-0.20 kWh per kg of black rice. Additionally, the PEF system is compact, low-maintenance, and suitable for SMEs. Importantly, the developed PEF machine achieved comparable or higher anthocyanin yields within minutes, demonstrating significant advantages in both processing efficiency and solvent reduction relative to traditional extraction. Overall, these findings indicate that PEF technology offers a scalable, energy-efficient, and solvent-free extraction strategy suitable for SME-level production of functional foods and bioactive compounds.

4 Conclusions

The extraction machine designed for Doi Saket black rice effectively extracted anthocyanins under optimal conditions of 5 kV/cm with 3,000 pulses or 4.63 kV/cm with 5,000 pulses, as determined by the Response Optimizer. The PEF machine allows for primary voltage adjustments from 0 to 220 V, producing secondary high voltages of 0.68-15.00 kV and DC output voltages of 0.96-21.21 kV. During extraction, the temperature remained below 50°C without cooling, at room temperature, and 1 atm pressure. This SME-level PEF machine demonstrates high efficiency in bioactive compound extraction, particularly anthocyanins, from black rice. When compared with 24-hour conventional maceration, the optimized PEF conditions produced comparable or superior anthocyanin yields within minutes, while significantly lowering solvent usage and processing time. Collectively, this work demonstrates the technical feasibility and industrial relevance of PEF as a rapid, energy-efficient, and solvent-free extraction technology for SME-level production of bioactive-rich functional ingredients.

5. Acknowledgements

The results of this research and development project were funded by the Thailand Science Research and Innovation (TSRI) for the fiscal year 2021, Basic Research Fund (Contract number; 2564Basic011). We would like to thank Mr. Surapol Sudakaew, President of the Doi Saket Black Rice Community Enterprise, Materials and Medical Innovation Research Unit, Faculty of Engineering, RMUTL, and Research Unit of Applied Electric Field in Engineering (RUEE), College of Integrated Science and Technology Rajamangala University of Technology Lanna during the project.

6. References

[1] Lanna Rice Research center. Khoa Gam Lanna. 2022. Available from: https://lanna-rice.cmu.ac.th/pages/view/24. [Accessed 12 January 2024].

[2] Fongfon S, Pusadee T, Prom-u-thai C, Rerkasem E, Jamjod S. Diversity of Purple Rice (Oryza sativa L.) Landraces in Northern Thailand. Agronomy. 2021;11:2029.

[3] Nuananong S, Nakamon K, Weeraphong C. Flavonoid content, total phenolic compounds and their anti-free radicals of Thai rice extracts. 2001. Available from: http:// www.research.cmru.ac.th/research59/ris/view.php?no=545. [Accessed 12 January 2024].

[4] Narikawa T, Shinomiya H, Fuji T. A beta-rutinosidase from Penicillium rugulosum IFO 7242 that is a peculiar flavonoid glycosidase. Biosci Biotechnol Biochem. 2000; 64:1317-19.

[5] Patras A, Brunton NP, O'Donnell C, Tiwari BK. Effect of thermal processing on anthocyanin stability in foods; mechanisms and kinetics of degradation. Trends Food Sci Technol. 2010:3-11.

[6] Lazze MC, Savio M, Pizzala R, Cazzalini O, Perucca P, Scovassi AI, Stivala LA, Bianchi L. Anthocyanins induce cell cycle perturbations and apoptosis in different human cell lines. Carcinogenesis. 2004;25:1427–33.

[7] Nithiya R. Food Chemistry. 5th ed. Bangkok: Odeon Store Publishing; 2002.

[8] Department of Science Services. Anthocyanins. Information processing is ready for use. 2010;1-15.

[9] Arusa C. Extraction and methods for analyzing anthocyanins. SWU J. Sci Technol. 2011;3:26-36.

[10] Tena N, Asuero AG. Up-To-Date Analysis of the Extraction Methods for Anthocyanins. Antioxidants. 2022;11:286.

[11] Bozinou E, Karageorgou I, Batra G, Dourtoglou VG, Lalas SL. PEF extraction and antioxidant activity of Moringa oleifera leaves. Beverages. 2019;5:8.

[12] Kantala C, Supasin S, Intra P, Rattanadecho P. Evaluation of pulsed electric field and conventional thermal processing for microbial inactivation in Thai orange juice. Foods. 2022;11:1-10.

[13] Eugene V, Nikolai IL. Extraction from foods and biomaterials enhanced by pulsed electric energy. Innov Food Sci Emerg Technol. 2016:31-56.

[14] Eshtiagh MN, Knorr D. High electric field pulse pretreatment: potential for sugar beet processing. J. Food Eng. 2002;52:265-72.

[15] Rastogi NK, Eshtiaghi MN, Knorr D. Accelerated mass transfer during osmotic dehydration of electrical field pulse pretreated carrots. J. Food Sci. 2006; 64: 1020-23.

[16] Bobinaite R, Pataro G, Lamanauskas N, Satkauskas S, Viskelis P, Ferrari G. Application of pulsed electric field in extraction of blueberry juice and bioactive compounds. J. Food Sci Technol. 2015; 52: 5898-905.

[17] Zhi-Hong Z, Lang-Hong W, Xin-An Z, Zhong H, Man-Sheng W. Effect of pulsed electric fields on pigments extracted from spinach. Innov Food Sci Emerg Technol. 2017;43:26–34.

[18] Francisco JS, Elisa L, Juan JC, Javier R, Maria PA. Aqueous extraction of polyphenols from borage leaves enhanced by PEF. Ind Crops Prod. 2015;65:390–6.

[19] Diego R, Maria EV, Elisa L, Javier R, Esther A. PEF as a green technology for extraction from thinned peach by-products. Innov Food Sci Emerg Technol. 2018;45:335-43.

[20] Suthira M, Praban R. Quantity of phenolic compounds and flavonoids. KKU Sci J. 2016;44:142-52.

[21] Tonutare T, Moor U, Szajdak L. Strawberry anthocyanins differentiation by pH differential spectroscopic method. Acta Sci Pol Hortorum Cultus. 2014;13:35-47.

[22] Kanchana S, Samaiphon P, Apinya A, Rapikorn C, Phonpat SA, Panadda C, Kulawadee P. Analysis of antioxidant substances in rice. PSRU J. Sci Technol. 2019;4:95-108.

[23] Rubashvill I, Tsitsagi M, Tsitsishvili V, Kordzakhia T, Ebralidze K, Buzariashvili M, Khachidze M. Sequential extraction and HPLC analysis of total anthocyanins of grape skin. The Chemist. 2019;91:33-41.

[24] Chittapun S, Jonjaroen V, Khumrangsee K, Charoenrat T. C-phycocyanin extraction from cyanobacteria by freeze-thaw and pulsed electric field. Algal Res. 2020;46:101789.

[25] Jansom C, Skulkhu E, Jansom V, Lerdvuthisopon N, Bhamarapravati K. Extraction of antioxidant compounds from black glutinous rice. Thammasat Med J. 2016;16(4):625-633.

[26] Raso J, Frey W, Ferrari G, Pataro G, Knorr D, Teissie J, Miklavčič D. Recommendations on PEF reporting. Innov Food Sci Emerg Technol. 2016;37:312–21.

[27] Mahnič-Kalamiza S, Vorobiev E, Miklavčič D. Electroporation in food processing. J. Membr Biol. 2014;247(12):1279-1304.

[28] Zhang ZH, Wang LH, Zeng XA, Han Z, Wang MS. Effect of PEFs on spinach pigments. Innov Food Sci Emerg Technol. 2017;43:26–34.

[29] Pataro G, Bobinaite R, Bobinas C, Satkauskas S, Raudoni R, Visockis M, Ferrari G, Viskelis P. Extraction of anthocyanins from blueberry. Food Bioprocess Technol. 2017;10(9):1595-1605.

[30] Delso C, Berzosa A, Sanz J, Alvarez I, Raso J. Response Surface Methodology for extraction conditions. Foods. 2022;11(4):621.

[31] Salee N, Chaiyana W, Yawootti A, Naruenartwongsakul S, Klangpetch W, Walter P, Utama-ang N. Optimization of PEF extraction of black rice. Sci Rep. 2022;12:6459.

Monitoring Water Turbidity in the Chiang Rai Reach of the Mekong River Using Sentinel-2 NDTI

Jurawan Nontapon[1], Phailin Kummuang[2], Neti Srihanu[2], Arun Kumar Bhomi[3], Rabi Shrestha[3], Rabina Poudyal[3], Umesh Bhurtyal[4], Pragya Pant[5] and Siwa Kaewplang[6*]
[1] Civil and Construction Management Engineering, Faculty of Science, Chandrakasem Rajabhat University, Bangkok, Thailand, 10900
[2] Faculty of Engineering, Northeastern University, Khon Kaen Province, Thailand, 40000
[3] Department of Geomatics Engineering, School of Engineering Kathmandu University, Dhulikhel, Kavre, Nepal, 6250
[4] Department of Geomatics Engineering, Pashchimanchal Campus, Tribhuvan University, Nepal, 33700
[5] Geography at the department of Geography, Minnesota State University, Mankato, MN, USA, 56001
[6*] Faculty of Engineering, Mahasarakham University, Kantharawichai District, Maha Sarakham, Thailand, 44150
[*]Corresponding Author: Siwa.kae@msu.ac.th Phone Number: +66-815475825
Received: 21 September 2025, Revised: 14 November 2025, Accepted: 26 November 2025

Abstract
The Mekong River plays a vital role in regional ecology, food security, and water governance, yet turbidity monitoring in its upper reaches remains limited. The Chiang Rai sector, located at the first upstream entry point of the Lower Mekong Basin, functions as a sediment and flow gateway to downstream countries; however, no systematic satellite-based turbidity assessment has previously been conducted for this area. This study addresses this gap by applying the Normalized Difference Turbidity Index (NDTI) derived from Sentinel-2 MSI imagery to investigate spatial and seasonal turbidity dynamics from 2019 to 2024. Multi-temporal satellite datasets were processed using Google Earth Engine and integrated with monthly rainfall (TerraClimate) and water surface area extracted using the Modified Normalized Difference Water Index (MNDWI). Results revealed a clear monsoonal pattern, with turbidity peaking between June and September and declining during the dry season (November-April). Regression analysis showed a moderate correlation between rainfall and turbidity ($R^2 = 0.37$), while a stronger association with water surface area ($R^2 = 0.514$) indicates the dominant influence of hydromorphological processes such as sediment resuspension and floodplain connectivity. Although the absence of field-based turbidity measurements represents a key limitation, the findings demonstrate the potential of Sentinel-2 -based NDTI as a cost-efficient monitoring tool in data-scarce transboundary basins. This study provides the first satellite-derived turbidity baseline for the northern Mekong and offers a practical framework to support basin-wide water-quality monitoring and policy decision-making under increasing hydropower regulation and climate variability.
Keywords: Mekong River, NDTI, MNDWI, Sentinel-2, TerraClimate

1. Introduction

The Mekong River is a major transboundary river system supporting regional ecosystems, agriculture, fisheries, navigation, and domestic water supply across six countries in Southeast Asia [1]. Beyond its socio-economic importance, the river functions as a dynamic sediment-water system in which turbidity plays a key role in controlling water quality, aquatic habitat conditions, and sediment transport processes [2]. The Chiang Rai reach in Northern Thailand represents the first upstream section of the Lower Mekong Basin and serves as the primary entry point where sediment loads, and hydrological conditions begin to propagate downstream into Laos, Cambodia, and Vietnam. Because of this upstream influence, changes in turbidity within this sector have basin-wide implications for river morphology, fisheries productivity, and transboundary water governance. Although previous studies have examined turbidity in various parts of the Lower Mekong Basin [3-5].

Most rely on sparse and spatially discontinuous in-situ measurements, which are insufficient for capturing rapid hydrological changes and seasonal sediment pulses [6]. Findings from other large Asian rivers (e.g., Ganges, Yangtze) confirm that turbidity and suspended sediment concentration (SSC) can vary sharply within a single monsoon cycle, highlighting the limitation of field-only datasets [4,7]. Despite this, no study has yet provided a satellite-based turbidity assessment for the Chiang Rai reach, leaving a critical upstream monitoring gap in the Mekong River system.

To address these monitoring gaps, numerous studies have confirmed that satellite remote sensing provides a reliable and efficient means of evaluating water turbidity across diverse hydrological settings, including large rivers [3,5], reservoirs and dams [4,8], lakes and coastal waters [7,9,10], and small inland water bodies [11]. High-resolution, frequently acquired satellite imagery enables consistent observation, making the Normalized Difference Turbidity Index (NDTI) an effective tool for monitoring turbidity in large, highly dynamic water bodies.

For example, at the Panchet Dam in India, turbidity rose sharply from 60 NTU to 700 NTU during the monsoon season. At its peak, highly turbid water covered more than 64 % of the reservoir, and the Landsat-8-derived NDTI showed a strong correlation with suspended sediment concentration (SSC) (R^2 = 0.90, RMSE = 13.59) [4]. Elhag et al. [8] used Sentinel-2 imagery to monitor water quality in the Wadi Baysh Dam (2017–2018). Field measurements showed strong correlations between satellite-derived indices and in-situ data chlorophyll a with MCI (R^2 = 0.96), nitrate with GNDVI (R^2 = 0.94), and turbidity with NDTI (R^2 = 0.94) demonstrating that Sentinel-2 provides an effective tool for assessing water quality in arid environments. Nontapon et al. [3] reported that Landsat-8 analysis of the Mekong River showed the NDSSI to be the most accurate index for estimating SSC (R^2 = 0.723, RMSE = 20.2 mg L^{-1}), whereas NDTI was less reliable (R^2 = 0.418, RMSE = 27.5 mg L^{-1}). Kolli & Chinnasamy [5] found that, in the highly dynamic Godavari River of India, Sentinel-2 imagery revealed that a red-edge single-band algorithm provided the most accurate turbidity estimates (R^2 = 0.91, RMSE = 0.003), outperforming NDTI (R^2 = 0.85, RMSE = 0.05). Li et al. [7] demonstrated the importance of long-term monitoring: a 30-year time series (1990-2020) of Landsat-5, Landsat-7, and Landsat-8 images for China's Chao Lake showed NDTI values increasing by more than 242 %, indicating intensified sedimentation and declining water quality. Dabire et al. [9] analyzed Sentinel-2 surface-reflectance data to compute NDTI and the Normalized Difference Chlorophyll Index (NDCI), reporting NDTI values from -0.045 to 0.0723 and NDCI values from -0.016 to 0.019, with the highest pollution detected along the shoreline. Ardyan [10] used Sentinel-2A imagery of Jakarta Bay, Indonesia, processed in Google Earth Engine, to calculate NDTI and Total Suspended Solids (TSS). Analysis of five observation points revealed clear spatial variation: Point 1 recorded the highest turbidity (NDTI = 0.21; TSS = 46.81 mg L^{-1}), Point 5 the lowest, and Point 3 the highest NDTI (0.23) but only 23.49 mg L^{-1} TSS, indicating finer suspended particles. Lacaux et al. [11] employed 10 m-resolution SPOT-5 imagery over the Ferlo region of Senegal, using the NDPI and NDTI indices to map small ponds. They found that ponds smaller than 0.5 ha accounted for 65–90 % of total pond area and that potential Rift Valley Fever mosquito habitat covered up to 25 % of the region during the rainy season. For Lake Nokoue in Benin.

These studies demonstrate that although the Normalized Difference Turbidity Index (NDTI) is highly useful for assessing water turbidity across a wide range of aquatic environments-including large rivers, reservoirs, lakes, and coastal waters-its performance is not uniformly consistent. Multiple factors, such as watershed characteristics, seasonal variations, upstream sediment loads, and human activities, can influence the accuracy of NDTI, leading to regional differences in assessment results. In many cases, long-term monitoring is essential to capture sedimentation trends and ongoing changes in water quality. Continuous observation over extended periods also helps identify seasonal or anthropogenic patterns of turbidity variation, such as those driven by dam construction, agricultural practices, or

urban expansion, providing critical information for water-resource management and sustainable environmental planning.

Research on the Chiang Rai reach of the Mekong River remains limited, despite its role as a critical upstream gateway of the Lower Mekong Basin where sediment transport and turbidity dynamics directly influence downstream water quality and regional food security. Applications of Sentinel-2–derived NDTI for this area are still scarce, and comprehensive evaluations integrating temporal and seasonal turbidity variations with spatial and seasonal heterogeneity have yet to be undertaken. Addressing these gaps is essential to advance understanding of spatio-temporal turbidity processes and to establish a cost-effective, satellite-based monitoring framework that complements conventional field observations. This study is based on the hypothesis that the NDTI from Sentinel-2 imagery can effectively reflect both the spatial and seasonal variability of water turbidity in the Mekong River within Chiang Rai Province. Higher turbidity is expected during the monsoon season due to increased sediment loads. The objectives of this research are: 1 to analyze the spatial distribution of turbidity using Sentinel-2 NDTI, and 2 to examine temporal and seasonal changes in turbidity patterns in the Mekong River within Chiang Rai Province.

2. Research Methodology

2.1 Study Area

The study was conducted in the Mekong River within Chiang Rai Province, northern Thailand. This section is a critical upstream reach of the Lower Mekong Basin, where hydrological flow and sediment transport strongly influence downstream water quality and aquatic ecosystems. Chiang Rai Province is located in a mountainous region, with elevations ranging from approximately 300 meters along the river plains to over 1,500 meters in the surrounding highlands. This topography contributes to rapid surface runoff and soil erosion, particularly during heavy rainfall, which increases sediment transport into the Mekong River.The climate of Chiang Rai is classified as tropical monsoon, consisting of three distinct seasons: a cool-dry season (November-February), a hot-dry season (March-May), and a rainy season (June-October). The average annual rainfall ranges between 1,200-1,600 mm, with the majority occurring during the monsoon period. Air temperatures generally range from 15-25 °C during the cool season to 25–35 °C in the hot season, with an annual mean temperature of about 24 °C. These climatic and topographic characteristics play a significant role in shaping the hydrological dynamics and turbidity variability of the Mekong River within Chiang Rai Province (see Figure 1).

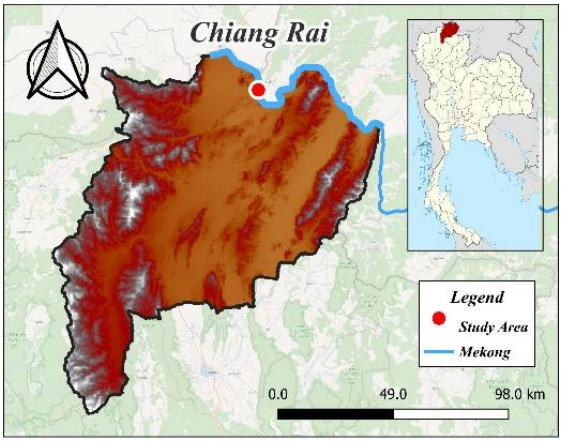

Figure 1 Location of the study area in the Mekong River at Chiang Rai Province, Northern Thailand.

2.2 Data Sources

This study employed multi-source datasets to monitor water turbidity in the Mekong River within Chiang Rai Province. Sentinel-2 MSI Level-2A surface reflectance imagery (COPERNICUS/S2_SR_HARMONIZED) from January 2019 to December 2024 was used, focusing on the Green (B3, 560 nm), Red (B4, 665 nm), and SWIR1 (B11, 1610 nm) spectral bands, with a spatial resolution of 10-20 m. and a revisit frequency of approximately five days. The data were processed and analyzed on the Google Earth Engine (GEE) platform [12] (accessed on August 25, 2025). From these data, the MNDWI was calculated to delineate water bodies, and the NDTI was applied as a proxy for turbidity. Monthly precipitation data were obtained from the TerraClimate dataset (*IDAHO_EPSCOR/TERRACLIMATE*) with 4.6 km resolution for the same period, providing climatic context [13].

Ancillary datasets included river boundary shapefiles for clipping and hydrological statistics from the Thai Meteorological Department and the Mekong River Commission for contextual interpretation. Cloud and shadow masking was performed using the Sentinel-2 Scene Classification Layer (SCL), with additional filtering based on the cloud probability layer (CLOUD_PROBABILITY < 20%). Preprocessing steps consisted of atmospheric correction (Level 2A), cloud and shadow removal, spatial clipping to the study area, and the generation of monthly median composites. A water mask with an MNDWI threshold greater than 0.1 was applied to ensure NDTI calculations were restricted to water pixels only.

2.3 Index Calculation

In this study, the NDTI was applied as the primary indicator of water turbidity [14]. The NDTI was calculated using the Red (B4) and Green (B3) bands of Sentinel-2 imagery according to the following Equation (1).

$$NDTI=\frac{Red-Green}{Red+Green} \quad (1)$$

Where Red is Band 4
Green is Band 3

This index was used as a turbidity proxy to detect suspended sediments and water quality changes, while monthly rainfall data (mm/month) from the TerraClimate dataset for the same period provided hydrological context for interpreting turbidity variability.

2.4 Monthly Aggregation and Statistical Analysis

For each month between January 2019 and December 2024, Sentinel-2 imagery was processed to generate monthly median composites, minimizing the effects of cloud contamination and temporal noise. The NDTI was calculated for each composite and masked using the MNDWI to ensure that turbidity measurements were restricted to water pixels only [15]. The MNDWI was computed from Sentinel-2 bands according to Equation (2).

$$mNDWI=\frac{Green-SWIR1}{Green+SWIR1} \quad (2)$$

Where Green is Band 3
SWIR1 is Band 11

Descriptive statistics including the mean, median, and standard deviation of NDTI were then computed within the study area to evaluate spatial and temporal variability in water turbidity. Water surface area was also estimated in both square meters and square kilometers using pixel area values where MNDWI exceeded 0.1. To provide hydrological context, monthly precipitation data from the TerraClimate dataset were averaged across the study area. Finally, all outputs-including NDTI statistics, water surface area, and rainfall data-were exported as Comma-Separated Values (CSV) files to support subsequent statistical and comparative analyses.

2.5 Visualization and Analysis

The visualization and analysis focused on examining the spatial and temporal variations of turbidity in the Mekong River throughout the study period. Time-series charts were generated to illustrate monthly changes in the NDTI, water surface area, and rainfall, which clearly highlighted seasonal differences between the monsoon and dry seasons. In addition, scatter plots were used to assess the relationships between rainfall and turbidity, as well as between water surface area and NDTI, reflecting the interactions between hydrological conditions and sediment transport processes. Linear regression trendlines were applied to the scatter plots to statistically evaluate both the strength and direction of these relationships. These visual and statistical analyses enabled the detection of distinct seasonal patterns, such as higher turbidity during the monsoon season and lower values during the dry season, providing essential insights for both scientific understanding and practical applications in water resource management.

3. Result

The results of this analysis, derived from Sentinel-2 MSI Level-2A surface reflectance data(COPERNICUS/S2_SR_HARMONIZED) covering the period from January 2019 to December 2024, are summarized in Table 1 and Figure 2. The NDTI was employed as a proxy for water turbidity, while the MNDWI was used to

delineate water bodies and restrict calculations to water pixels. To incorporate hydrological context, monthly rainfall data from the TerraClimate dataset (IDAHO_EPSCOR/TERRACLIMATE) were integrated into the analysis. All datasets were processed and analyzed using the Google Earth Engine (GEE) platform.

Table 1. Annual mean values and variability of NDTI, rainfall, and water surface area in the Mekong River (2019–2024).

Year	NDTI (Mean ± SD)	Rainfall (mm) (Mean ± SD)	Water Area (km^2) (Mean ±SD)
2019	0.013 ± 0.07	858 ± 94.7	34.45 ± 13.4
2020	−0.004 ± 0.10	1318 ± 130.7	34.68 ± 9.3
2021	0.025± 0.10	1340 ± 90.4	36.99 ± 6.7
2022	0.05 ± 0.09	1567 ± 117.7	38.50 ± 7.2
2023	0.016 ± 0.09	1321 ± 126.6	36.82 ± 6.2
2024	0.039 ± 0.12	1978 ± 210.9	34.90 ± 11.9

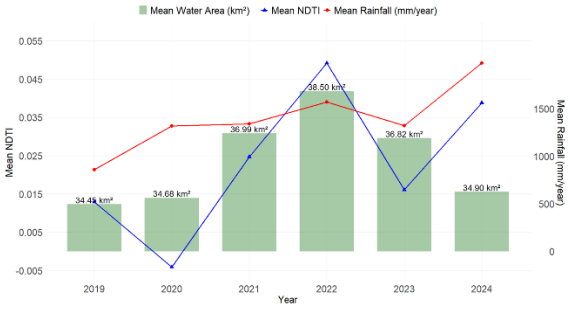

Figure 2 Annual Dynamics of Mean NDTI, Rainfall, and Surface Water Area in the Mekong River at Chiang Rai (2019–2024).

In addition, Figure 3 presents maps of the seasonal variation of turbidity (NDTI) in the Mekong River at Chiang Rai during 2024: (a) January-March, (b) April-June, (c) July-September, and (d) October-December.

3.1 Monthly NDTI Analysis

The analysis of the NDTI from January 2019 to December 2024 revealed distinct seasonal fluctuations in the Mekong River within Chiang Rai Province (Figure 4). NDTI values ranged from -0.18 to 0.20, reflecting increased turbidity during the monsoon season (June-September) and reduced turbidity during the dry season (November-April). The highest turbidity values were recorded in August 2020 and September 2024, when NDTI reached approximately 0.20, indicating elevated suspended sediment loads driven by rainfall and surface runoff. In contrast, the lowest values occurred in March-April 2020 and January-February 2024, with NDTI dropping below -0.15, signifying clearer water conditions during the dry season.

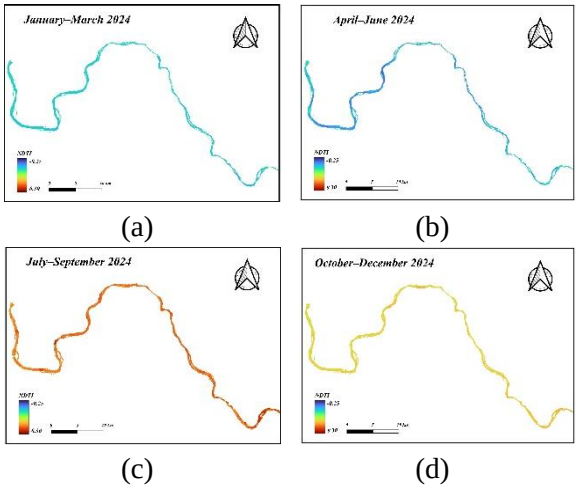

Figure 3 Seasonal variation of turbidity (NDTI) in the Mekong River at Chiang Rai during 2024: (a) January-March, (b) April-June, (c) July-September, and (d) October-December.

This recurring annual cycle highlights the direct relationship between rainfall and turbidity: heavy rainfall leads to increased runoff and higher suspended sediment concentrations, raising NDTI values, while reduced rainfall corresponds to clearer water and lower NDTI values. These findings underscore the continuity of hydrological processes and the critical role of seasonal dynamics in shaping turbidity patterns in the Mekong River at Chiang Rai, as illustrated in Figure 3.

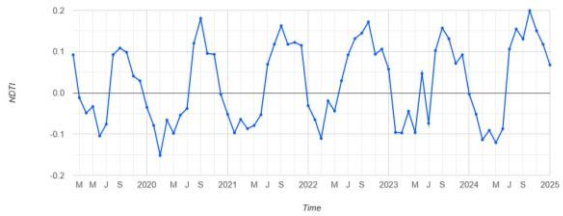

Figure 4 Monthly variation of the NDTI in the Mekong River at Chiang Rai (2019-2024).

3.2 Monthly Rainfall and NDTI Analysis

The time-series analysis of the NDTI and rainfall between January 2019 and December 2024 reveals a strong seasonal pattern in the Chiang Rai reach of the Mekong River (Figure 5). Peaks in rainfall

during the monsoon months (June-September) consistently coincide with elevated NDTI values (up to ~0.20), indicating higher turbidity driven by increased runoff and suspended sediment inflows. Conversely, during the dry season (November-April), rainfall drops to near zero and NDTI values decline below -0.15, reflecting clearer water conditions.

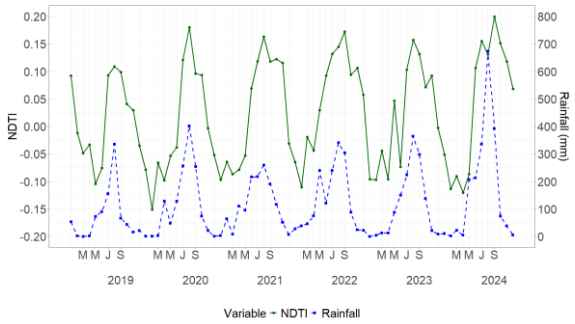

Figure 5 Monthly variation of rainfall and NDTI in the Mekong River at Chiang Rai (2019-2024).

3.3 Correlation Between Monthly Rainfall and NDTI

The relationship between monthly rainfall and turbidity, expressed by the NDTI, indicates a moderate positive correlation in the Chiang Rai reach of the Mekong River (Figure 6). The regression analysis yielded Equation (3).

$$NDTI=-0.0314+0.000412\times Rain \quad (3)$$

Where NDTI = Normalized Difference Turbidity Index, a proxy for water turbidity.

Rain(mm) = Monthly rainfall in millimeters.

With a coefficient of determination of $R^2=0.37$ ($p<0.05$) This suggests that approximately 37% of the variability in NDTI can be explained by monthly rainfall, as shown in Equation (3), This indicates a statistically significant but moderate linear relationship between precipitation and turbidity dynamics in the study area.

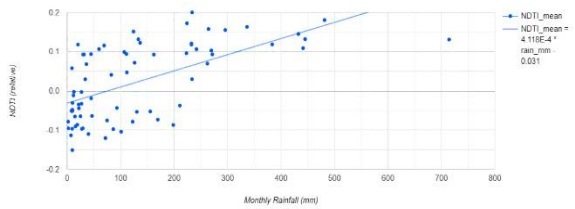

Figure 6 Scatter plot shows correlation between rainfall and NDTI in the Chiang Rai reach of the Mekong River.

3.4 Monthly Variability of NDTI and Water Area in the Mekong River

The analysis of monthly NDTI values and water surface area in the Chiang Rai reach of the Mekong River between 2019 and 2024 revealed clear seasonal dynamics (Figure 7). NDTI values tended to increase during the monsoon season (June-September), reflecting higher turbidity caused by increased sediment inflow, while lower values during the dry season (November-April) indicated clearer water conditions. In contrast, the water surface area remained relatively stable throughout most of the study period, showing only minor fluctuations.

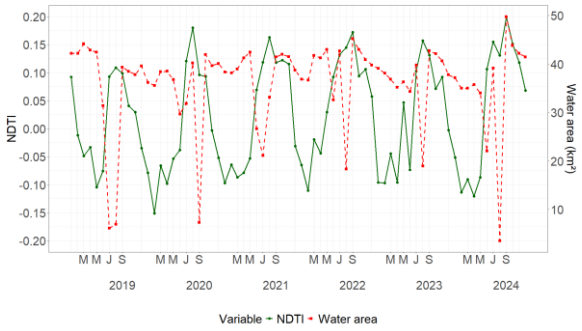

Figure 7 Monthly variation of NDTI and water surface area in the Chiang Rai reach of the Mekong River (2019-2024).

3.5 Correlation Between Water Area and NDTI

The relationship between water surface area and turbidity, expressed by the NDTI, shows a significant positive correlation in the Chiang Rai reach of the Mekong River (Figure 8). Linear regression analysis produced Equation (4), indicating that as the water surface area increases, the NDTI also tends to rise. This pattern reflects higher turbidity resulting from sediment resuspension and increased inflow during wetter hydrological conditions. The coefficient of determination ($R^2 = 0.514, p < 0.001$) suggests that approximately 51% of the variability in NDTI can be explained by changes in water surface area.

$$NDTI=-0.863+0.022\times Water\ Area \quad (4)$$

Where

NDTI = Normalized Difference Turbidity Index.

Water Area = Surface water area (km^2).

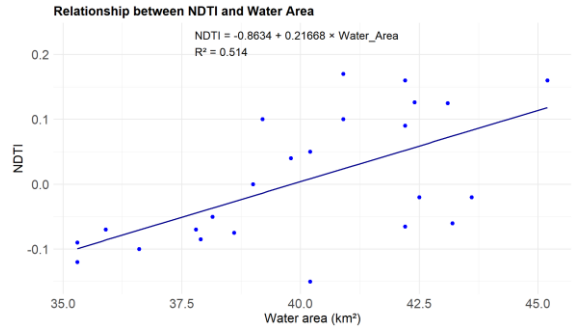

Figure 8 Scatter plot shows the relationship between water surface area and NDTI in the Chiang Rai reach of the Mekong River.

However, an important deviation from this trend occurs in September of every year, when the water surface area declines abruptly despite the river still being within the wet season. This anomaly is not attributable to reduced rainfall but instead reflects upstream hydropower flow regulation from dams in China and Laos, which typically begin storing water in preparation for the dry season. As a result, turbidity levels (NDTI) remain relatively high due to sediment mobilization from preceding monsoon flows, while the observable surface water area decreases sharply. This decoupling effect creates outlier behavior in the regression model and slightly reduces the overall coefficient of determination.

4. Discussion

The analysis of turbidity dynamics in the Mekong River at Chiang Rai provides valuable insights into the seasonal variability and hydrological drivers of water quality. Spatial and temporal analysis of the NDTI revealed a clear seasonal cycle, with elevated turbidity during the monsoon (June-September) and reduced turbidity in the dry season (November-April). Peak NDTI values (~0.20) in August 2020 and September 2024 coincided with heavy rainfall and surface runoff, while the lowest values (< -0.15) were recorded during dry months such as March-April 2020 and January-February 2024. These findings support the hypothesis that turbidity in the Chiang Rai reach is strongly influenced by seasonal precipitation regimes, consistent with studies in other dynamic river systems, such as the Godavari River [5] and the Panchet Dam [4], where turbidity patterns were closely linked to rainfall and seasonal hydrological conditions.

The spatio-temporal analysis of turbidity in the Chiang Rai reach revealed a clear monsoonal pattern, with elevated NDTI values during June-September and reduced turbidity in the dry season, reflecting strong seasonal hydrological control. However, the statistical analysis demonstrates that rainfall alone is not the dominant driver of turbidity dynamics. Although the rainfall-NDTI relationship was significant (R^2 = 0.37), the moderate strength of this correlation indicates that precipitation acts only as an indirect trigger of sediment processes. Similar decoupling between rainfall and turbidity has been observed in other large river basins, such as Chao Lake, China [7], where long-term increases in turbidity were driven more by sediment resuspension and land disturbance than by rainfall intensity.

In contrast, the stronger correlation between water surface area and turbidity (R^2 = 0.514) suggests that hydromorphological expansion of the river corridor is a more direct proxy for sediment mobilization. When the wetted width increases, flow energy and shear stress rise, enhancing bank erosion, sediment resuspension, and channel-bar scouring. This explains why turbidity can remain high even after rainfall decreases, and why floodplain connectivity plays a key role in sediment delivery. It also clarifies the "September anomaly," in which river width drops sharply while turbidity remains elevated-an indicator of upstream hydropower storage operations in China and Laos, which reduce surface extent but continue releasing sediment-rich flows. Similar regulation-driven decoupling has been documented in the Yangtze and Lancang-Mekong mainstream.

While NDTI proved effective for detecting seasonal turbidity patterns, several limitations must be acknowledged. First, NDTI is an optical proxy and does not directly measure suspended sediment concentration (SSC), meaning its spectral sensitivity may vary with sediment type, grain size, and water color. Second, the absence of field-measured turbidity or SSC data in this study prevents full quantitative validation of satellite retrievals. Third, the reported correlations fall

within a moderate range ($R^2 < 0.6$), indicating that predictive applications of NDTI alone may be inadequate without incorporating additional drivers such as discharge, dam-release data, and watershed land use.

Alternative spectral indices may offer improved performance. Previous work in the Mekong River indicated that the Normalized Difference Suspended Sediment Index (NDSSI) produced higher accuracy than NDTI for SSC estimation[3],while red-edge-based turbidity models using Sentinel-2 band 5 achieved superior performance in highly dynamic rivers such as the Godavari [4,5]. Future work should therefore compare NDTI with red-edge and SWIR-based algorithms or apply machine-learning regression using multi-band spectral inputs combined with hydrological variables.

Overall, this study provides the first satellite-based turbidity assessment for the Chiang Rai reach and demonstrates the practical value of integrating Sentinel-2 monitoring into basin-wide water-quality systems, particularly where in-situ networks are sparse. A combined satellite and field-based validation framework would enhance the capacity of the Mekong River Commission and national agencies to detect sediment anomalies, assess hydropower impacts, and strengthen early-warning and sediment-management strategies across the transboundary Mekong Basin.

5. Conclusion

This study applied the NDTI derived from Sentinel-2 MSI data to examine the spatial and seasonal dynamics of turbidity in the Mekong River at Chiang Rai, a critical upstream reach of the Lower Mekong Basin. The findings highlight several key insights.

First, consistent with the study hypothesis, turbidity exhibited a clear seasonal cycle, with elevated NDTI values during the monsoon season (June-September) and reduced values during the dry season (November-April). This pattern reflects the dominant role of rainfall-driven processes in controlling suspended sediment transport. Second, the analysis confirmed a moderate positive correlation between rainfall and NDTI ($R^2 = 0.37$), indicating that precipitation is an important, though not exclusive, driver of turbidity dynamics. Additional hydrological and geomorphological processes-such as sediment resuspension, bank erosion, and floodplain connectivity-also play a significant role in shaping turbidity levels. Third, the relationship between water surface area and turbidity showed a stronger positive correlation ($R^2 = 0.514$), underscoring that riverine hydro morphological factors exert a more direct influence on turbidity than rainfall alone.

Integrating these results, the study demonstrates the practical value of Sentine l-2 based NDTI as a cost-effective tool for monitoring turbidity in large, dynamic river systems. Compared with conventional field-based networks, which are often limited in coverage, unevenly distributed, and costly to maintain, satellite observations provide high-resolution, frequent, and spatially consistent data. The findings confirm that NDTI remains a reliable proxy for monitoring seasonal and hydrological turbidity dynamics, particularly in data-scarce regions such as Chiang Rai.

However, several limitations should be acknowledged. (1) NDTI is used as a single proxy index for turbidity and does not directly measure suspended sediment concentration (SSC), meaning its accuracy may vary with optical conditions, sediment characteristics, or concentration saturation. (2) The study lacks field-based turbidity or SSC validation data, which prevents full assessment of the absolute accuracy of satellite-derived values. (3) The statistical relationships observed ($R^2 = 0.37$ and 0.514) indicate moderate not strong correlation levels, suggesting that turbidity cannot be fully explained by rainfall or water area alone and may require additional hydrological inputs such as discharge or dam-release data.

In summary, this research advances current understanding by addressing the gap in turbidity monitoring for the Chiang Rai reach of the Mekong River, an upstream area of strategic importance to the Lower Mekong Basin that has not been systematically studied. The results reinforce the importance of integrating satellite-derived indices into basin-wide and transboundary water quality monitoring frameworks. Such

approaches can complement field observations, provide timely and spatially extensive information, and support sustainable water resource management in the Mekong region under the combined pressures of climate change and human activities.

Although this study has demonstrated the potential of using the NDTI derived from Sentinel -2 data for monitoring turbidity in the Mekong River at Chiang Rai, several avenues for future research remain. First, integrating data from higher-frequency satellite missions (e.g., Sentinel -1 SAR or Planet Scope imagery) could enhance the temporal resolution of turbidity monitoring, particularly during rapid hydrological events such as flash floods. Second, linking remote sensing data with hydrodynamic and sediment transport models would enable predictive assessments of turbidity under future climate change and land-use scenarios, thereby strengthening the capacity for proactive water resource management.

Third, future work should compare NDTI with alternative turbidity indices (e.g., NDSSI, red-edge indices) and incorporate field validation campaigns to improve reliability of satellite-based monitoring.

6. Acknowledgment

This research project was financially supported by Chandrakasem Rajabhat University.

7. References

[1] Mekong River Commission n.d. https://www.mrcmekong.org/ (accessed September 14, 2025).
[2] Douglas I. The Mekong river basin. Phys Geogr Southeast Asia Oxf Univ Press Oxf 2005:193–218.
[3] Nontapon J, Srihanu N, Auttarapong D, Hasita S, Ratanachotinun J, Bhurtyal UB, et al. Assessment of Suspended Sediment Concentration in the Mekong River Using Landsat-8 Data. Eng Access 2025;11:233-42.
[4] Bid S, Siddique G. Identification of seasonal variation of water turbidity using NDTI method in Panchet Hill Dam, India. Model Earth Syst Environ 2019;5:1179-200.
[5] Kolli MK, Chinnasamy P. Estimating turbidity concentrations in highly dynamic rivers using Sentinel-2 imagery in Google Earth Engine: Case study of the Godavari River, India. Environ Sci Pollut Res 2024;31:33837-47.
[6] Ogilvie A, Belaud G, Massuel S, Mulligan M, Le Goulven P, Calvez R. Surface water monitoring in small water bodies: potential and limits of multi-sensor Landsat time series. Hydrol Earth Syst Sci 2018;22:4349 -80.
[7] Li C, Rousta I, Olafsson H, Zhang H. Lake water quality and dynamics assessment during 1990-2020 (A case study: Chao Lake, China). Atmosphere 2023;14:382.
[8] Elhag M, Gitas I, Othman A, Bahrawi J, Gikas P. Assessment of water quality parameters using temporal remote sensing spectral reflectance in arid environments, Saudi Arabia. Water 2019;11:556.
[9] Dabire N, Ezin EC, Firmin AM. Water Quality Assessment Using Normalized Difference Index by Applying Remote Sensing Techniques: Case of Lake Nokoue. 2024 IEEE 15th Control Syst. Grad. Res. Colloq. ICSGRC, IEEE; 2024, p. 1-6.
[10] Ardyan PAN. Water Quality Analysis Using NDTI and TSS Parameters Based on Sentinel Image Data in Jakarta Bay Waters. Marit Park J Marit Technol Soc 2025:103-9.
[11] Lacaux JP, Tourre YM, Vignolles C, Ndione JA, Lafaye M. Classification of ponds from high-spatial resolution remote sensing: Application to Rift Valley Fever epidemics in Senegal. Remote Sens Environ 2007;106:66-74.
[12] Gorelick N, Hancher M, Dixon M, Ilyushchenko S, Thau D, Moore R. Google Earth Engine: Planetary-scale geospatial analysis for everyone. Remote Sens Environ 2017;202:18–27.
[13] Abatzoglou JT, Dobrowski SZ, Parks SA, Hegewisch KC. TerraClimate, a high-resolution global dataset of monthly climate and climatic water balance from 1958-2015. Sci Data 2018;5:1-12.
[14] Thoma DP. Management impacts and remote sensing applications for water quality assessment. University of Minnesota; 2003.
[15] Xu H. Modification of normalised difference water index (NDWI) to enhance open water features in remotely sensed imagery. Int J. Remote Sens 2006;27:3025-33. https://doi.org/10.1080/01431160600589179.

RMUTL Engineering Journal
Faculty of Engineering
Rajamangala University of technology Lanna

Journal of Engineering

Rajamangala University of technology Lanna